WWW.IJME.US
Print ISSN: 2157-8052
Online ISSN: 1930-6628

INTERNATIONAL JOURNAL OF MODERN ENGINEERING

Fall/Winter 2014
Volume 15, No. 1

The Leading Journal of Engineering, Applied Science and Technology

THE LEADING JOURNAL OF ENGINEERING, APPLIED SCIENCE, AND TECHNOLOGY

International Journal of Modern Engineering

www.ijme.us

Print ISSN: 2157-8052
Online ISSN: 1930-6628

International Association of Journals and Conferences

www.iajc.org

INTERNATIONAL JOURNAL OF MODERN ENGINEERING

ABOUT IJME:

- IJME was established in 2000 and is the first and official flagship journal of the International Association of Journal and Conferences (IAJC).
- IJME is a high-quality, independent journal steered by a distinguished board of directors and supported by an international review board representing many well-known universities, colleges and corporations in the U.S. and abroad.
- IJME has an impact factor of **3.00**, placing it among the top 100 engineering journals worldwide, and is the #1 visited engineering journal website (according to the National Science Digital Library).

OTHER IAJC JOURNALS:

- The International Journal of Engineering Research and Innovation (IJERI)
  For more information visit www.ijeri.org
- The Technology Interface International Journal (TIIJ).
  For more information visit www.tiij.org

IJME SUBMISSIONS:

- Manuscripts should be sent electronically to the manuscript editor, Dr. Philip Weinsier, at philipw@bgsu.edu.

  For submission guidelines visit
  www.ijme.us/submissions

TO JOIN THE REVIEW BOARD:

- Contact the chair of the International Review Board, Dr. Philip Weinsier, at philipw@bgsu.edu.

  For more information visit
  www.ijme.us/ijme_editorial.htm

INDEXING ORGANIZATIONS:

- IJME is currently indexed by 22 agencies. For a complete listing, please visit us at www.ijme.us.

Contact us:

Mark Rajai, Ph.D.

Editor-in-Chief
California State University-Northridge
College of Engineering and Computer Science
Room: JD 4510
Northridge, CA 91330
Office: (818) 677-5003
Email: mrajai@csun.edu

TIIJ International

www.tiij.org

International Journal of Engineering Research & Innovation IJERI

www.ijeri.org

INTERNATIONAL JOURNAL OF MODERN ENGINEERING

The INTERNATIONAL JOURNAL OF MODERN ENGINEERING (IJME) is an independent, not-for-profit publication, which aims to provide the engineering community with a resource and forum for scholarly expression and reflection.

IJME is published twice annually (Fall and Spring issues) and includes peer-reviewed articles, book and software reviews, editorials, and commentary that contribute to our understanding of the issues, problems, and research associated with engineering and related fields. The journal encourages the submission of manuscripts from private, public, and academic sectors. The views expressed are those of the authors and do not necessarily reflect the opinions of IJME or its editors.

EDITORIAL OFFICE:

Mark Rajai, Ph.D.
Editor-in-Chief
Office: (818) 677-2167
Email: ijmeeditor@iajc.org
Dept. of Manufacturing Systems
Engineering & Management
California State University-
Northridge
18111Nordhoff Street
Northridge, CA 91330-8332

THE INTERNATIONAL JOURNAL OF MODERN ENGINEERING EDITORS

TABLE OF CONTENTS

IN THIS ISSUE (P.5)

A DOOR MOTION ENERGY HARVESTING SYSTEM FOR POWERING AN ELECTRONIC DOOR LOCK

Philip Weinsier, IJME Manuscript Editor

You likely already know something about energy harvesting—or scavenging, as some choose to call it—or at least have heard about it. But in the not-too-distant future, most of us will find ourselves using the technology either actively by consciously manipulating a device, or passively by wearing clothing that collects untapped energy from our bodies to be used elsewhere or simply stored for future use.

The most obvious beneficiaries of energy-harvesting activities are laptops and mobile phones. Why obvious? Well consider that these now-ubiquitous devices were designed to be used on-the-go and run on batteries. Their batteries, though, have to be charged; thus, the devices themselves end up being tethered to umbilical power cords for extended periods of time. Fast-forward just a bit and you'll be charging your device(s) as you walk, dance, or eat breakfast. Energy can be scavenged from our bodies through even the slightest of movements, or the interaction of our bodies with our clothes. There's a dance club in the Netherlands that has a floor that is compressed by the dancers (less than a half inch) that generates up to 20 watts; not much in the scheme of things, though efficiency can only increase in the years to come. Researchers at a university in British Columbia are developing a generator affixed to a standard knee brace that could translate one minute of walking time into 30 minutes of cell-phone usage. Researchers at the Georgia Institute of Technology are working on clothing to collect our smallest movements that could also power a cell phone.

Though we can't (yet) charge our electric vehicles by doing a few pushups, we can already find applications for the technology in the consumer industry, healthcare, the auto industry, and the military. Estimates put annual sales around $5 billion—almost 20% of which is spent on wearable technology—with numbers of devices approaching one trillion, many of which are no larger than a pinhead. "Dumb" sensors simply gather information (data) and pass it on to a processor for analysis. Smart sensors are able to evaluate the incoming data, analyze it, perform calculations on it, and deliver outputs based on decisions made by the sensors.

In addition to smart clothing—that can measure your physical exertion, your heart rate, the number of calories burned, or even your quality of sleep and the air you breathe—smart sensors are already finding plenty of work: a thermostat adjustable via a mobile app; a door that can communicate its status (open/closed) to you; an app that will let you search for open parking spaces within the city or on your university campus; monitor (prevent) prescription drug and alcohol abuse; smart watches and glasses; heads-up displays; continuous glucose monitors; drug delivery; hand-worn terminals; augmented reality headsets; etc. You're probably already wondering if there's a sensor that could be used in an application that just came to mind!

Energy harvesting is unquestionably a great concept—as are the myriad applications—but where does this "extra" energy come from? And, if we physically are the source of the energy, are we being unduly taxed by having our energy stolen such that we tire so quickly as to reduce our ability to function normally throughout the day? In some early studies, subjects were asked to wear 80-pound packs; lugging that around all day would certainly intrude upon your normal routine. Besides yourself, though, other sources of energy could be thermal (furnaces, heaters, friction), light (solar, photo sensors/diodes), wind (or water such as ocean currents), mechanical (vibration, mechanical stress/strain), electromagnetic (inductors, coils, transformers); and chemical/biological sources. Stealing minute amounts of energy from any given source is one thing, but storing or processing it for use by some device is quite another. One common device to convert different forms of energy into electricity is a piezoelectric element. But let's not forget that all of the electronic elements used for capturing, storing, and managing our power also require power of their own. Thus, we would need to capture yet more energy to be able to power these systems.

In this current study, the authors developed an energy-harvesting system that could use the motion of a door to operate a card-swipe electronic door lock. By using a small electromechanical generator connected to the door that would convert the rotational motion of the door into electrical energy, they were able to harvest more energy than was required by the lock to perform the unlock procedure. The system was also invisible, or self-sustaining, and not a burden on the user or the system from which the energy was taken.

Editorial Review Board Members

Mohammed Abdallah	State University of New York (NY)
Nasser Alaraje	Michigan Tech (MI)
Aly Mousaad Aly	Louisiana State University (LA)
Jahangir Ansari	Virginia State University (VA)
Kevin Berisso	Ohio University (OH)
Salah Badjou	Wentworth Institute of Technology (MA)
Pankaj Bhambri	Guru Nanak Dev Engineering (INDIA)
Water Buchanan	Texas A&M University (TX)
Jessica Buck Murphy	Jackson State University (MS)
John Burningham	Clayton State University (GA)
Shaobiao Cai	Penn State University (PA)
Vigyan Chandra	Eastern Kentucky University (KY)
Isaac Chang	Cal Poly State University SLO (CA)
Bin Chen	Purdue University Calumet (IN)
Wei-Yin Chen	University of Mississippi (MS)
Hans Chapman	Morehead State University (KY)
Rigoberto Chinchilla	Eastern Illinois University (IL)
Phil Cochrane	Indiana State University (IN)
Michael Coffman	Southern Illinois University-Carbondale (IL)
Emily Crawford	Southern Wesleyen University (SC)
Brad Deken	Southeast Missouri State University (MO)
Z.T. Deng	Alabama A&M University (AL)
Sagar Deshpande	Ferris State University (MI)
David Domermuth	Appalachian State University (NC)
Ryan Dupont	Utah State University (UT)
Marilyn Dyrud	Oregon Institute of Technology (OR)
Mehran Elahi	Elizabeth City State University (NC)
Ahmed Elsawy	Tennessee Technological University (TN)
Rasoul Esfahani	DeVry University (OH)
Dominick Fazarro	Sam Houston State University (TX)
Rod Flanigan	University of Nebraska-Kearney (NE)
Ignatius Fomunung	University of Tennessee Chattanooga (TN)
Ahmed Gawad	Zagazig University EGYPT)
Daba Gedafa	University of North Dakota (ND)
Ralph Gibbs	Eastern Kentucky University (KY)
Mohsen Hamidi	Utah Valley University (UT)
Mamoon Hammad	Abu Dhabi University (UAE)
Youcef Himri	Safety Engineer in Sonelgaz (ALGERIA)
Xiaobing Hou	Central Connecticut State University (CT)
Shelton Houston	University of Louisiana Lafayette (LA)
Barry Hoy	St. Leo University (VA)
Ying Huang	North Dakota State University (ND)
Charles Hunt	Norfolk State University (VA)
Dave Hunter	Western Illinois University (IL)
Christian Hyeng	North Carolina A&T University (NC)
Pete Hylton	Indiana University Purdue (IN)
Ghassan Ibrahim	Bloomsburg University (PA)
John Irwin	Michigan Tech (MI)
Sudershan Jetley	Bowling Green State University (OH)
Rex Kanu	Ball State University (IN)
Reza Karim	North Dakota State University (ND)
Tolga Kaya	Central Michigan University (MI)
Satish Ketkar	Wayne State University (MI)
Manish Kewalramani	Abu Dhabi University (UAE)
Tae-Hoon Kim	Purdue University Calumet (IN)
Doug Koch	Southeast Missouri State University (MO)
Sally Krijestorac	Daytona State College (FL)
Ognjen Kuljaca	Brodarski Institute (CROATIA)
Chakresh Kumar	Uttar Pradesh Tech University (INDIA)
Zaki Kuruppalil	Ohio University (OH)
Edward Land	Johns Hopkins Medical Institute
Ronald Land	Penn State University (PA)
Jane LeClair	Excelsior College (NY)
Shiyoung Lee	Penn State University Berks (PA)
Soo-Yen Lee	Central Michigan University (MI)
Chao Li	Florida A&M University (FL)
Jimmy Linn	Eastern Carolina University (NC)
Dale Litwhiler	Penn State University (PA)
Guoxiang Liu	University of North Dakota (ND)
Louis Liu	University of New Orleans (LA)
Mani Manivannan	ARUP Corporation
G.H. Massiha	University of Louisiana (LA)
Thomas McDonald	University of Southern Indiana (IN)
David Melton	Eastern Illinois University (IL)
Shokoufeh Mirzaei	Cal State Poly Pomona (CA)
Bashir Morshed	University of Memphis (TN)
Sam Mryyan	Excelsior College (NY)
Wilson Naik	University of Hyderabad (INDIA)
Arun Nambiar	California State University Fresno (CA)
Ramesh Narang	Indiana University-Purdue University (IN)
Anand Nayyar	Institute Management and Tech (INDIA)
Stephanie Nelson	Cal State LA (CA)
Hamed Niroumand	Universiti Teknologi (MALAYSIA)
Aurenice Oliveira	Michigan Tech (MI)
Troy Ollison	University of Central Missouri (MO)
Reynaldo Pablo	Indiana University-Purdue University (IN)
Basile Panoutsopoulos	Community College of Rhode Island (RI)
Shahera Patel	Sardar Patel University (INDIA)
Jose Pena	Purdue University Calumet (IN)
Karl Perusich	Purdue University (IN)
Thongchai Phairoh	Virginia State University (VA)
Huyu Qu	Honeywell Corporation
John Rajadas	Arizona State University (AZ)
Desire Rasolomampionona	Warsaw University of Tech (POLAND)
Mulchand Rathod	Wayne State University (MI)
Mohammad Razani	New York City College of Tech (NY)
Sangram Redkar	Arizona State University-Poly (AZ)
Michael Reynolds	University of Arkansas Fort Smith (AR)
Marla Rogers	Wireless Systems Engineer
Dale Rowe	Brigham Young University (UT)
Anca Sala	Baker College (MI)
Mehdi Shabaninejad	Zagros Oil & Gas Company (IRAN)
Ehsan Sheybani	Virginia State University (VA)
Musibau Shofoluwe	North Carolina State University (NC)
Siles Singh	St. Joseph University Tanzania (AFRICA)
Ahmad Sleiti	University of North Carolina Charlotte (NC)
Jiahui Song	Wentworth Institute of Technology (MA)
Yuyang Song	Toyota Corporation
Carl Spezia	Southern Illinois University (IL)
Michelle Surerus	Ohio University (OH)
Vassilios Tzouanas	University of Houston Downtown (TX)
Jeff Ulmer	University of Central Missouri (MO)
Mihaela Vorvoreanu	Purdue University (IN)
Phillip Waldrop	Georgia Southern University (GA)
Abraham Walton	Purdue University (IN)
Liangmo Wang	Nanjing University of Science/Tech (CHINA)
Jonathan Williams	Lake Erie College (OH)
Boonsap Witchayangkoon	Thammasat University (THAILAND)
Alex Wong	Digilent Inc.
Shuju Wu	Central Connecticut State University (CT)
Baijian Yang	Ball State University (IN)
Mijia Yang	North Dakota State University (ND)
Faruk Yildiz	Sam Houston State University (TX)
Yuqiu You	Morehead State University (KY)
Jinwen Zhu	Missouri Western State University (MO)

A DOOR MOTION ENERGY HARVESTING SYSTEM FOR POWERING AN ELECTRONIC DOOR LOCK

Dale H. Litwhiler, Penn State Berks; Thomas H. Gavigan, Penn State Berks

Abstract

The harvesting of energy from small, unconventional sources is becoming more practical as higher density energy storage media emerge and ultra-low-power smart electronics are being integrated into a given system. The act of a human being opening a door can be employed as a means of generating electricity that can be captured and stored for use by electronic devices.

In the application presented here, the energy required to operate a card-swipe electronic door lock was obtained from the motion of the door itself. A small, hinge-mounted electromechanical generator was used to convert the rotational motion of the door into electrical energy. The output voltage of the generator was increased to that required by the door lock system with a custom DC-DC converter. The electrical output energy of the DC-DC converter was stored in a supercapacitor for use by the lock. The net energy harvested was greater than that required by the lock to perform the unlock procedure; thus, the system was sustainable. In this paper, the authors present the test setup and data obtained from various door-opening scenarios. The electrical and mechanical design of the energy harvesting system is also presented and discussed.

Motivation

All classroom and office doors in the new engineering building on the authors' campus are equipped with electronic card access locks. Each lock is powered by six AA primary non-rechargeable, alkaline cell batteries. During the first few months of building occupancy, many of the lock batteries became exhausted. Access to these rooms was delayed until maintenance could manually unlock the doors and install fresh batteries. With primary batteries alone, this scenario was inevitable.

The challenge was to design a lock power system that could scavenge the energy required to power the electronic lock from sources local to the door. The obvious source of energy was the motion of the door. If sufficient energy from one open and close sequence of the door could be captured, the energy required by the lock itself could be replaced such that the system was sustainable with little or no energy taken from the battery.

Introduction

Harvesting the energy from human sources has been widely presented and discussed in recent literature [1], [2], in particular, the energy generated by human use of doors [3-6]. The main goal in most energy harvesting applications is to capture waste energy that would otherwise be lost or ignored. When capturing human energy, the goal is often to make the process invisible and not unusually burden the user. In the situation from this current study, the door user was not to experience any unusual operation of the door as a result of the energy harvesting apparatus. The types of doors investigated in this study were common swing doors with no closing mechanism of any kind. The user had to physically push the door open and shut. Each door was equipped with a card-swipe electronic entry system, as shown in Figure 1.

Figure 1. Photos of Electronic Lock Assembly: Inside and Outside Views

The typical entry sequence involved swiping a badge through the card reader on the outside of the door, turning the handle, pushing the door open, and then pushing it closed from the other side. In the office scenario, the door was often left open until the user left the room, rather than closing it immediately after entering the room. Thus, there might be only one opening and closing of the door between subsequent unlock operations. A simple, hinge-mounted rotary motor functioning as a generator was conceived as the energy harvesting device. If the motor shaft could be made coaxial with the door hinge axis, a simple mounting arrangement could be implemented. The motor shaft could be fixed to the stationary side of the hinge, while the motor housing could then be mounted to the door in order to provide the required relative motion between the shaft and housing. The wiring from the generator to the lock assembly would then be all contained on the door itself. Figure 2 shows a photograph of the generator mounted to the door.

Figure 2. Photograph of Energy Harvesting Unit Mounted to the Door

Due to the relatively slow door rotation speed, a gear motor was required to provide sufficient motor speed to produce useful output voltage levels. Gear motors typically have the final output shaft offset toward the edge of the housing, which also helped to facilitate aligning the shaft with the hinge axis.

Energy Considerations

The energy required by one unlock sequence was measured in order to determine the system design minimum. The lock unit's battery output current was recorded during a card swipe unlock sequence. Figure 3 shows the recorded current waveform. As shown in Figure 3, the unlock sequence consisted of three pulses of current required by the lock mechanism. The initial pulse was the actual unlock pulse, while the following two pulses were involved with resetting the lock mechanism. Closer analysis of this current waveform showed that roughly 0.09 C of charge was required for the entire unlock sequence. Thus, for a battery voltage of 9 V, the required lock energy was about 0.8 J. Therefore, the energy harvester had to capture about this much energy during one door open and close sequence in order to be viable.

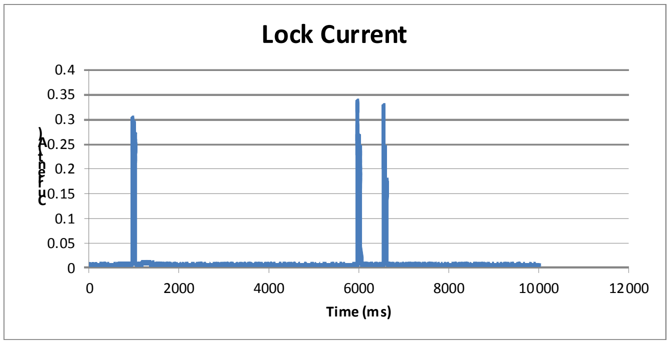

Figure 3. Battery Output Current Waveform During Unlock Sequence

Door Energy

Measurements of door parameters were made to determine approximate energy levels typically found in human-powered door motion. Door opening and closing speeds were recorded for several users. A typical office door was weighed and measured such that its moment of inertia could be calculated. Angular reference marks were placed on the floor beneath a typical office swing door at 15° intervals. A video was made while several volunteers opened and closed the door. The video data were reviewed frame-by-frame to extract the average time of motion for each user. The average time to open the door from fully closed to the 60° position was about 1.25 s, for an average speed of about 7.5 rpm. Figure 4 shows a still-frame of the video for one user opening the door.

Figure 4. Still Frame of Door-opening Video Trial

A human being pushing on a door increases the rotational kinetic energy of the door. This energy is a result of the inertia of the door and its angular velocity. A typical office door is shown in the photograph displayed in Figure 5. The kinetic energy of the rotating door can be calculated from Equation (1):

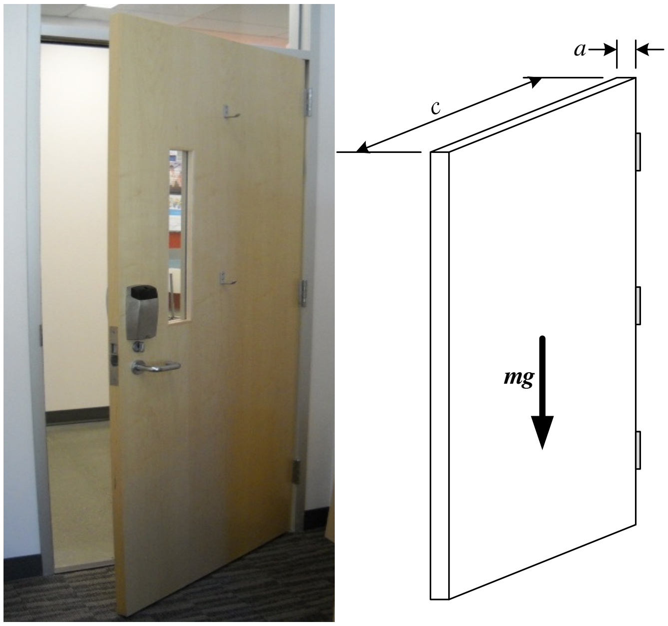

Figure 5. Photograph and Diagram of Typical Office Swing Door

$$KE = \frac{1}{2} I \omega^2 \tag{1}$$

where, I is the mass moment of inertia of the door with respect to its axis of rotation (axis of the door hinge) and ω is the angular velocity of the door in rad/s. The door is treated as a rectangular prism whose mass moment of inertia is given by Equation (2):

$$\mathrm{I} = \frac{1}{3} m(a^2 + c^2) \tag{2}$$

where, m is the mass of the door and a and c are its lateral dimensions, as shown in Figure 5. The mass of the door used in this test was approximately 45 kg, and the lateral dimensions a and c were 44 mm and 914 mm respectively. During the door opening testing, the average door speed of 7.5 rpm resulted in the door's kinetic energy being equal to approximately 3.9 J.

Laboratory testing of the generator showed that about 1 ft·lb of torque was required to turn the generator shaft at 7.5 rpm, with the nominal electrical load connected. The torque required to accelerate the door from a standstill to 7.5 rpm in 1 s was about 7.27 ft·lb. The resulting additional force required to open the door measured at the door handle position was about 0.4 lb. The user would experience only about a 13% increase in effort required to open the door.

Generator Selection

Several small gear motors were investigated as candidates for the door energy harvesting generator unit. Catalog data for each motor was extracted and used for comparison. A simple DC motor model, as shown in Figure 6, provided the necessary parameters needed for the comparison [7]. Parameters typically available from catalog data include terminal voltage, V_t, no-load current, I_{NL}, no-load speed (in rpm), n_{NL}, stall current, I_{stall}, and/or armature resistance, R_a. These parameters can be combined in order to determine the motor constant, k, which provides the open-circuit output voltage as a function of shaft speed. The maximum output power for each motor could also be found from the maximum power transfer equation, as shown in Equation (3):

$$R_a = \frac{V_t}{I_{stall}} \quad E_{a_{NL}} = V_t - I_{NL} R_a \quad k = \frac{E_{a_{NL}}}{n_{NL}} \quad P_{out_{max}} = \frac{E_a^2}{4R_a} \tag{3}$$

Using these parameters together with a typical door opening speed of 7.5 rpm, the motors could be compared, as shown in Table 1. From the comparison data for the available gear motors, the unit manufactured by Source Engineering was chosen for this application [8].

Table 1. Gear Motor Parameter Comparison

Motor Manufacturer	V_t	I_{NL}	n_{NL}	I_{Stall}	R_a	k (V/rpm)	$P_{out\text{-}Max}$
Pittman	19.1V	0.08A	82 rpm	1.5A	12.7Ω	0.22	0.054W
Maxon	36V	6mA	116 rpm	0.6A	60Ω	0.31	0.022W
Buhler	24V	0.035A	135 rpm	0.42A	57Ω	0.16	6.5mW
Sayama	12V	0.02A	62 rpm	0.41A	29Ω	0.18	13mW
Source Engineering	24V	0.06A	25 rpm	1.1A	22Ω	0.91	0.53W

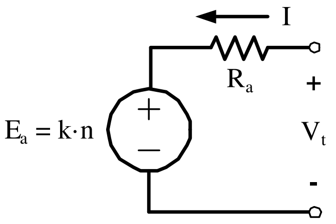

Figure 6. Simple DC Motor Model

Mechanical Design

The kinetic energy of the rotating door was transferred to a gear motor used as a generator mounted to the door at the point of the hinge. A photograph of the assembly is shown in Figure 2, and a CAD drawing of the motor with the motor shaft extending from it is shown in Figure 7. The motor housing firmly attached to the moving door rotates relative to its stationary shaft, which is attached to the door hinge with a set screw, as shown in Figure 2.

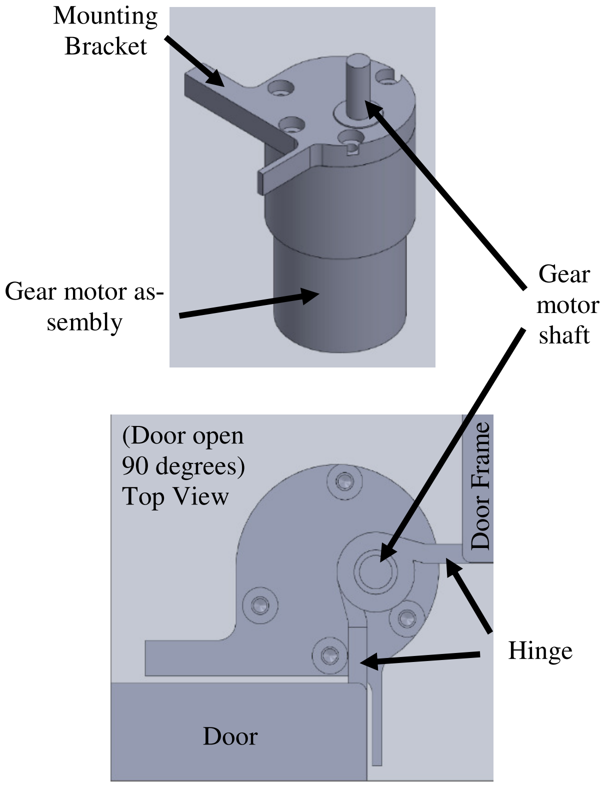

Figure 7. CAD Drawings of Generator Mounting Assembly

The unique design of the plate connecting the gear motor housing to the door provided a firm connection between them. In addition, it was unnecessary to drill holes into the door, thereby avoiding damage to the door. Doors that swing in the opposite direction to that shown here can be accommodated by mounting the generator to the top of the hinge. As a result, it would provide a more universal mounting configuration. The mounting bracket was fabricated on a CNC machine using low-carbon 1018 cold-rolled steel in order to provide the necessary strength, while keeping the thinnest possible profile. The bracket was secured to the generator using standard tapped mounting holes on the motor housing. The design provided a snug fit against the door's inner surface and edge to capture door motion in both directions and convey that relative motion to the generator.

Electrical Design

The output voltage polarity of brush-type DC motors changes with the direction of rotation. Therefore, in order to capture energy in both directions of door motion, the output of the generator had to be full-wave rectified. Schottky rectifiers were used to create the bridge circuit to minimize voltage drop. The generator output circuit is shown in Figure 8.

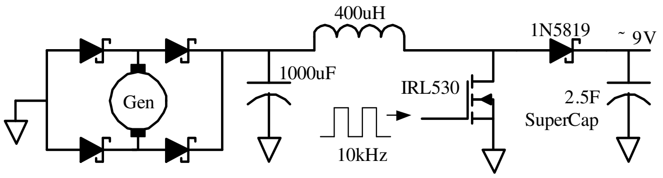

Figure 8. Generator Output Rectifier and Boost Converter Schematic

As shown in Table 1, the motor constant for the chosen gear motor was 0.91 V/rpm. At a typical rotational speed of 7.5 rpm, an open-circuit voltage of about 6.8 V would be produced. The maximum power transfer would, therefore, occur when the generator output terminals were loaded to produce a voltage of about 3.4 V. A boost converter would be required to produce a voltage near the 9 V required by the lock unit. A simple fixed-frequency, fixed-duty ratio boost converter was repurposed from another energy harvesting project. Figure 8 shows a schematic of the boost converter circuit. The MOSFET gate drive signal was obtained from a function generator for the experimental phase of the project. For the prototype, a fixed frequency of 10 kHz was used. The duty ratio was adjusted in order to obtain maximum energy transfer for typical door opening speeds. Due to the dynamic nature of the voltage source, a fixed-duty ratio boost converter provided a solution that was a compromise but not the true optimum performance.

Because of the short duration of the generator output pulse during door opening and closing operations, the energy could not efficiently be captured by an electrochemical process. Therefore, high capacity capacitors (referred to as super capacitors or ultra-capacitors) were investigated as a means of storing the pulsed energy [9] .Based on the available supercapacitor capacitance, voltage rating values and an acceptable voltage sag during the lock current pulses, a bank of four 10 F supercapacitors configured in series was chosen [10]. The total energy storage capacitance was 2.5 F. Each supercapacitor was rated at 2.7 V. A passive balancing resistance of 1 MΩ was placed in parallel with each supercapacitor to help maintain voltage sharing, while minimizing leakage current.

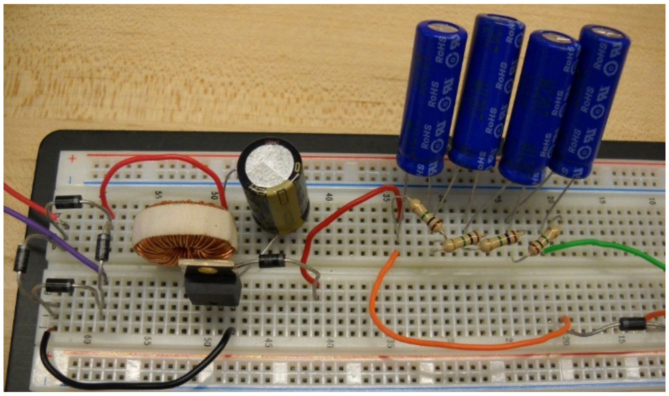

Figure 9. Photograph of Rectifier Bridge, Boost Converter, and Supercapacitor Bank Breadboard Circuit

Test Data

The battery pack of the lock was removed and replaced with the 2.5 F supercapacitor bank that had been pre-charged to 9.0 V with an external power supply. An unlock sequence was initiated by a card swipe, while the capacitor bank voltage was measured with a 5½ digit DMM. The capacitor bank voltage was observed to decrease by about 35 mV, as a result of the unlock operation. This voltage sag was consistent with an average current draw of about 16 mA for the duration of the unlock sequence time of about 5.5 seconds. The energy harvesting generator was mounted to a door, as shown previously in Figure 2. The open-circuit output voltage of the generator, after rectification, was recorded during several trials of opening and closing the door. Figure 10 shows the typical open-circuit voltage waveform. The waveform roughly approximated a half sine wave with a peak of about 10 V and a duration of about 2 seconds.

The generator/rectifier circuit was then connected to the input of the boost converter. The output of the boost converter was connected to the supercapacitor bank that was pre-charged to 9.0 V with an external power supply. Many door opening and closing trials were conducted for various values of boost converter duty cycle. The change in the supercapacitor bank voltage was measured for each trial. A duty ratio of 35% was found to produce the maximum change in capacitor bank voltage of about 50 mV for one complete open and close cycle of the door.

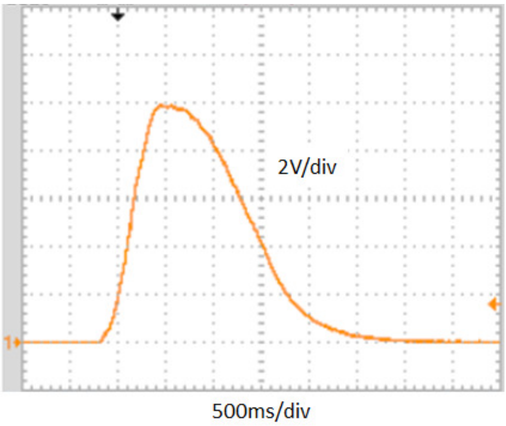

Figure 10. Open-circuit Generator Output Voltage Waveform

Figure 11 shows the generator output voltage (boost converter input voltage) and boost converter output current (supercapacitor bank input charging current) for a typical door operation in one direction. For a fixed-duty ratio of 35% and a fairly stiff output voltage of 9 V, the boost converter remained in discontinuous conduction mode until the input voltage reached about 5 V. A further increase of the input voltage resulted in a continuous conduction mode, which tended to clamp the input voltage. As mentioned earlier, this type of operation does not provide maximum power transfer from high-impedance sources such as the generator used here. Closed-loop control would need to be implemented to resolve this issue.

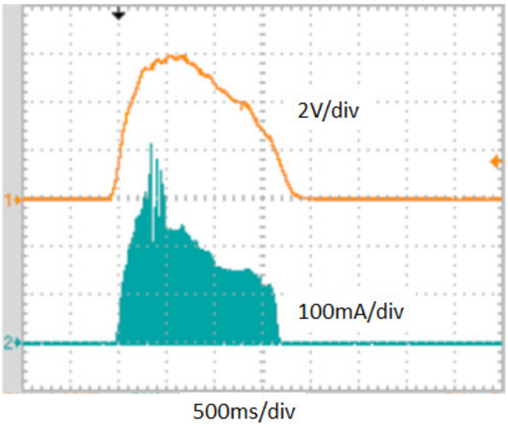

Figure 11. Generator Output Voltage and Boost Converter Output Current Waveforms

Conclusions

A practical system for harvesting the energy produced by human beings opening a door was studied. The goal of capturing enough energy during one door open and close cycle to replace that used by the unlocking mechanism was demonstrated. A simple DC generator with a non-intrusive hinge mounting system provided the means for converting the energy of the swinging door into electrical energy. The amount of energy captured was sufficient to sustain the system, yet the burden placed on the door user was minimal.

The work presented here represents a proof of concept. Many of the practical problems of this method were resolved, though there remained some that will require future work before the system can be deployed for general use. The supercapacitors must be protected from charging beyond their working voltage rating. A mechanism to control self-discharge of the supercapacitors during long periods of door inactivity must also be implemented. More optimal energy extraction could be achieved by employing smarter voltage and/or door speed sensing into the DC-DC converter control loop.

References

[1] Paradiso, J. A., & Starner, T. (2005). Energy Scavenging for Mobile and Wireless Electronics. *IEEE Pervasive Computing, 4*(1), 18-27.

[2] Ottman, G. K., Hofmann, H. F., Bhatt, A. C., & Lesieutre, G. A. (2002). Adaptive Piezoelectric Energy Harvesting Circuit for Wireless Remote Power Supply. *IEEE Transactions on Power Electronics, 17*(5), 669-676.

[3] Yuan, R., Cheng, S., & Arnold, D. (2013). An Energy Harvesting System for Passively Generating Power from Human Activities. *Journal of Micromechanics and Microengineering, 23*(11), 114012.

[4] Litwhiler, D. H., & Gavigan, T. H. (2008). Energy Harvesting: Measurement and Analysis of Swing Doors. *Journal of Engineering Technology*, *25*(2), 26-31.

[5] Yildiz, F. (2011). Energy Harvesting from Passive Human Power. *Journal of Applied Science and Engineering Technology*, 4, 5-16.

[6] Yildiz, F. (2010). Low Power Self Sufficient Wireless Camera System. *International Journal of Modern Engineering*, *10*(2), 31-41.

[7] Carlson, A., & Gisser, D. (1990). *Electrical Engineering: Concepts and Applications*. (2nd ed.). Reading, MA: Addison-Wesley Publishing Co.

[8] Source Engineering motor available from Marlin P. Jones. (n.d.). Retrieved from http://www.mpja.com/24VDC-19RPM-Gearmotor/productinfo/19284%20MD

[9] Mars, P. (2010, July). Using a Small Solar Cell and a Supercapacitor in a Wireless Sensor. *Sensors Magazine*. Retrieved from http://www.sensorsmag.com/networking-communications/energy-harvesting/using-a-small-solar-cell-and-a-supercapacitor-a-wireless-sen-731

[10] Maxwell Technologies. (n.d.). Retrieved from http://www.maxwell.com/products/ultracapacitors/products/hc-series

Biographies

DALE H. LITWHILER is an Associate Professor at Penn State, Berks Campus. He received his B.S. from Penn State University, M.S. from Syracuse University, and Ph.D. from Lehigh University, all in electrical engineering. Prior to beginning his academic career, he worked with IBM Federal Systems and Lockheed Martin Commercial Space Systems as a hardware and software design engineer. Dr. Litwhiler may be reached at dhl10@psu.edu

THOMAS H. GAVIGAN is an Assistant Professor at Penn State, Berks Campus. He received his B.S. in Mechanical Engineering from Drexel University in 1970 and his M.S. in Engineering Mechanics from Penn State in 1977. Mr. Gavigan teaches in the areas of Engineering Mechanics and Engineering Design. Mr. Gavigan may be reached at thg2@psu.edu

STATE-SPACE MODELS WITH KALMAN FILTERING FOR FREEWAY TRAFFIC FORECASTING

Brian Portugais, Boise State University; Mandar Khanal, Boise State University

Abstract

A challenge in road traffic operations and management is that it is not always possible to collect real-time data and process it for use in control algorithms. This is due to the fact that by the time data are processed and a control measure applied, the traffic will have passed. A solution to this is to predict the traffic state based on assessments of current and past measurements. In this study, the authors were able to forecast the state of traffic volume using a Kalman filter that was employed in a dynamic state-space model framework, where parameters of the state were permitted to change with time.

Introduction

The need for forecasting with the Kalman filter arose from a requirement to process traffic data collected in real-time. This is due to the fact that by the time processing is completed and a control measure applied, the traffic will have passed. A solution to this problem is to forecast the traffic state and implement a control measure based on the forecast. A time series in the state-space framework can be considered the output of a dynamic system perturbed by random disturbances such as noise in measurements [1]. Particular cases of general state-space models that are linear and Gaussian are also referred to as dynamic linear models [2], [3]. A Kalman filter (KF) is a recursive data processing algorithm that uses only the previous time-step's prediction with the current measurement in order to make an estimate for the current state [4]. This means the KF does not require previous data to be stored or reprocessed with new measurements. At every iteration, the KF minimizes the variance of the estimation error, making it an optimal estimator if linear and Gaussian conditions are satisfied. A KF was used to analyze traffic data in order to make predictions on traffic volume for Interstate 84 (I-84) in Meridian, Idaho.

The KF works by making a prediction of the future and comparing the estimate with real-time measurements. Along with the prediction, an error covariance is calculated. After a new measurement is taken, the KF calculates an error of the estimate and updates the prediction of the state using the new measurement and the error covariance. Because the recursive algorithm uses only the current measurement and error covariance, online forecasting can be achieved with low computational costs. Five-minute aggregate volume, occupancy, vehicle classification, and average lane speed data were collected on I-84 near the Meridian Road and Eagle Road interchanges. Six Wavetronix™ radar-based sensing devices were used to record data from November 7-15, 2013. Five-minute aggregate volume data, depicted in Figure 1, were collected before the Eagle Road east-bound loop on-ramp on the I-84 mainline. Weekend observations were removed as typical weekend traffic volume is significantly lower and, thus, was not of interest for this current study.

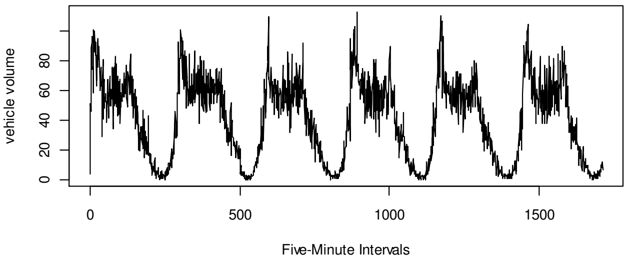

Figure 1. Five-minute Average Volumes with Weekend Data Removed

The work reported here on traffic forecasts is a component of a ramp metering feasibility project, which will use the traffic forecasts in a proactive ramp metering control system.

State-Space Framework

State-space models can be used for modeling univariate non-stationary time series that allow for natural interpretation as a result of trend and seasonal (periodic) components [1], [2]. A local-level model is a time series where observations can be modeled as random fluctuations around a stochastic level (described by a random walk). An extension to the local-level model is one with linear trend and seasonal components. A stochastic local-level model with a seasonal component was constructed and its parameters estimated by maximum-likelihood estimation (MLE) in the 'R' language and environment for statistical computing [3].

The main tasks for the given state-space model were to make inferences on the unobserved traffic state and predict future observations based on part of the observation sequence. Computing the conditional distributions of the traffic state, given the available information and measurements, completes the forecast. In dynamic state-space models, the KF provides the formulas for updating current inferences on the state vector.

Kalman Filter

The general problem that the KF addresses is the estimation of the state, x_t, of a discrete-time controlled process that is governed by the general state equation shown in Equation (1):

$$x_t = G_t x_{t-1} + w_t \tag{1}$$

and, based on measurements for y_t, according to the observation equation shown in Equation (2):

$$y_t = F_t x_t + v_t \tag{2}$$

where, G_t and F_t are known matrices and V_t and V_t are independent white-noise sequences with $w_t \sim \mathcal{N}(0,Q_t)$ and $v_t \sim \mathcal{N}(0,R_t)$.

The KF can be thought of as a recursive two-stage prediction and measurement update algorithm with the following prediction-stage equations [4]:

State estimate (*a priori*):

$$\hat{x}_{t|t-1} = G_t \hat{x}_{t-1|t-1} \tag{3}$$

Error covariance estimate (*a priori*):

$$P_{t|t-1} = G_t P_{t-1|t-1} G_t^T + Q_t \tag{4}$$

The predicted-state estimate (*a priori*) does not include information from the current time step. After a measurement is taken, it is compared with the prediction to refine the state estimate (*a posteriori*). The measurement update equations are as follows:

Measurement innovation:

$$\tilde{y}_t = y_t - F_t \hat{x}_{t|t-1} \tag{5}$$

The innovation covariance:

$$S_t = F_t P_{t|t-1} F_t^T + R_t \tag{6}$$

Kalman filter gain:

$$K_t = P_{t|t-1} F_t^T S_t^{-1} \tag{7}$$

State estimate (*a posteriori*):

$$\hat{x}_{t|t} = \hat{x}_{t|t-1} + K_t \tilde{y}_t \tag{8}$$

Error covariance estimate (*a posteriori*):

$$P_{t|t} = P_{t|t-1} - K_t F_t P_{t|t-1} \tag{9}$$

The Kalman filtering state matrix:

$$G_t = \begin{bmatrix} 1 & 0 \\ 0 & 1 \end{bmatrix} \tag{10}$$

With noise covariance:

$$Q_t = \begin{bmatrix} 12.01 & 0 \\ 0 & -1 \end{bmatrix} \tag{11}$$

Observation design matrix:

$$F_t = \begin{bmatrix} 1 & 1 \end{bmatrix} \tag{12}$$

And observation noise:

$$R_t = [58.75] \tag{13}$$

The KF algorithm computed the one-step-ahead predicted values for the observation of the state vector, together with their variance/covariance matrices. A Kalman smoother computed smoothed values of the state vectors together with their variance/covariance matrices. The smoothing algorithm estimated the state sequence at times 1,...,t, given the data $y_1,\ldots y_t$, by a recursive algorithm. As seen in Figure 2, the KF had a "burn-in" time through about 25, five-minute observation periods. The filter's one-step-ahead forecasts appeared to produce good predictions after this period.

The Kalman smoother's output is shown in Figure 3. The smoothing algorithm is not an ideal solution when online processing is required, since it uses the sequence of observations up to the current observation. It can, however, provide more reliable estimates by using additional measurements made after the time of the estimated state.

Model Validation

The model was validated using ramp flows from the Eagle Road interchange east-bound on-ramp from one day of observations from 6:00am–12:00pm. A smaller data set was chosen with larger deviations in observations to test the KF tuning time and performance. It should be noted that the model was calibrated against the five-minute traffic volume data and validated against the hourly traffic flows. As seen in Figure 4, the model's one-step-ahead forecasts appeared to converge to reasonable estimates relatively early. Note that at the second time step, sensors recorded a negative flow and the KF was able to process the noisy measurement. Smoothed estimates from the KF are shown in Figure 5.

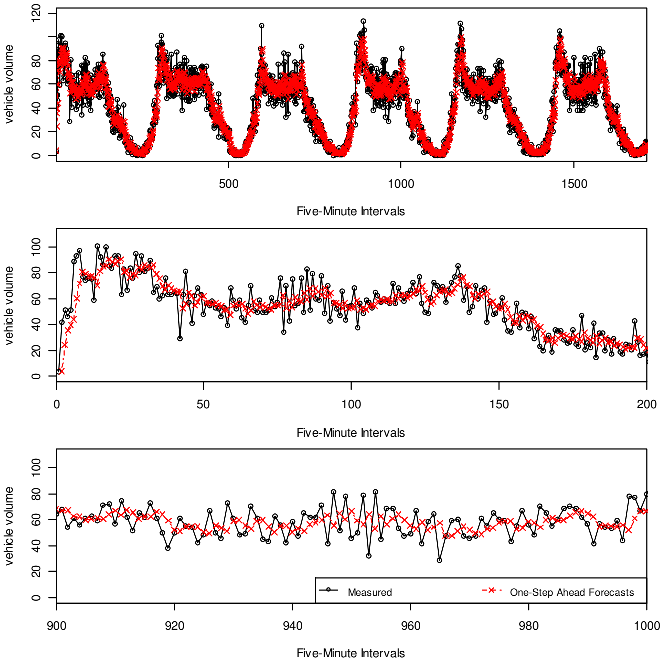

Figure 2. Measured Traffic State with One-step-ahead Forecasts (shown in greater detail in the second and third plots)

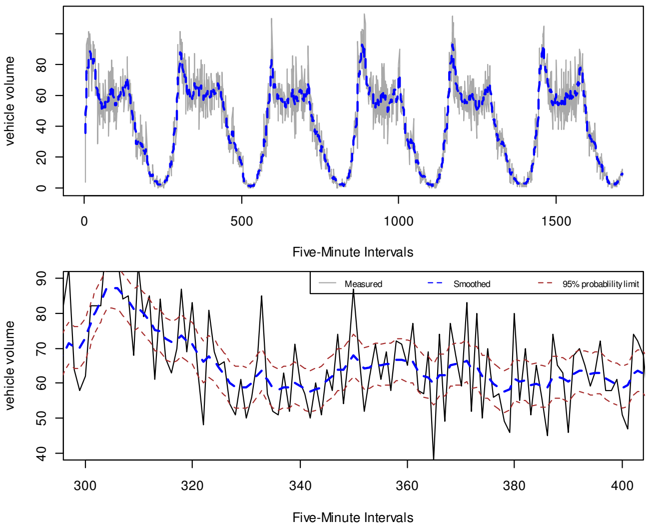

Figure 3. Smoothed State Estimates (shown in greater detail in the second plot)

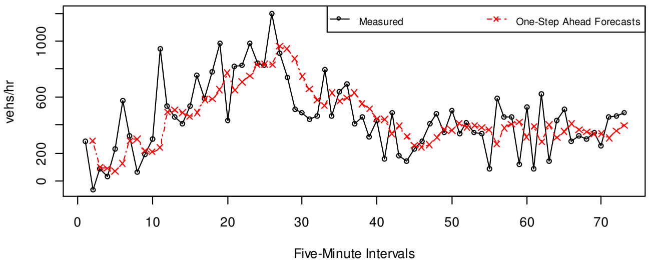

Figure 4. Eagle Road On-ramp One-step-ahead Flow Predictions

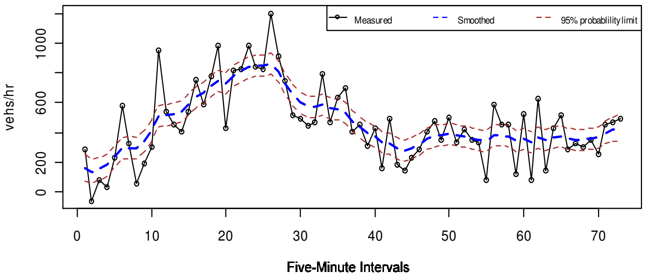

Figure 5. Eagle Road On-ramp Smoothed Estimates

Conclusion

The model used in this study was centered on the idea that the observations, y_t, for traffic volume are incomplete and a noisy function of the unobservable state process, x_t. The unobservable state process was the actual traffic volume which was observed through noisy measurements. The traffic volumes observed on I-84 were characterized by a mixture of smooth gradual changes over a day as well as rapid fluctuations that occurred during a twice-daily, more congested period. To capture these dynamics, the traffic state was modeled in a state-space framework with its predictions performed by a Kalman filter. A polynomial state-space model with stochastic local level and seasonal components parameters was estimated by the maximum likelihood estimation (MLE) method. The uncertainty associated with the MLE's standard errors were 6.11 and 10.70. Plots of the Kalman filter's output appeared to be tuned relatively early and have good performance.

The state-space equations should be formulated to represent the system being observed. Since this is not always possible, the evolution of the predictions from the Kalman filter may not be the minimum error variance. However, the method described in this paper can be used in many areas where estimation of the traffic state is needed, such as dynamic traffic management and control. When applied to travel speeds, this methodology may provide real-time freeway travel time predictions. Real-time, short-term traffic flow forecasting was presented in this paper. Such a procedure can be incorporated into an adaptive ramp metering scheme for better traffic management.

References

[1] Casdagli, M. (1992). A dynamical systems approach to modeling input-output systems. *Nonlinear Modeling and Forecasting*, 265–281.

[2] Petris, G., & Petrone, S. (2011). State space models in R. *Journal of Statistical Software*, *41*(4), 1-25.

[3] Petris, G. (2013). Package dlm: Bayesian and Likelihood Analysis of Dynamic Linear Model, R package version 1.1-3.

[4] Gibbs, B. P. (2011). *Advanced Kalman filtering, least-squares and modeling: a practical handbook*. John Wiley & Sons.

Biographies

BRIAN PORTUGAIS received his B.S. (Civil Engineering, 2012) and M.S. (Civil Engineering, 2014) from Boise State University. Currently, he is a Project Engineer for an Underground Directional Drilling company in the San Francisco Bay Area. His interests are in Cyber Physical Systems for transportation applications, traffic microsimulation, time-series analysis, predictive modeling, and control. Mr. Portugais may be reached at brianportugais@u.boisestate.edu

MANDAR KHANAL is an Associate Professor of Civil Engineering at Boise State University. Dr. Khanal received his M.S. degree in Transportation Engineering from Northwestern University and Ph.D. in Civil Engineering from the University of California at Irvine. At Boise State University, Dr. Khanal teaches various courses and conducts research related to transportation engineering and planning. Dr. Khanal also serves on the Editorial Board of the Journal of Civil and Environmental Engineering and has reviewed papers for various journals in his field. Dr. Khanal may be reached at mkhanal@boisestate.edu

IMPROVING THE USABILITY OF LIQUID MOTOR FUELS: A NEW CONCEPT FOR IN-SITU FUEL VOLATILITY MEASUREMENT

Mebougna L. Drabo, Alabama A&M University; Daniel Fonseca, the University of Alabama;
Marcus D. Ashford, the University of Alabama

Abstract

A probe was developed to quantitatively measure the volatility and distillation profiles of motor fuels. The study sought to show that this novel measurement technique for the validation of volatility characteristics may be appropriate for use by the automotive industry. In this paper, the authors present a validation of the associated model used in the study which, in turn, validates the probe's measurements when compared to those from current industry standard measurement methods. The probe used a horizontal, electrically heated platinum wire, which served as both an element and temperature probe. The basic operating principle behind the probe was based on the fact that more volatile fuels dissipate more energy at a given heating element temperature under nucleate boiling conditions. However, less volatile fuels conversely dissipate more energy at a given temperature within the film boiling regime. The probe quantitatively exhibited this behavior during the initial phase of testing with binary mixtures of isopentane, toluene, and isooctane. These were chosen because they are three of the more prominent ingredients in commercial gasoline. Subsequent testing compared data obtained from the probe to results generated by industry's standard ASTM D86 distillation test. The tests were conducted on identical gasoline blends of various volatilities. A basic quantitative correlation was established between the output of the probe and the ASTM D86 distillation test results. This study validated the concept of a hot-wire volatility sensor, essentially a miniature on-board distillation tester.

Introduction

Automobiles are responsible for a significant portion of the hydrocarbons (HC) released into the environment. In 2002, the U.S. Environmental Protection Agency (EPA) estimated that mobile sources were responsible for 44% of the national inventory of volatile organic compounds [1]. The majority of hydrocarbon combustion emissions from light-duty vehicles occur during transient operation. Changes in temperature and pressure cause phase transitions in liquid fuels, which subsequently result in fueling inaccuracies. In an internal combustion engine, some of the injected fuel will join intake-port and/or in-cylinder fuel films rather than the combustible mix directly. Likewise, these fuel films release fuel to the combustible mix. Figure 1 illustrates the fuel film phenomenon as expressed in the χ-τ Model, shown in Equation (1), commonly used in engine-controller transient-fuel-compensation algorithms [2], [3].

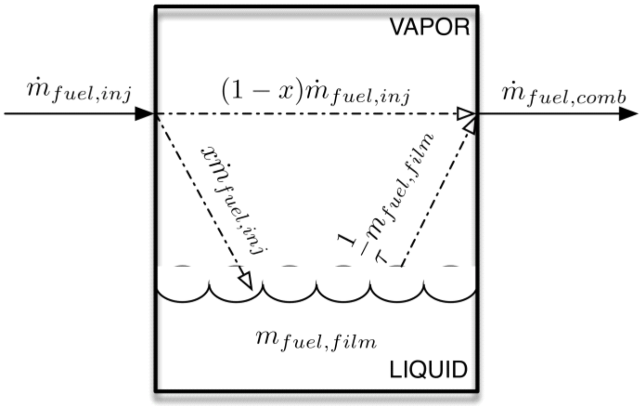

Figure 1. Expression of Fuel Film Mass Dynamics, as Seen in the x-τ Fuel Film Model (adapted from the work by Shan et al. [2])

$$\frac{df_{comb}}{dt}=\frac{1}{\tau}m_{film}+(1-\chi)\frac{df_{inj}}{dt} \qquad (1)$$

In Equation (1), both χ (the fraction of fuel entering the film) and τ (the time constant for fuel leaving the film) are functions of the fuel composition and local temperature and pressure. Fuel entering the combustion chamber is represented by f_{comb}; the amount of fuel injected is represented by f_{inj}; and fuel film mass is given by $m_{fuel,film}$. Under equilibrium conditions, there is zero net fuel flowing to the films; thus, the amount of fuel injected is the same amount entering the combustible mix. Accurate fuel control is trivial; however, engine transients occur at time scales that are much shorter than the time constant for the fuel film to move from one equilibrium state to another. During throttle-opening transients (increasing intake pressure), the film mass grows, creating a lean excursion unless additional fuel is injected as compensation. Conversely, during throttle-closing transients, the decreasing fuel film mass causes rich excursions. These air-fuel excursions increase emissions and fuel consumption, while adversely affecting drivability.

Moreover, the volatility of commercially available pump gasoline varies considerably, both geographically and seasonally. Figure 2 shows the distillation curves of fuels representing typical summer, winter, and hesitation blends. Pertinent distillation parameters are listed in Table 1. A fuel's distillation curve shows how much fuel vaporizes at a particular temperature, when tested per the ASTM D86 distillation protocol. T_{qq} represents the temperature at which *qq%* of the sample has vaporized and E_{rr} represents the percentage of fuel vaporized at temperature *rr*. Hesitation fuel is the lowest volatility fuel typically expected to be found in the fuel supply, and is so named because an engine control scheme not properly calibrated for it tends to cause noticeable "hesitation" in response to throttle opening.

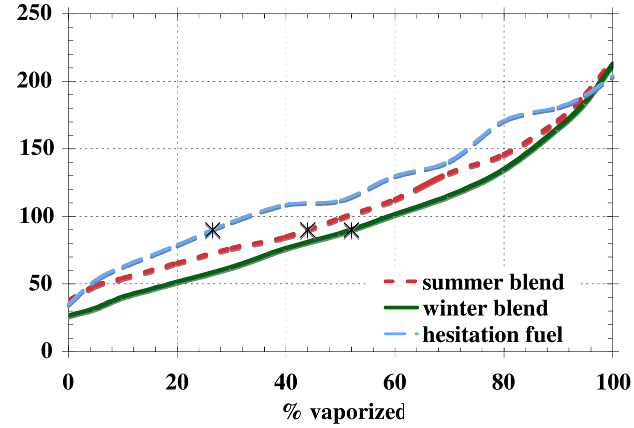

Figure 2. Distillation Curves of Average 2003 U.S. Commercially Available Summer and Winter Gasoline Blends and a Certification "hesitation" Fuel [4]

Table 1. Distillation Parameters of the Summer, Winter, and Hesitation Fuel Blends in Figure 2

	T_{10} [%]	T_{50}	T_{90}	E_{90} [°C]
winter	54	99	171	52
summer	41	88	166	44
hesitation	63	112	181	26

For a given temperature, the amount of fuel vaporization is a strong function of fuel type. Considering vaporization at a typical operating temperature of 90 °C, and comparing E_{90} values (listed in Table 1), the winter fuel has twice the vaporization of hesitation fuel. Regarding the χ-τ model, even if well calibrated, dealing with this kind of fuel variability is very difficult. During cold starts (engine at ambient temperature), the transient fueling problem is exacerbated by extremely rapid transients in both temperature and pressure. Furthermore, at starting temperatures, massive over-fuelling is needed in order to generate a reliable combustible mix. The engine computer has no knowledge of the fuel on board *a priori* and is typically programmed to assume a worst-case scenario: hesitation fuel. Accounting for all of these difficulties, fueling during a cold start can be 10 to 20 times the stoichiometric amount. The catalytic converter can take up to 40 seconds to reach 50% efficiency. Thus, the vast majority of the excess fuel required for starting exits the tailpipe as HC emissions. Measured over the FTP protocol, 60% to 95% of all tailpipe HC emissions occur during the first two minutes after start [3], [5-7].

Modern engine controllers are equipped with transient fuel compensation capability. Additionally, a control scheme that utilizes a fuel distillation profile and vapor/ liquid equilibrium (VLE) behavior would be beneficial in reducing transient fueling inaccuracies. This current study aimed to develop engine-control schemes that employ VLE, either via behavior prediction, property sensing, or manipulation of the fuel itself. The specific objective of the present study was to evaluate the concept of a hot-wire distillation analyzer for in-situ volatility sensing. The operating principle of the sensor is quite simple. In the nucleate boiling range, more volatile liquids boil more vigorously at a given temperature. This manifests itself as higher heat transfer rates. In the film boiling regime, a more volatile fluid readily forms a vapor blanket on the heating surface that tends to restrict conductive and convective heat transfer [8-10]. Thus, more volatile fluids are less able to transfer heat during film boiling.

Experimental Setup

The hot-wire probe assembly is depicted in Figure 3. The test probe consisted of a fine-gauge platinum wire (0.025 mm diameter x 25 mm) attached to two copper tubes held in place by an insulating block. An exposed type-k thermocouple was suspended 4 mm above the wire centerline. The platinum wire was used as both the heating element and temperature sensor.

The probe assembly produces a resistance. This resistance is equivalent to the unknown resistance in a conventional Wheatstone bridge circuit (see Figure 4). The power source was an Agilent 6652A 500 W regulated DC power supply. Data were collected via a National Instruments PCI-6133/ BNC-2120 DAQ board and connector block set at 1 kHz. The voltages measured about the bridge were V_S ($\overline{AC}$), V_G ($\overline{BD}$), and V_{wire} ($\overline{BC}$). The resistance across the probe was calculated by using Equation (2):

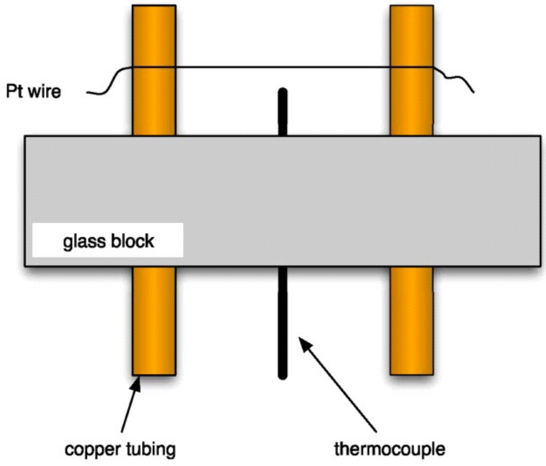

Figure 3. Probe assembly

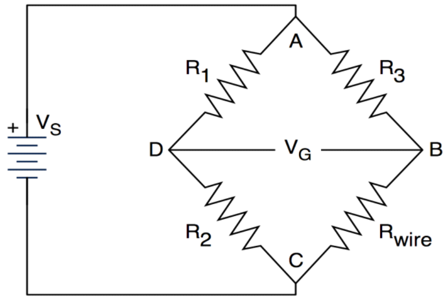

Figure 4. Wheatstone Bridge Setup

$$R_{probe} = R_3 \frac{V_G(R_1 + R_2) + V_S R_2}{V_S R_1 - V_G(R_1 + R_2)} \tag{2}$$

Resistance is related to temperature; as such, by knowing the R_{probe}, the temperature of the probe wire can be determined. The "known" resistors $R_{1\text{–}3}$ (Ohmite E300K10R) were rated at 10 Ω nominal resistance and 300 W.

Probe Calibration

Platinum was chosen as the probe material because of the linear relationship between its resistance and temperature as well as its chemically inert nature. Calibration of the wire was performed by measuring the resistance of the probe assembly while it was submerged in a beaker of oil and heated by a hot plate with a magnetic stirrer. Resistance was measured via an Agilent 34410A digital multimeter and the oil temperature was measured via the probe's integrated thermocouple. A typical calibration curve is shown in Figure 5 and represented by Equation (3):

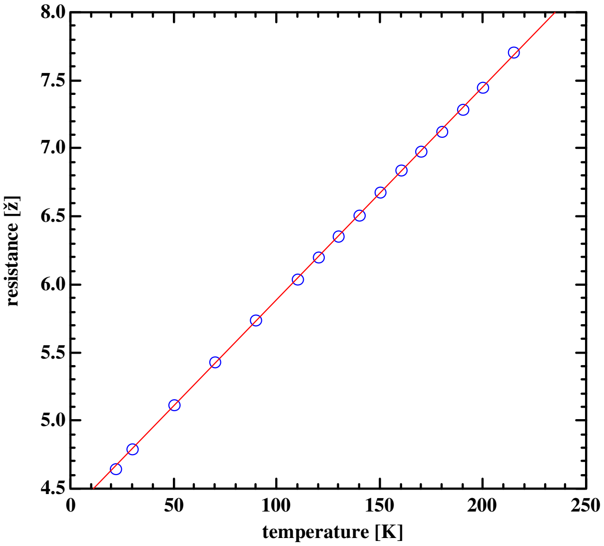

Figure 5. Typical Calibration of the Pt Hot Wire Probe

$$R_{probe}\ [\Omega] = 0.016\ T_{wire}\ [°C] + 4.32 \tag{3}$$

Transposing the calibration equation above, the probe temperature was calculated by using Equation (4):

$$T_{wire}\ [°C] = 62.5\ R_{probe} - 270 \tag{4}$$

The probe was calibrated before and after each test.

Experimental Steps

At the start of each test, resistances $R_{1\text{-}3}$ were recorded and the bridge was balanced. Supply voltage V_S was increased slowly in 0.05 V increments through the nucleate boiling regime and well into the film boiling regime, up to a maximum of 10 V. Extreme care was taken in the film boiling regime to avoid wire breakage. At each new voltage setting, data acquisition was delayed for a few seconds to allow the system to relax in order to eliminate transient effects. The test was stopped if the probe's thermocouple measured a fluid temperature increase of 2 °C. All tests were conducted at room temperature (20-21 °C).

Results and Discussion

This research study was conducted in two phases: testing of known mixtures of neat fuels and testing the hot-wire probe with gasolines of known distillation profiles. The neat fuels were isopentane (2-methylbutane), isooctane (2,2,4-trimethylpentane), and toluene. They were chosen since they are major ingredients of commercially available pump gasoline. Moreover, it was expected that the considerable differences between their boiling points (e.g., isopentane versus isooctane) and molecular structures (e.g., aromatic versus alkane isomer) would allow easier detection and analysis of mixture effects.

Neat Fuels and Boiling Regimes of Interest

Extensive research has been done on nucleate, pool, and film boiling heat transfer [11-13]. Nucleate, transition, and film boiling regimes were considered for this testing, as well as the natural convection regime prior to boiling. Again, the goal here was to determine the feasibility of using this probe to discern a quantifiable measure of volatility. Figure 6(a) shows the power flux from the probe at the associated wire temperatures for binary mixtures of isopentane and toluene at various mixture strengths. The mixtures varied from pure toluene to pure isopentane in steps of 25% by volume. In the natural convection region (pre-boiling), the five mixtures were virtually indistinguishable. This was expected, as the pertinent thermophysical parameters governing natural convection for these hydrocarbons are quite similar.

In the nucleate boiling regime, several observations stood out. Both the 0% and 25% isopentane mixtures showed a distinct transition into nucleate boiling, where the slope of power/temperature abruptly increased significantly, as shown in Figure 6(b). The 50% mixture showed a brief nucleate boiling period, and the 75% and 100% isopentane mixtures transitioned almost immediately from natural convection into film boiling with no definite nucleate boiling range. The boiling point of isopentane is relatively low (28 ° C), so its early transition to film boiling was somewhat expected. In the film regime, there was a clear distinction among mixtures of different volatilities. Thus, the film boiling regime was further investigated in this study. As expected, the lower volatility fluids dissipated more power at a given temperature. Mixtures with a higher fraction of heavier compounds exhibited a more pronounced nucleate boiling range. A higher degree of the nucleate boiling range could have been observed with smaller incremental increases in wire power flux. A longer wire would have facilitated this, but one intrinsic goal was to keep the wire relatively short.

Figures 6(b) and 6(c) show the hot-wire probe power flux over a range of probe wire temperatures for binary mixtures of isooctane/toluene and isopentane/isooctane, respectively. Boiling points for all three neat fuels are listed in Table 2. In the binary mixtures of fuels with large boiling point differences—Figures 6(a) and 6(b)—the probe clearly distinguished the higher and lower volatility mixtures. When boiling points are similar, as shown in Figure 6(c), the probe was much less effective at discerning volatility differences.

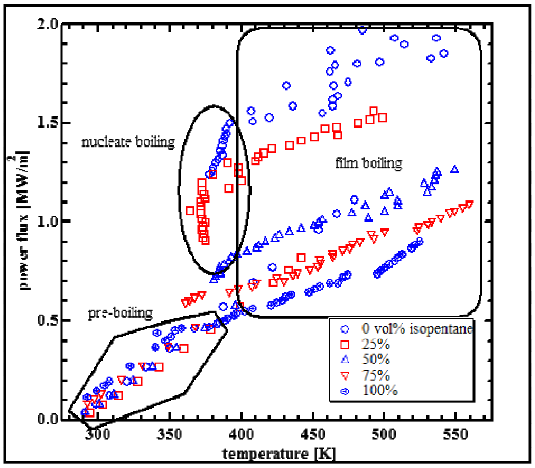

(a) Isopentane/toluene Binary Mixtures

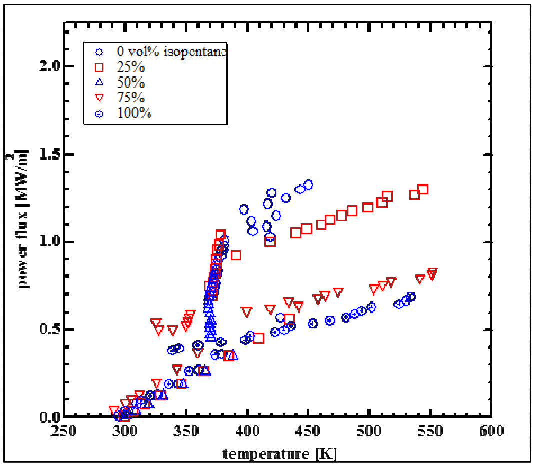

(b) Isopentane/isooctane Binary Mixtures

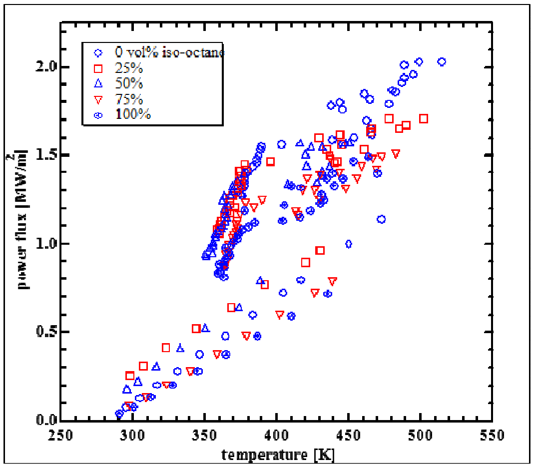

(c) Isooctane/toluene Binary Mixtures

Figure 6. Hot-wire Probe Distillation Results

Table 2. Boiling points of Neat Fuels

isopentane	28 °C
toluene	110.6 °C
isooctane	99.3 °C

Gasolines

Shown in Figure 7(a) are the measured power and resistance levels. These were measured by the probe apparatus for six gasoline blends used in this phase of the study. Figure 7(b) depicts distillation curves of the same fuel blends, generated per industry's standard ASTM D86 distillation test. The legends in both graphs delineate the fuels by the drivability index (i.e., DI = $1.5T_{10} + 3T_{50} + T_{90}$). The various blends were generated by using the ASTM D86 distillation procedure. This procedure was performed on commercially available pump gasoline under various conditions. This selectively drives out light ends. These probe measurements were taken in the film boiling regime. Power-resistance comparisons were used here because these are likely the values measured by vehicular electronics. The probe's readings showed good agreement with the distillation curves. Comparing results from both techniques, the three blends that had similar ASTM distillation profiles (B, C, and D) also had similar signatures, as measured by the probe. Likewise, the probe was able to quantitatively discern blends with distinctly different distillation profiles in much the same fashion as the D86 technique.

Quantitative Regression between Probe Output and ASTM Distillation Test Results

Table 3 shows the average power value of fuels A through F. Table 4 shows the exponential coefficient of each fuel obtained from the ASTM distillation test results. From a linear regression analysis of the average power (AvgP) and the Exponential Coefficient (Figure 8), the volatility coefficient (VC) in Equation (5) was found to be:

$$VC = 0.2533(AvgP) - 0.1929 \qquad (5)$$

The predicted fuel's D86 equation was given by Equation (6):

$$D86_{Temp} = 300e^{vc^{*}\,\alpha} \qquad (6)$$

where, α = [0.1 - 0.9]

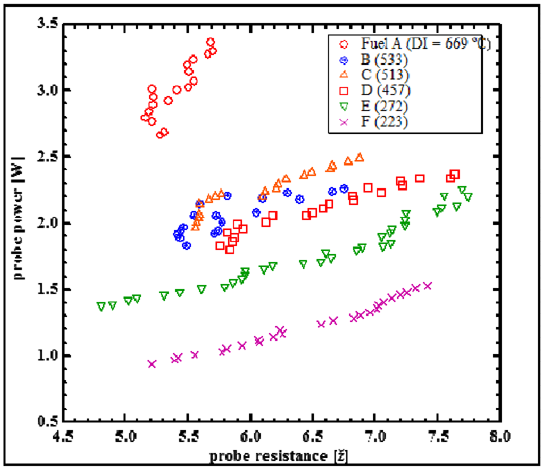

(a) Gasolines of Various Distillation Profiles

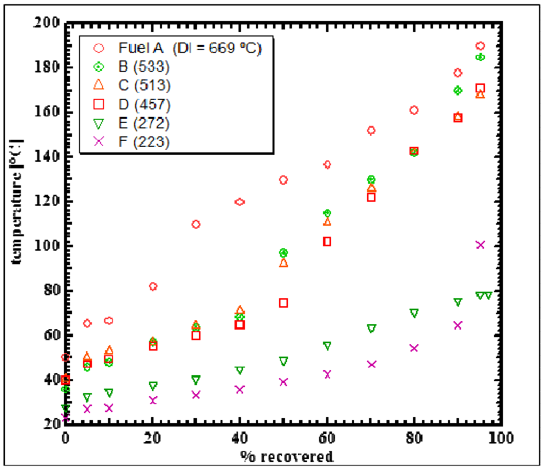

(b) Corresponding ASTM D86 Distillation Profiles

Figure 7. Hot-wire Probe Distillation Results

Table 3. Average Power from the Wire Data

Fuel	Average Power from the wire data
A	3.00
B	2.06
C	2.24
D	2.10
E	1.77
F	1.23

Table 4. Exponential Coefficient of Each Fuel

Fuel	Exponential Coefficient
A	0.516
B	0.418
C	0.403
D	0.384
E	0.159
F	0.103

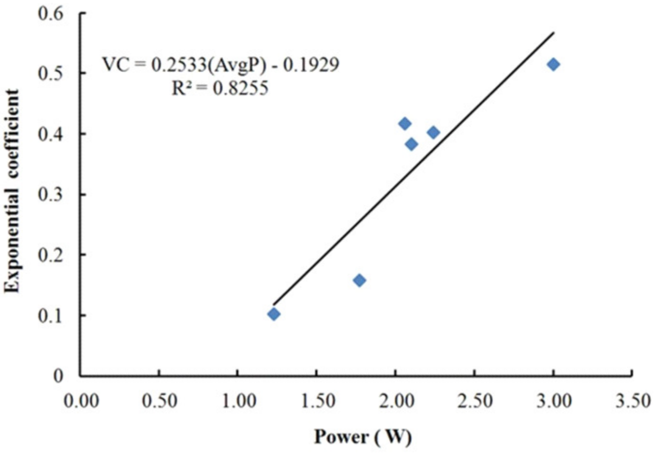

Figure 8. Power versus Exponential Coefficient

By examining the collected wire data, it was concluded that there is an exponential growth in the average $D86_{Temp}$ as the Volatility Coefficient increases. As explained by Emerson [14] and Emerson and Stoto [15], such a relationship is expected from empirical data that is linearly dependent on a second-degree causal factor, as it is the case of the $D86_{Temp}$ and the calculated Average Power. Linearity between the volatility coefficient and the average power was clearly established by the generated plots and resulting regression coefficients (see Figures 9-11). The exponential regression between the $D86_{Temp}$ and the dependent variable from this linear relationship (i.e., the VC) was determined by the mathematical transformation suggested by Emerson and Stoto [15].

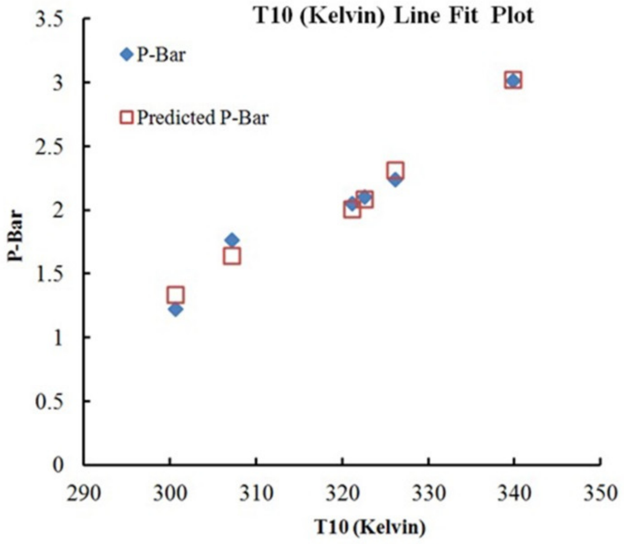

Figure 9. T10 Line Fit Plot

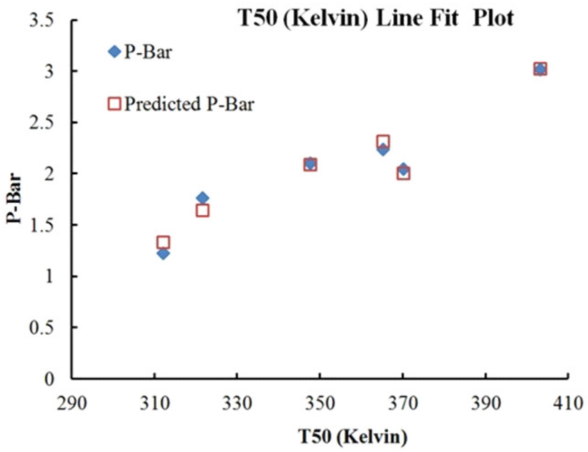

Figure 10. T50 Line Fit Plot

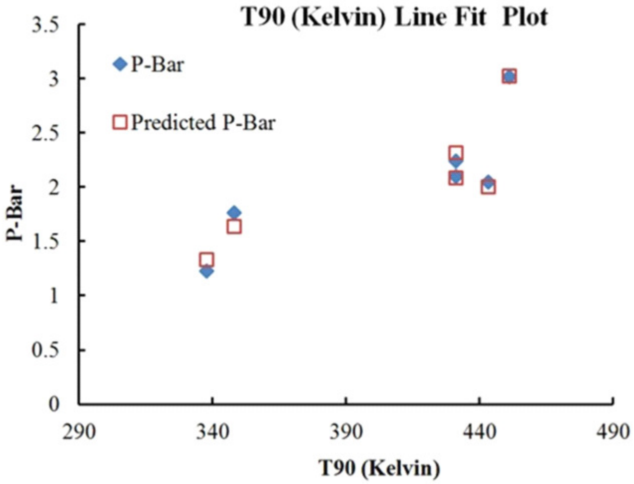

Figure 11. T90 Line Fit Plot

Shown in Figure 12 are the ASTM D86 distillation profile and the corresponding model prediction results. The prediction model shows good results in certain areas. For example, fuels E and F showed good model estimates, but the model did not perform well at the extremes. Evaluating the model at the extremes is an area for future research. The next step in this study is to test different fuel blends of known composition in order to determine if there is a way to express the coefficients in terms of the expected thermo-physical parameters of the constituents. These constituents can be heat of vaporization, mole (or mass) fraction, boiling point, specific heat, and surface tension.

Conclusions

In this paper, the authors described the development of a proof-of-concept for a distillation testing and volatility-sensing probe, based on measuring the amount of boiling heat transfer from a heating element at a given temperature. Through testing with binary mixtures of known ratios of isopentane/toluene/isooctane, the probe was able to quantitatively discern the differences between volatility of the mixtures and distillation profiles. It was determined that the most effective regime for probe operation was that of film boiling.

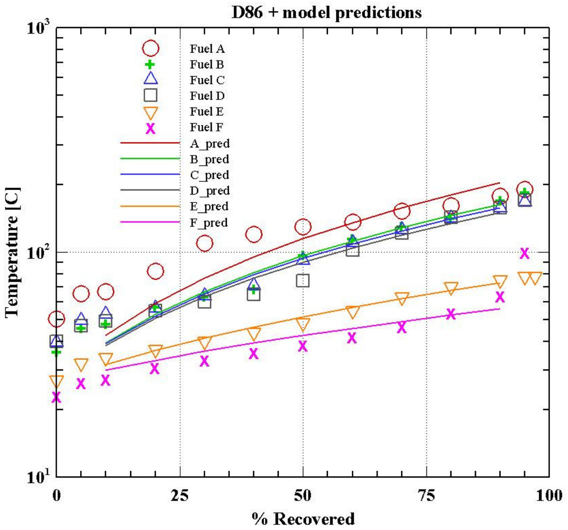

Figure 12. ASTM D86 Distillation Profiles and Model Predictions

Probe performance was also tested with six gasoline blends of different volatilities. The results were compared to those obtained from the industry standard ASTM D86 distillation test. The probe was able to distinguish fuel blends of different distillation profiles in much the same way as the D86 test. Blends that had similar D86 distillation profiles generated similar profiles with the hot-wire probe. Likewise, the probe results varied in magnitude with nearly identical trends to the D86 results. A basic quantitative correlation was established between the probe's output and the ASTM D86 distillation test results. The prediction model showed good results at certain areas but not at the extremes. Future work is aimed at determining if the correlation coefficient can be inferred as a function of the relevant thermophysical and transport properties of the fuel itself.

Acknowledgements

This study was supported by the National Science Foundation (under award Number 535791) and the University of Alabama. The opinions and findings presented herein do not necessarily reflect the views of NSF or any other Federal or State agencies.

References

[1] Environmental Protection Agency. (2005). 1970-2002 Average Annual Emissions, All Criteria Pollutants in MS Excel. Retrieved October 30, 2006, from http://www.epa.gov/ttn/chief/trends/index.html

[2] Shan, X., Burl, J., Jankovic, M., & Cooper, S. (2008). Transient Fuel X-Tau Parameter Estimation Using Short Time Fourier Transform. *SAE Technical Paper*, doi:10.4271/2008-01-1305.

[3] Luan, Y., Henein, N., & Tagomori, M. (2006). Port-Fuel-Injection Gasoline Engine Cold Start Fuel Calibration. *SAE Technical Paper*. doi:10.4271/2006-01-1052.

[4] Ashford, M.D. (2004). *An on-board distillation system to reduce cold-start hydrocarbon emissions from gasoline internal combustion engines*. Doctoral dissertation, The University of Texas at Austin.

[5] Ashford, M. D., & Matthews, R. (2006). On-Board Generation of a Highly Volatile Starting Fuel to Reduce Automobile Cold-Start Emissions. *Environmental Science and Technology*, *40*(18), 5770-5777.

[6] Santoso, H., & Cheng, W. (2002). Mixture Preparation and Hydrocarbon Emissions Behaviors in the First Cycle of SI Engine Cranking. *SAE Technical Paper*. doi:10.4271/2002-02-2805.

[7] Kane, E., Huang, Y., Mehta, D., Frey, C., Tillerson, M., Chavis, Z., et al. (2001). Refinement of a Dedicated E85 1999 Silverado with Emphasis on Cold Start and Cold Driveability. *SAE Technical Paper*. doi:10.4271/ 2001-01-0679.

[8] Hahne, E. (1977). *Heat Transfer in Boiling*. Academic Press.

[9] Incropera, F. P., & De Witt, D. P. (2001). *Fundamentals of Heat and Mass Transfer*. (5th ed.). Wiley.

[10] Pais, C., & Webb, L. (1991). Literature Survey on Single Tube Pool Boiling on Enhanced Surfaces. *ASHRAE Transactions, 97*, 79-89.

[11] Kunugi, T. (2012). Brief Review of Latest Direct Numerical Simulation on Pool and Film Boiling. *Nuclear Engineering and Technology*, *44*(8), 847-854.

[12] Zhou, L., Wei, L., Du, X., Yang, Y., Jiang, P., & Wang, B. (2014). Effects of Nanoparticle Behaviors and Interfacial Characteristics on Subcooled Nucleate Pool Boiling Over Microwire. *Experimental Thermal and Fluid Sciences, 57*, 310-316.

[13] Sohel Murshed, S. M., Nieto de Castro, C. A., Lourenço, M. J. V., Lopes, M. L. M., & Santos, F. J. V. (2011). A Review of Boiling and Convective Heat Transfer with Nanofluids. *Renewable and Sustainable Energy Reviews*, *15*, 2342-2354.

[14] Emerson, J. D. (1983). Mathematical aspects of transformation. In D. C. Hoaglin, F. Mosteller, & J. W. Tukey (Eds.), *Understanding Robust and Exploratory Data Analysis* (pp. 247-282). New York, NY: John Wiley.

[15] Emerson, J. D., & Stoto, M. A. (1983). Transforming data. In D. C. Hoaglin, F. Mosteller, & J. W. Tukey (Eds.), *Understanding Robust and Exploratory Data Analysis* (pp. 97-128). New York, NY: John Wiley.

Biographies

MEBOUGNA L. DRABO is an Assistant Professor of Mechanical Engineering at Alabama A&M University. Dr. Drabo may be reached at mebougna.drabo@aamu.edu

DANIEL FONSECA is an Associate Professor of Mechanical Engineering at The University of Alabama. His research interests include manufacturing systems, reliability engineering, and the application of artificial intelligence (AI) techniques to complex engineering domains. Dr. Fonseca received B.S. and M.S degrees in Industrial Engineering from the University of Alabama, and M.S. and Ph.D. degrees in Engineering Science from Louisiana State University. Prior to joining the faculty of the University of Alabama, Dr. Fonseca worked as a professor and industrial consultant at the Monterrey Institute of Technology in Mexico. Dr. Fonseca may be reached at dfonseca@eng.ua.edu

MARCUS D. ASHFORD is an Associate Professor of Mechanical Engineering at Alabama in Tuscaloosa. His research interests include alternative fuel and hydrogen engine/vehicle applications, advanced combustion IC engine concepts, internal combustion engine control schemes, IC engine emission reduction and efficiency improvement, and combustion and fire science. Dr. Ashford may be reached at marcus.ashford@eng.ua.edu

COMPARISON OF AN ANALYTICAL HIERARCHY PROCESS AND FUZZY AXIOMATIC DESIGN FOR SELECTING APPROPRIATE PHOTOVOLTAIC MODULES FOR ONBOARD VEHICLE DESIGN

Mahmoud Abdelhamid, Clemson University; Ala Qattawi, University of California, Merced; Rajendra Singh, Clemson University;
Imtiaz Haque, Clemson University

Abstract

In this paper, the authors present an overview of the available commercial photovoltaic (PV) module options for powering onboard vehicle applications. The authors used two decision-making methodologies to determine the evaluation factors and the decision-making criteria necessary for assessing the suitability of a particular PV module type. In both the analytical hierarchy process (AHP) and the fuzzy axiomatic design (AD), the authors used at the input stage quality function deployment (QFD) to determine customer requirements for a vehicle with PV module capabilities. This approach is innovative in that evaluation depended upon data collected from PV manufacturers' datasheets. This approach is novel in that: 1) the AHP and fuzzy AD processes were used as decision-making methodologies to select the optimum PV module type to power a vehicle; 2) the QFD and AHP hybrid approaches were compared with the QFD and fuzzy AD hybrid approaches; and, 3) commercial PV market data, not from experts, were used for comparison, as in traditional research. A benchmark of both approaches determined differing results if the evaluation was conducted with both methods using identical data with different natures (i.e., precise versus fuzzy). Results showed that for onboard vehicle applications, the most suitable PV module option was mono-crystalline silicon and the least suitable option was cadmium telluride.

Introduction

Gasoline-powered internal combustion engines have been the mainstay of the automobile industry for over a century. For example, the U.S. transportation sector consumed approximately 71% of the total petroleum used in 2013 [1]. Unfortunately, this technology is now a fundamental hindrance to global economic growth and is entirely inadequate for meeting the long-term energy needs of a growing world economy. The world's population will reach nearly 9 billion in 2040 [2], with a concurrent increase in the number of individuals who can afford vehicles. This population growth will in turn lead to an increase in energy demands, a problem further complicated by the expected increase in petroleum products combined with large and unpredictable fluctuations in availability. Perhaps the greatest adverse effect to the earth's climate is the total energy-related CO_2 vehicular emissions released in that each vehicle emits roughly 5.1 metric tons of CO_2 annually [3].

Switching from the present transportation system to one that uses sustainable, renewable, and clean energy sources will ensure U.S. energy independence with a corresponding low environmental impact. Solar-generated electricity is a prominent candidate for replacing current U.S. energy supplies because of its clean nature, abundance, and supply of inexhaustible and cost-free sunlight. Solar electricity could be generated by photovoltaic (PV) cells, which is a specialized semiconductor diode (PN-Junction) that converts electromagnetic radiation near the visible range into direct current (DC) electricity. The PV module is a packaged assembly of individual PV cells. The cost of PV modules has declined significantly over the past 20 years, from $5.7 per watt in the early nineties to approximately $0.65 per watt currently [4]. The cost of solar electricity will be competitive with other sources of energy by 2020 [5]. As such, the cumulative installed solar PV capacity is firmly moving to the terawatt scale and is a prominent candidate for solving 21st-century energy challenges [6-10]. The continuous increases in PV cell efficiencies [11], improving manufacturing and inspection technologies to make defect-free PV modules [12], and reductions in cost are making PVs particularly useful in powering the next generation of individual transportation solutions. The PV modules can provide energy to the vehicle either via onboard or off-board applications. In off-board applications, the PV is the source of energy for the charging station. In onboard applications, the PV modules are vehicle mounted either to assist in propulsion or to run a specific vehicle application. Applications for onboard PV modules have been the subject of much research. The approaches vary in terms of the configuration and the specifications of the system [13-17].

Thus far, however, no research has been undertaken to determine the decision-making methodology for selecting the best commercial PV module type for onboard vehicle applications. The objective of this paper was to provide an overview of different commercial PV module options to power vehicle applications, and that of the decision-making criteria for selecting the optimum PV module types for onboard vehicle applications. In this study, two decision-making methodologies were evaluated: the analytical hierarchy process (AHP) [18] and the fuzzy axiomatic design (AD) [19], [20]. In both approaches, the quality function deployment (QFD) [21] was incorporated as the input stage in order to capture customer requirements for vehicle applications with PV module capabilities. The novel use of each of these approaches will benchmark each of the others in order to minimize subjectivity, which usually is the most difficult challenge.

Background of AHP, Fuzzy AD, and QFD

AHP and fuzzy AD are multi-criteria decision-making (MCDM) methods used to evaluate multiple and conflicting criteria. Selecting the best PV module for vehicle applications shares the common MCDM problem characteristics [22] in that the conflicting objective or attribute criteria, and the incommensurable unit of measurements, require choosing a solution from a list of alternatives. The AHP allows decision makers to structure the decision-making case in attribute hierarchies. These establish a relationship between objective function and criteria in the first hierarchy level and between the criteria and alternatives in the second. The AHP is superior in that it combines both qualitative and quantitative approaches. In the qualitative sense, it breaks down an unstructured problem into a systematic decision hierarchy, followed by a quantitative ranking using numerical ranks and weights in which a pairwise comparison determines the local and the global priority weights in order to obtain a ranking of proposed alternatives. Some of the most recent applications of AHP rank various renewable and non-renewable electricity production technologies [23]: selecting the most appropriate package of solar home systems for rural electrification [24]; selecting the solar-thermal power plant investment projects [25]; and evaluating different power plants [26]. As part of this study, the authors used AHP to rank the different micro-crack non-destructive inspection tools for automated PV production stages [27].

Designers can use the AD approach to create a theoretical foundation based on logical and rational thought processes to reduce the random search and trial-and-error processes, and then determine the best design among those proposed designs [19]. The most important concept in AD is the existence of the design axioms [19], [20]. The first axiom, which is the independence axiom, maintains the independence of functional requirements (FRs). The second axiom is the information axiom, which involves minimizing the information content. The FR is the minimum set of independent requirements that the design must satisfy. The first axiom states that a design solution should not allow one FR to affect the other FRs. The second axiom provides the theoretical basis for design optimization by providing a quantitative measure of the merits of a given design. The design with the least information content is the best choice. The AD was applied to a fuzzy environment in which there were fuzzy data instead of precise data. Some of the applications of fuzzy AD to decision-making problems were selected from renewable energy alternatives [28]: evaluation energy policies [29]; ergonomic compatibility evaluation of advanced manufacturing technology [30]; and, the best green supplier manufacturing companies [31].

The QFD [21] is a method that the designer may use to develop a new product or service by learning about customer needs, which in QFD is known as the voice of the customer (VOC). The aim of QFD is to incorporate the VOC into the engineering characteristics of a specific product or a service. The planners can then prioritize each product or service attribute in order to set the levels necessary for achieving these characteristics. The QFD tool has been used for many applications [32]. Some authors have used QFD with the AHP tool for various situations [33]. In this study, the authors implemented a QFD and AHP combination as a decision-making tool for selecting materials for automobile bodies [34] and for developing a knowledge-based system to design an automotive production line [35].

Kahraman et al. [36] undertook a comparative study of fuzzy AHP and fuzzy AD and used this approach for selecting the best renewable energy sources, both of which were used in a fuzzy environment with all evaluations based on expert linguistic terms or fuzzy numbers. The proposed approach in this current study goes beyond that work. Unlike conventional fuzzy studies, i) the AHP and fuzzy AD were used for the PV module selection for onboard vehicle application; ii) the pairwise comparison in the AHP depends on data collected from PV manufacturers' datasheets and not numbers from experts, as in typical fuzzy AHP; iii) the fuzzy data applied to AD were from the same dataset, which the authors collected from PV manufacturers; and, iv) the authors conducted a comparative study of the two approaches after adding the QFD as the input stage. There are many other MCDM models, all of which have their strengths, weaknesses, and areas of application, and none of which is truly superior [37]. Thus far, no MCMD has been applied to this current problem and the proposed approaches will fill this gap in the literature. In this study, the AHP and the fuzzy AD were chosen as the proposed decision-making methodologies for the following reasons: a) it allowed selection of the optimum PV module type for onboard vehicle use, which is an MCMD problem with conflicting objectives; b) it used precise data for a robust pairwise comparison of the AHP decision tool; c) the fuzzy AD approach was used to conduct evaluations in fuzzy environments in order to capture the entire commercial PV market data; d) the QFD can be incorporated into the input stage for both approaches reflecting the VOC and reducing the subjectivity of traditional methods; and, e) the authors used the data from PV manufacturers' datasheets in the proposed evaluation, thus reducing subjectivity and permitting benchmarking of both approaches using data that are both precise and fuzzy.

Methodology

PV Module Types

Though more than 25 PV cell types exist [11], not all are available for commercial use. They are also unsuitable for vehicle applications because of cost, availability of raw materials, reliability, stability, and lifetime limitations. Here, the authors outline the different commercial PV technologies, emphasizing the strengths and challenges of each PV module type. This overview is essential for decision-making as it highlights the possible search space for the MCDM tools. The current commercial PV modules are bulk silicon (wafer-based) or thin films and could be deposited on rigid or flexible substrates. The total global PV module production in 2013 was 40 GW, of which the silicon bulk PV modules (mono-crystalline silicon, Mono-Si, and multi-crystalline silicon, Multi-Si) shipped was 89.58% of the total, and thin films (cadmium telluride, CdTe, copper indium gallium selenide, CIGS, and amorphous silicon a-Si) solar cells comprised the remaining 10.42% [38]. Mono-Si and Multi-Si PV modules are advantageous in that they use silicon, the second most abundant element in the earth's crust. Silicon is also a well-researched and well-understood element in the periodic table, due to its use in the semiconductor industry at around $350 billion.

One of the authors in this study predicted the dominance of silicon as a PV material in 1980 [39]; then restated this prediction in 2009 [40], that the abundance of this raw material is a key requirement for terrestrial PV. CdTe PV modules have the inherent disadvantage of using Cd, which is toxic, and being combined with a limited supply of Te [7]. To handle CdTe module toxicity, some companies recycle this material, but reclamation is both difficult and expensive. CIGS PV modules are much safer than CdTe because of the miniscule amounts of cadmium sulfide. The most critical drawback of CIGS modules is the very limited supply and expense of indium, which constitutes the primary element of this module [7]. The advantages of an a-Si PV module, in addition to the abundance of silicon, is that the manufacturing techniques and tools used to deposit a-Si and related materials are similar to liquid crystal display (LCD) manufacturing. Additionally, a-Si PV modules also have the advantage of operating well in both hot and cloudy climates and being compatible with building-integrated PVs. The disordered structure of a-Si initially degrades a-Si PV module efficiency, which stabilizes at some point. The efficiency of stabilized commercial single-junction a-Si PV modules is much lower than the single-junction CdTe and CIGS PV modules. However, the performance of commercial double-junction a-Si PV modules is comparable with CdTe and CIGS PV modules.

In this study, the top five commercial PV types were analyzed. Other PV module types—such as multi-junction cells and single-junction gallium arsenide (GaAs) cells, organic photovoltaic (OPV) cells, dye-sensitized solar cells (DSSC), and quantum dot cells—were excluded from this study for the following reasons: Although GaAs is the most efficient PV type, it is also the most expensive, and mainly used in space applications. The relatively low efficiencies of OPVs, DSSCs, and quantum dot cells make them particularly poor candidates for the large-scale PV generation of electricity. Specifically, DSSCs do not exceed 7 cm^2, which makes it very difficult to build large-area modules because of the large amount of energy lost during connection [8]. OPV is unreliable with a cell lifetime of only 3 to 4 years [41], compared to other PV types, which have a 20-30 year lifespan. In this study, six evaluation criteria were proposed based on QFD, and used for benchmarking and evaluating PV modules for vehicle applications, as below:

(i) Power density, which is defined as PV module power generated per area (W/m^2) at standard test conditions (STC). Limited vehicle surface areas make higher density modules preferable. This factor is related to PV module efficiency, which is the PV wattage generated per area divided by 1000 W/m^2 at STC.
(ii) Specific weight, which is the PV module wattage generated per weight (W/kg). A high specific weight is required, since the installation of PV modules adds extra weight of an automobile body and increases the vehicle curb weight, thereby affecting vehicle performance.
(iii) Power temperature coefficient (PC) is measured as -% per ºC, which is related to PV module reliability. Temperature increases reduce the performance

of all PV module types. A module with a lower PC factor is more reliable.

(iv) Flexible substrates are used with thin-film technology, making the installation of PV modules on the vehicle body easier.

(v) Health and safety considerations using silicon obviates any supply chain difficulties. Unlike silicon, Cd-based CdTe PV modules present environmental and human hazards. For that, the CdTe module could be banned in the future in a few countries and is not even a preferred choice worldwide [42].

(vi) The lifecycle cost (LCC) of electricity is defined as the total cost of the PV system per total energy generated through the PV system in the lifecycle of the unit (¢ per kWh). Given this constraint, the installation surface area on the vehicle is determined as follows, where LCC is calculated using Equations (1) and (2) [43], [44]:

$$\text{LCC}\,(\$/\text{kWh}) = \frac{\text{Cost}\sum\begin{matrix}[\text{PV Module} + \text{installation} + \text{land} + \\ \text{Energy storage} + \text{maintenance}]\end{matrix}}{\text{Total energy generated}} \qquad (1)$$

The total energy generated over a system's lifetime can be calculated using Equation (2):

$$\text{Totalenergygenerated} = \text{I} \times \eta \times PR \times LT \times A^{'} \qquad (2)$$

where, I is the irradiation (kWh/m^2/yr), which is the average energy flux from the sun and depends on the installation location; η is the lifetime average module efficiency (%); PR is the performance ratio LT is the system lifetime in a year; and A is the total module area (m^2).

In order to evaluate adequately the PV options, the constraints of geographical location, mounting configuration, and a tracking/orientation option should be identical in any comparison. In addition, the structural design of the solar panels should fulfill many load demands since the solar panels may be subject to strong wind, snow, and many other effects. Aly and Bitsuamlak [45], [46] evaluated wind-induced pressure on solar panels, which are beyond the scope of this paper. In order to evaluate the different PV module types, the authors collected the required performance specifications for each PV module that reflect each of the proposed evaluation factors using datasheets from many PV manufacturers (see Figures 1 and 2). The data gathered from 27 PV manufacturers (eight Multi-Si, eight Mono-Si, three a-Si, three CdTe, and five CIGS) reflect the current PV market. Based on Figures 1 and 2, the results for power density, specific weight, and PC factors are tabulated in Table 1.

Table 1 data are from manufacturers and reflect the minimum and maximum values, and the average values for each PV type. The flexibility and health/safety concerns were non-numerical values. The bulk silicon PV types are rigid, and the thin-film PVs deposited on rigid or flexible substrates depend on packaging. The results, in regards to LCC of electricity (see Table 2), were calculated with the following assumptions: the cost of land was not factored in, since the PV modules were mounted on the vehicle's body. In addition, the installation, maintenance, and energy storage costs were assumed to be similar for all PV module types. The current prices of commercial PV modules (excluding tax) in $/W for the bulk silicon solar modules were 0.55, 0.657, and 0.92, while thin-film solar modules were slightly lower at 0.49, 0.583, and 0.87 for low, average and, high scenarios, respectively [47]. These prices were set by the manufacturers, with Chinese-made PV modules being the least expensive.

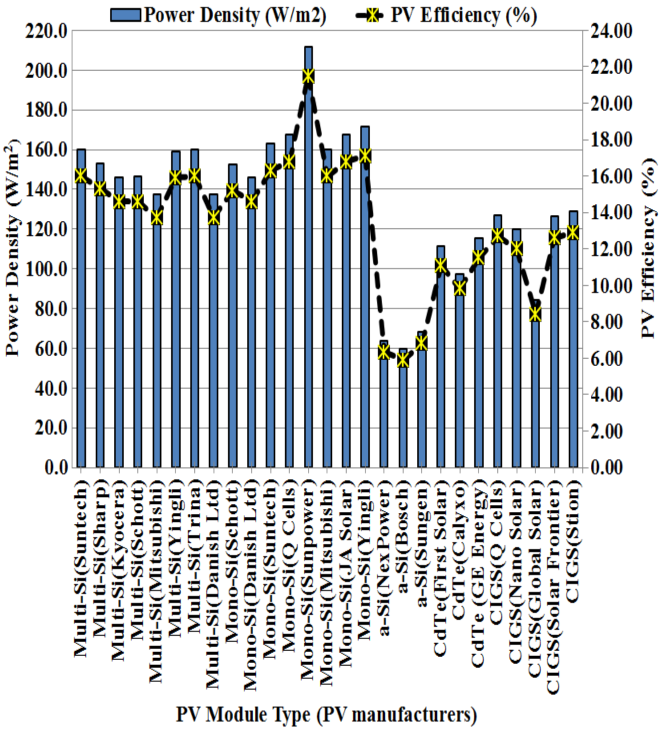

Figure 1. Power Density and Efficiency Factors of the Commercial PV Module Types

The cost of a PV module per energy generated was calculated using three scenarios: best, intermediate, and worst-case. The calculation was based on Equations (1) and (2), and the assumed parameters were I=1800 kWh/m^2/yr, based on U.S. location; PR=0.75; and, n=30 years [48]. Furthermore, η was based on degradation over the system's lifetime by 0.5% (relative to the initial efficiency) per year [48]. The initial PV efficiency was considered equal to the average

PV efficiency in Table 1. Sample LCC calculations are shown in Table 2 with respect to Multi-Si PV modules; the LCC values for all other PV types was done in a similar manner and tabulated in Table 1.

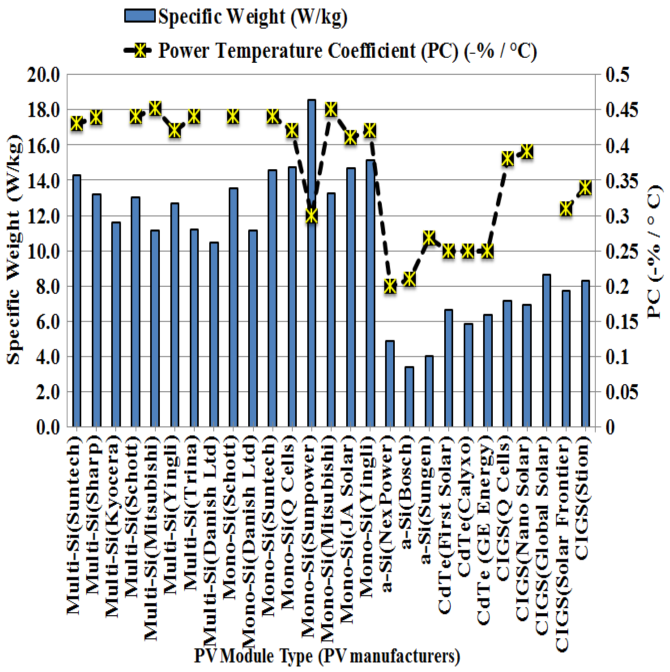

Figure 2. Specific Weight and PC Factors of the Commercial PV Module Types

The QFD and AHP Approaches

The incorporation of the QFD and AHP approaches can be done through a three-step process in order to overcome the well-known dependence of AHP on subjective pairwise comparisons. A knowledge-based database was used in the pairwise comparison, where the comparison of each criterion was based upon manufacturer datasheets. To make the pairwise comparison more robust, the authors compared the average values from different manufacturers of each PV module type in Table 1. Finally, the QFD approach was incorporated as an input stage to the AHP to assign weights per vehicle customer preference. Figure 3 shows the proposed QFD/AHP combined procedure. The QFD structure is shown in Table 3. There are five QFD components. The first are the engineering requirements specified by the *How* window, which are the PV FRs.

Next is the customer need (VOC) represented by the vehicle requirements and specified by the *What* window. Third are the weights for customer needs, shown as an importance percentage of specific vehicle requirements, with the total importance weights for all VOC requirements equaling 100%. Fourth are the combined *How*'s and *What*'s using a relation matrix of three scores (1, 3, and 9), where a score of 1 is the lowest between the specific column in the *How* window and the specific row in the *What* window; a score of 3 is the mean medium impact; and a score of 9 is a strong impact.

Table 1. Performance Data from PV Manufacturers' Datasheets and LCC Results

PV Module Type	Power Density (W/m^2)			Specific Weight (W/kg)			PC (-%/°C)			Life cycle cost (LCC) of electricity(¢/kWh)		
	Min.	Max	Avg.	Min.	Max	Avg.	Min.	Max	Avg.	Min.	Max	Avg.
Multi-Si	137.2	159.8	149.9	10.5	14.3	12.2	0.42	0.452	0.4368	1.570	2.625	1.875
Mono-Si	146.1	211.6	167.5	11.1	18.5	14.4	0.3	0.44	0.411	1.557	2.603	1.859
a-Si	59.4	68.2	63.7	3.4	4.9	4.1	0.268	0.2	0.226	1.394	2.477	1.660
CdTe	97.2	115.3	107.9	5.8	6.7	6.3	0.25	0.25	0.25	1.389	2.465	1.652
CIGS	84.1	128.9	117.1	6.9	8.6	7.8	0.31	0.39	0.355	1.389	2.465	1.652

Table 2. LCC Calculations with Respect to Multi-Si PV Modules

PV Module Type	Module price ($/W) (excluded tax) [47]	Module price after 7 % sales tax ($/W)	PV Module Average Power Density (W/m^2) [Table 1]	Cost PV Module ($\$/m^2$)	PV Module Average initial efficiency (%) [Figure 1]	PV Module Average Lifetime efficiency (%)	Total energy generated (KWh)	Cost PV per Total Energy (¢/KWh)
Low LCC Scenario	0.550	0.589	149.900	88.216	14.900	13.877	5620	1.570
Average LCC Scenario	0.657	0.703	149.900	105.378	14.900	13.877	5620	1.875
High LCC Scenario	0.920	0.984	149.900	147.562	14.900	13.877	5620	2.625

Table 3. Proposed QFD Structure

Relative Weight (%)	Customer Importance	Functional Requirement (FR) / EV Customer Needs	Power Density (W/m^2)	Specific Weight (W/kg)	Reliability to Temp.	Envir./ health/ safety	Flexibility	Cost ($/kWh)
20	3	High Range	9	3	3			
30	2	Help Save Money	9	3	3			9
35	1	Eco-Friendly				9		
15	4	Aesthetic (Good looking)					9	
		Evaluation	450	150	150	315	135	270
		Relative Evaluation (%)	30.6	10.2	10.2	21.4	9.2	18.4

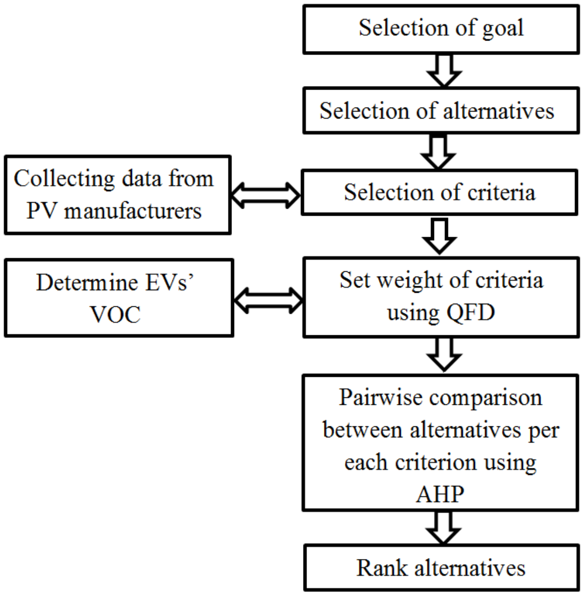

Figure 3. Steps for Applying QFD with AHP

For instance, a score of 35 is assigned a label of "Eco-friendly", as a high-valued customer would need for those EVs. EV customer requirements have a strong impact on environmental, health, and safety concerns. Correspondingly, the rest of the relationship matrix can be completed. Although these values cause decision inconsistency, this can be reduced by establishing many customer-oriented questionnaires and by incorporating a team of engineering, marketing, and research professionals. Finally, there is the outcome at the bottom of the QFD matrix of the relative evaluations (weights). In the present approach, the QFD output correlates the PV module FRs with vehicle requirements. The returned relative evaluations (weights) are the relative importance of all PV module requirements and are the input for the AHP stage. The evaluation was calculated using Equation (3) [21]:

$$Evaluation = \sum \alpha_i \beta_{ij} \quad (3)$$

where, i = number of rows (from 1 to 4); j = number of columns (from 1 to 6); α is the importance; β is score in specific *How*'s.

The evaluation in the first column (power density) was calculated as = 20×9+30×9= 450. The relative evaluation was calculated as the specific evaluation divided by the sum of all evaluations equal to 450/1470 = 0.306 (30.6%). The last step in this approach entails using AHP to rank alternatives. Figure 4 shows the construction of the problem as a top-level hierarchy, as the objective function of the problem. The second level represents the criteria for evaluations, which is the same *How*'s window in the QFD stage. The third hierarchy level has the alternatives, which are the five PV module candidates.

The proposed AHP model evaluates the alternatives different from traditional AHPs [18]. First, the authors created the relationship between the objective function and each criterion in the first hierarchy, giving related weights for each criterion, which is the output of the QFD stage. Second, the pairwise comparison matrix *A* in a traditional AHP in the second hierarchy was obtained based on the decision-maker's judgments, *aij*, from a scale of 1 to 9 using Equation (4) [18]. In the proposed methodology, the decision matrix was based on averaging the values from actual manufacturer datasheets in Table 1. Table 4 shows examples of comparisons of PV alternatives, with respect to power density criteria. The comparison between Mono-Si and Poly-Si yielded a value of 1.117.

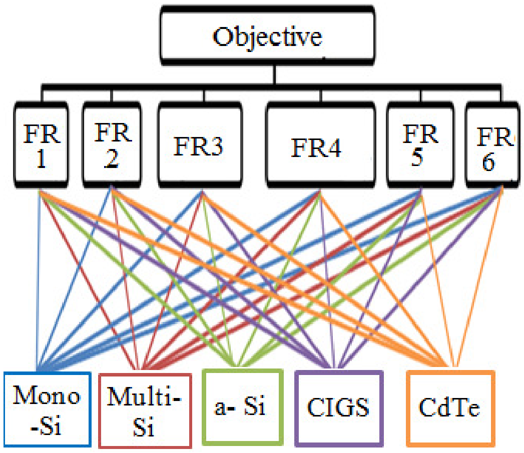

Figure 4. Hierarchical Problem Construction

Table 4. Pairwise Comparison Matrix Related to Power Density

	Mono-Si	Multi-Si	a-Si	CdTe	CIGS
Mono-Si	1.0	**1.117**	2.629	1.43	1.552
Multi-Si	0.89526	1.0	2.353	1.28	1.389
a-Si	0.38037	0.42499	1.0	0.544	0.590
CdTe	0.6993	0.78125	1.8382	1.0	1.085
CIGS	0.64433	0.71994	1.6949	0.92166	1.0

$$A = \begin{bmatrix} 1 & a_{12} & \dots & a_{1n} \\ a_{21} & 1 & \dots & a_{2n} \\ \vdots & \vdots & \dots & \vdots \\ a_{n1} & . & \dots & 1 \end{bmatrix} \tag{4}$$

where, $a_{ij} = 1/a_{ji}$, i, j = 1,…,n

The average power densities from datasheets, listed in Table 1 for Mono-Si and Poly-Si, were equal to 167.5 and 149.9 W/m^2, respectively. By dividing these two numbers, the value of 1.117 was obtained (see Table 4). All comparisons were performed in this manner. Although time consuming, the results were very accurate, as no personal experiences of the designers were used. The consistency index (C.I.) was calculated using Equation (5) [49].

$$CI = \frac{\lambda_{\max} - n}{n - 1} \tag{5}$$

Consistency index (C.I.) = 0.00

where, λ_{max} is the maximal eigenvalue of the comparison matrix and n is the number of the attribute in the square matrix.

In this case, n=5, as shown in Table 4, since the authors used only actual manufacturer datasheets, and the calculated λ_{max} = 5.00, and the C.I. = 0.00, as shown in Table 4. In a typical AHP, the conclusion about C.I can be drawn by comparing it to the consistency ratio (CR) in order to check the judgment inconsistencies using Equation (6) [49]:

$$CR = \frac{CI}{RI} \tag{6}$$

where, RI is the random index, which is an experimental value dependent on n.

In this case, n=5, then RI=1.11 (the full table of RI values can be found in the study by Saaty [49]). In a typical AHP, if the C.I. is less than or equal to 0.111, the decision maker accepts the results; in the proposed methodology, however, the C.I. was zero, which reflects the high accuracy of the methodology used in this study. The final step was to rank all of the alternatives, as shown in Figure 5. The results show that Mono-Si PV modules rank first with a score of 22.9 out of 100 points, followed by multi-Si modules with a score of 21.5 out of 100. The third-, fourth-, and fifth-ranked PV modules were a-Si, CIGS, and CdTe, respectively. The sensitivity analysis of the problem is shown in Figure 6. It clearly indicates that the problem has conflicting objectives. For example, a-Si PV modules have the best results in regards to the PC factor and the worst in both power density and specific weight factors.

The Fuzzy AD Approach

In the second decision-making methodology, the fuzzy AD approach combined with the QFD approach was proposed. The method was based on independence axioms, with information axioms as the decision-selection tool.

Figure 7 lists the steps applied to the fuzzy AD method. The selection of the goal and alternatives were the same as discussed in the AHP decision-making method. Although the FRs were identical to the QFD stage, the first axiom was satisfied. FRs were chosen in order to ensure independence from one another. The system range was set by converting the data in Table 1 to a triangular fuzzy number (TFN) in Table 5. The maximum value was converted to a scale of 10, and the remaining values to a scale of 0-10. The benefits are two-fold: It allows benchmarking the AHP/QFD method, since it uses the same data set; and it provides a robust decision process because it captures the entire commercial

PV market data, and not just the average value used in pairwise comparisons, as with the AHP method. Consequently, decision makers have more freedom to determine which specific PV type satisfies the design range.

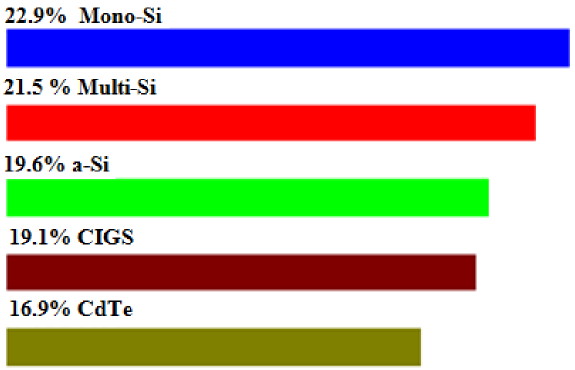

Figure 5. Rank of Different PV Module Types for Vehicle Application using a Combined AHP/QFD Approach

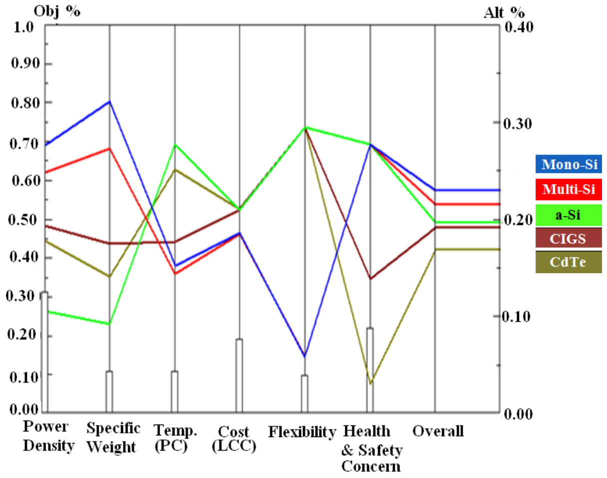

Figure 6. Sensitivity Analysis of AHP/QFD Ranked Results

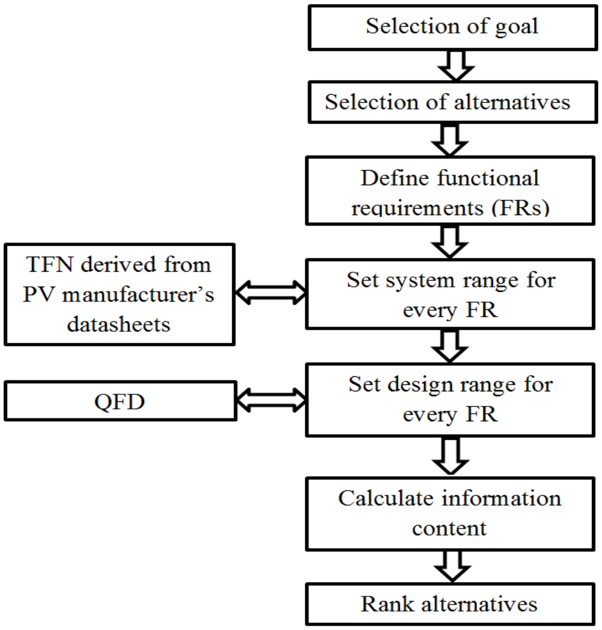

Figure 7. The Proposed Approach for a Fuzzy AD Method

In Table 5, the flexibility is set to "0-1-1" if the module is rigid and set to "1-5-10" if it depends upon packaging. For health and safety concerns, value "0" is the best, indicating few adverse environmental consequences. TFN can be defined by a triplet (n_1, n_2, and n_3), shown in Figure 8. The membership function $\mu(x)$ is defined using Equation (7) [50]. For the design ranges for every FR, a wider selection was provided in order to choose the most appropriate alternative for each FR based on QFD. For the factors of power density, specific weight, and flexibly, the highest values are the best for the proposed application. While for all remaining factors—PC, health and safety concerns, and LCC—the opposite is true.

Table 5. System Range for an AD Approach

Criteria	Power Density			Specific Weight			PC			Cost			Flexibility			Health and Safety Consideration		
PV Types	Min	Max	Avg	Min	Max	Avg	Min	Max	Avg	Min	Max	Avg	Min	Max	Avg	Min	Max	Avg
Multi-Si	6.5	7.6	7.1	5.7	7.7	6.6	9.3	10.0	9.7	5.98	10.0	7.14	0.0	1.0	1.0	0.0	1.0	1.0
Mono-Si	6.9	10.0	7.9	6.0	10.0	7.8	6.6	9.7	9.1	5.93	9.92	7.08	0.0	1.0	1.0	0.0	1.0	1.0
a-Si	2.8	3.2	3.0	1.8	2.6	2.2	5.9	4.4	5.0	5.31	9.44	6.32	0.0	10.0	5.0	0.0	1.0	1.0
CdTe	4.6	5.4	5.1	3.1	3.6	3.4	5.5	5.5	5.5	5.29	9.39	6.29	0.0	10.0	5.0	7.0	10.0	10.0
CIGS	4.0	6.1	5.5	3.7	4.6	4.2	6.9	8.6	7.9	5.29	9.39	6.29	0.0	10.0	5.0	4.0	10.0	10.0

$$\mu(x) = \begin{cases} 0, & x < n_1 \\ \dfrac{x - n_1}{n_2 - n_1} & n_1 \le x \le n_2 \\ \dfrac{x - n_3}{n_2 - n_3} & n_2 \le x \le n_3 \\ 0 & x > n_3 \end{cases} \tag{7}$$

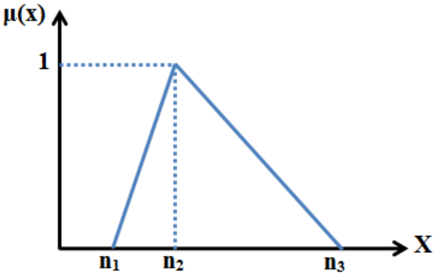

Figure 8. Triangular Fuzzy Number

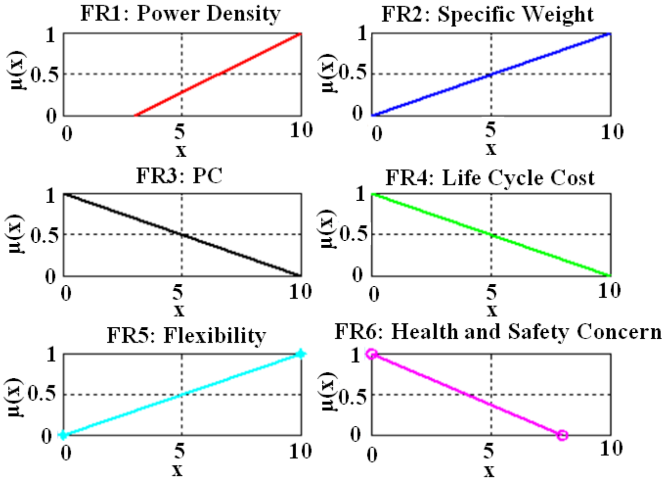

Figure 9. Design Ranges for an AD Approach

The proposed design ranges in this study are shown in Figure 9. The information content, I_i, for the specific FR_i is defined in terms of probability per Shannon's theory [51], in Equation (8):

$$I_i = \log_2 \frac{1}{P_i} \tag{8}$$

where, the information, I, is in unit of bits; P is the probability from the AD perspective; and, P_i is the probability of achieving a specific FR_i.

The information content for the entire system was calculated using the Equation (9) [19], [20]:

$$I_{sys} = \sum_{i=1}^{m} I_i = -\sum_{i=1}^{m} \log_2 P_i \tag{9}$$

where, m is the number of independent FRs.

If the I approach is infinity, the probability is zero and the system will never function. If I is zero, however, the probability is that the system will function perfectly (Axiom 2). In the AD approach, the designer wishes a high probability of success in terms of the design range (tolerance) and system range, which reflects overall system capability. The information content was calculated using Equation (10) [52]:

$$P_i = \frac{\text{Area of common range}}{\text{Area of system design}} \tag{10}$$

Here, the common range was the overlap between the design and system ranges. For example, the information content was calculated for the "FR3: PC" with respect to an a-Si PV module as an alternative (see Figure 10), which indicated the design ranges (see Figure 9) and system ranges (Table 5). By solving the intersection, the following parameters were determined:

$(x_1, \mu_1) = (4.7159, 0.5284)$
$(x_2, \mu_2) = (5.4946, 0.4505)$

$$A_{\text{common}} = 0.5559$$

$$P_i = \frac{0.5559}{\frac{1}{2} \times (5.9 - 4.4) \times 1} = 0.7412$$

$$I_i = \log_2(0.7412) = 0.432$$

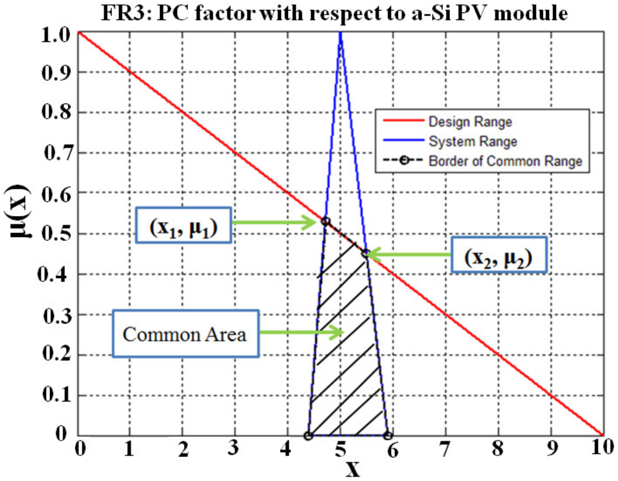

Figure 10. FR3 (PC Factor) with Respect to a-Si PV Module

The same procedure was repeated for each FR and each alternative. The calculations for all FRs with respect to all alternatives are tabulated in Table 6. In total, the Mono-Si PV module was ranked first, as it contained the lowest information content followed by the CIGS and Multi-Si PV modules, respectively. The a-Si and CdTe PV modules were fourth and fifth, respectively. The green color in Table 6 indicates the best PV module option for a specific FR. The green color indicates the lowest information content and the best option for a specific FR.

Discussion and Conclusions

Two decision-making methodologies were proposed here for determining the optimum commercially available PV module type for use in vehicle design: (i) a QFD/AHP combination and (ii) a QFD/Fuzzy AD combination. The novel use of both approaches permitted a mutual benchmarking of each with minimal subjectivity, which was the most difficult challenge. In both approaches, the QFD was incorporated in order to correlate the PV module FRs with vehicle requirements. Both were superior to current methods in that the evaluations were dependent on data collected from PV manufacturer datasheets, reflecting current PV market data, which yielded a very robust methodology. The gathered data were used in a pairwise comparison between various alternatives in the AHP methodology and to derive TFN to implement the system range for the fuzzy AD-based approach to capture the complete commercial PV market. The results from the fuzzy AD approach agreed with the AHP results; for both approaches, the most suitable PV was Mono-Si and the least suitable was CdTe. The difference was that, in the AHP approach, the Multi-Si PV modules were ranked number 2; in the fuzzy AD approach, however, the CIGS was ranked number 2. If the aesthetics are deemed less important, as was assumed here, then the crystalline PV was the most appropriate selection. A comparison of both approaches is provided in Table 7.

Table 6. Information Content for Alternatives

PV Type	Power Density	Specific Weight	PC	LCC of Electricity	Flexibility	Health and Safety Concern	Total
Multi-Si	0.26	0.175	3.89	1.43	4.32	**0.02**	10.1
Mono-Si	**0.12**	**0.08**	1.76	1.4	4.32	**0.02**	**7.7**
a-Si	6.18	1.36	**0.43**	1.11	**2.00**	**0.02**	11.1
CdTe	1.01	0.84	1.15	**1.06**	**2.00**	5.05	11.1
CIGS	0.96	0.60	1.36	1.08	**2.00**	2.39	8.4

Table 7. Comparison between AHP/QFD with Fuzzy AD/QFD

Methodology	AHP/QFD	Fuzzy AD/QFD
Approach	Depends upon pairwise comparison based on average value obtained from many PV manufacturers datasheets	Depends on all range obtained from PV manufacture datasheets. Fuzzy data is from the minimum, average, and maximum values in all datasheets.
Way to minimize subjectivity	Each criterion is compared based on actual manufacturer datasheets and not anecdotal decisions. To improve the pairwise comparison, many datasheets are collected from different manufactures with the average for each criterion calculated for each alternative. The QFD is used to weigh all criteria based on customer need and incorporated into the AHP stage.	The FRs and the design range are derived in the QFD stage. System range is derived from manufacturer datasheets in TFN form.
Strength	The inconsistent error is too low. Accurate data is needed to improve the selection of the best PV module.	Robust decision-making tool works in a fuzzy environment

References

[1] Estimated Energy Use in 2013. (n.d.). Retrieved May 12, 2014, from https://flowcharts.llnl.gov/#

[2] The Outlook For Energy: A View to 2040. (n.d.). Retrieved May 1, 2014, from http://cdn.exxonmobil.com/en/energy/energy-outlook

[3] Greenhouse Gas Emissions from a Typical Passenger Vehicle. (n.d.). Retrieved December 1, 2013, from http://www.epa.gov/otaq/climate/documents/420f14040.pdf

[4] Mints, P. (2013, March 20). Solar PV Profit's Last Stand. Retrieved February 4, 2014, from http://www.renewableenergyworld.com/rea/news/article/2013/03/solar-pv-profits-last-stand?cmpid=SolarNL

[5] Photovoltaics. (n.d.). Retrieved February 8, 2014, from http://energy.gov/eere/sunshot/photovoltaics

[6] Martínez-Duart, J. M., & Hernández-Moro, J. (2013). Commentary: Photovoltaics Firmly Moving to the Terawatt Scale. *Journal of Nanophotonics*, *7*(1), 078599-078599.

[7] Singh, R., Gupta, N., & Poole, K. F. (2008). Global Green Energy Conversion Revolution in 21st Century through Solid State Devices. *Proceedings of the 26th International Conference on Microelectronics,* (pp. 45-54). Niš, Serbia.

[8] Singh, R., Alapatt, G. F., & Lakhtakia, A. (2013). Making Solar Cells a Reality in Every Home: Opportunities and Challenges for Photovoltaic Device Design. *IEEE Journal of the Electron Devices Society*, *1* (6), 129-144.

[9] Singh, R., Alapatt, G. F., & Abdelhamid, M. (2012). Green Energy Conversion & Storage for Solving India's Energy Problem through Innovation in Ultra Large Scale Manufacturing and Advanced Research of Solid State Devices and Systems. *Proceedings of the 2012 International Conference of Emerging Electronics (ICEE),* (pp. 1-8). IIT Bombay, Mumbai.

[10] Singh, R., Asif, A. A., Venayagamoorthy, G. K., Lakhtakia, A., Abdelhamid, M., Alapatt, G. F., et al. (2014). Emerging Role of Photovoltaics for Sustainably Powering Underdeveloped, Emerging, and Developed Economies. *Proceedings of the 2nd International Conference on Green Energy and Technology (ICGET)*. Dhaka, Bangladesh.

[11] Green, M. A., Emery, K., Hishikawa, Y., Warta, W., & Dunlop, E. D. (2014). Solar Cell Efficiency Tables (version 43). *Progress in Photovoltaics: Research and Applications*, *22*(1), 1-9.

[12] Tariq, M., Abdelhamid, M., Li, Y., Omar, M., & Zhou, Y. (2012). Fusion of Thermal and Visible Acquisitions for Evaluating Production-borne Scratches and Shunts in Photo-Voltaic PV Cells. *Journal of Materials Science Research*, *1*(4), 57-72.

[13] Fujinaka, M. (1992). Solar Cars Free of Environmental Pollution-Prototype of Practically Usable Car Completed. *Renewable Energy*, *2*(1), 57-64.

[14] Seal, M. R. (1994). Viking 23-zero Emissions in the City, Range and Performance on the Freeway. *Proceedings of the Northcon/94 Conference Record*, (pp. 264-268). Seattle, WA.

[15] Sasaki, K., Yokota, M., Nagayoshi, H., & Kamisako, K. (1997). Evaluation of Electric Motor and Gasoline Engine Hybrid Car using Solar Cells. *Solar Energy Materials and Solar Cells, 47*(1-4), 259-263.

[16] Astrolab. (n.d.). Retrieved January 10, 2014, from http://www.venturi.fr/vehicules/la-gamme-venturi/astrolab/overview

[17] STELLA. (n.d.). Retrieved September 20, 2014, from http://www.stellagoesusa.com

[18] Saaty, T. L. (1990). How to Make a Decision: the Analytic Hierarchy Process. *European Journal of Operational Research, 48*(1), 9-26.

[19] Suh, N. P. (1990). *The Principles of Design*. Oxford University Press.

[20] Suh, N. P. (2001). *Axiomatic Design: Advances and Applications*. Oxford University Press.

[21] Chan, L. K., & Wu, M. L. (2002). Quality Function Deployment: A Literature Review. *European Journal of Operational Research*, *143*(3), 463-497.

[22] Hwang, C., & Yoon, K. (1981). *Multiple Attribute Decision Making: Methods and Application – A State of the Art Survey*. Springer-Verlags.

[23] Stein, E. W. (2013). A Comprehensive Multi-criteria Model to Rank Electric Energy Production Technologies. *Renewable and Sustainable Energy Reviews, 22*, 640-654.

[24] Ahammed, F., & Azeem, A. (2013). Selection of the Most Appropriate Package of Solar Home System Using Analytic Hierarchy Process Model in Rural Areas of Bangladesh. *Renewable Energy*, *55*, 6-11.

[25] Aragonés-Beltrán, P., Chaparro-González, F., Pastor-Ferrando, J., & Pla-Rubio, A. (2014). An AHP (Analytic Hierarchy Process)/ANP (Analytic Network Process)-based Multicriteria Decision Approach for the Selection of Solar-thermal Power Plant Investment Projects. *Energy, 66*, 222-238.

[26] Scannapieco, D., Naddeo, V., & Belgiorno, V. (2014). Sustainable Power Plants: a Support Tool for the Analysis of Alternatives. *Land Use Policy*, *36*, 478-484.

[27] Abdelhamid, M., Singh, R., Omar, M. (2014). Review of Microcrack Detection Techniques for Silicon Solar Cells. *IEEE Journal of Photovoltaics, 4*(1), 514

-524.

[28] Kahraman, C., Cebi, S., & Kaya, İ. (2010). Selection among Renewable Energy Alternatives Using Fuzzy Axiomatic Design: The Case of Turkey. *Journal of Universal Computer Science*, *16*(1), 82-102.

[29] Boran, F. E., Boran, K., & Dizdar, E. (2012). A Fuzzy Multi Criteria Decision Making to Evaluate Energy Policy Based on an Information Axiom: A Case Study in Turkey. *Energy Sources, Part B: Economics, Planning, and Policy*, *7*(3), 230-240.

[30] Maldonado, A., García, J. L., Alvarado, A., & Balderrama, C. O. (2013). A Hierarchical Fuzzy Axiomatic Design Methodology for Ergonomic Compatibility Evaluation of Advanced Manufacturing Technology. *The International Journal of Advanced Manufacturing Technology*, *66*(1-4), 171-186.

[31] Kannan, D., Govindan, K., & Rajendran, S. (2014). Fuzzy Axiomatic Design Approach Based Green Supplier Selection: a Case Study from Singapore. *Journal of Cleaner Production.* doi:10.1016/j.jclepro.2013.12.076

[32] Carnevalli, J. A., & Miguel, P. C. (2008). Review, Analysis and Classification of the Literature on QFD—Types of Research, Difficulties and Benefits. *International Journal of Production Economics*, *114*(2), 737-754.

[33] Ho, W. (2008). Integrated Analytic Hierarchy Process and its Applications–a Literature Review. *European Journal of Operational Research, 186*(1), 211-228.

[34] Mayyas, A., Shen, Q., Mayyas, A., Abdelhamid, M., Shan, D., Qattawi, A., et al. (2011). Using Quality Function Deployment and Analytical Hierarchy Process for Material Selection of Body-in-White. *Materials & Design*, *32*(5), 2771-2782.

[35] Qattawi, A., Mayyas, A., Abdelhamid, M., & Omar, M. A. (2013). Incorporating Quality Function Deployment and Analytical Hierarchy Process in a Knowledge-based System for Automotive Production Line Design. *International Journal of Computer Integrated Manufacturing*, *26*(9), 839-856.

[36] Kahraman, C., Kaya, İ., & Cebi, S. (2009). A Comparative Analysis for Multiattribute Selection among Renewable Energy Alternatives using Fuzzy Axiomatic Design and Fuzzy Analytic Hierarchy Process. *Energy*, *34*(10), 1603-1616.

[37] Bouyssou, D., Marchant, T., Pirlot, M., Perny, P., Tsoukias, A., & Vincke, P. (2000). *Evaluation and Decision Models: A Critical Perspective*. Kluwer Academic Publishers.

[38] Mehta, S. (2014). Global 2013 PV Module Production Hits 39.8GW; Yingli is the Shipment Leader. Retrieved April 23 from http://www.greentechmedia.com/articles/read/Global-2013-PV-Module-Production-Hits-39.8-GW-Yingli-Leads-in-Production-a

[39] Singh, R., & Leslie, J. D. (1980). Economic Requirements for New Materials for Solar Photovoltaic Cells. *Solar Energy*, *24*, 589-592.

[40] Singh, R. (2009). Why Silicon Is and Will Remain the Dominant Photovoltaic Material. *Journal of Nanophotonics, 3(1)*, 032503.

[41] Peters, C. H., Sachs-Quintana, I. T., Kastrop, J. P., Beaupré, S., Leclerc, M., & McGehee, M. D. (2011). High Efficiency Polymer Solar Cells with Long Operating Lifetimes. *Advanced Energy Materials*, *1*(4), 491-494.

[42] Saurat, M., & Ritthoff, M. (2010). *Photovoltaics and the RoHS Directive*, Wuppertal Institute, Retrieved from https://engineering.dartmouth.edu/~d30345d/courses/engs171/SauratRittoff-Photovoltaics_and_RoHS-2010.pdf

[43] Ito, M., Kato, K., Komoto, K., Kichimi, T., & Kurokawa, K. (2008). A Comparative Study on Cost and Life-cycle Analysis for 100 MW Very Large-scale PV (VLS-PV) Systems in Deserts Using m-Si, a-Si, CdTe, and CIS Modules. *Progress in Photovoltaics: Research and Applications*, *16*(1), 17-30.

[44] Lakhani, R., Doluweera, G., & Bergerson, J. (2014). Internalizing Land Use Impacts for Life Cycle Cost Analysis of Energy Systems: A Case of California's Photovoltaic Implementation. *Applied Energy*, *116*, 253-259.

[45] Aly, A. M., & Bitsuamlak, G. (2013). Aerodynamics of Ground-mounted Solar Panels: Test Model Scale Effects. *Journal of Wind Engineering and Industrial Aerodynamics*, *123*(Part A), 250-260.

[46] Aly, A. M., & Bitsuamlak, G. (2013). Wind-induced Pressures on Solar Panels Mounted on Residential Homes. *Journal of Architectural Engineering*, *20*(1). 04013003-1, 04013003-12.

[47] PVinsights Grid the World. (n.d.). Retrieved May 5, 2014, from http://pvinsights.com/index.php

[48] Fthenakis, V., Frischknecht, R., Raugei, M., Kim, H. C., Alsema, E., Held, M., et al. (2011). *Methodology Guidelines on Life Cycle Assessment of Photovoltaic Electricity*. (2nd edition). (EA-PVPS T12-03:2011). International Energy Agency Photovoltaic Power Systems Programme.

[49] Saaty, T. L. (1994). *Fundamentals of Decision Making and Priority Theory with the Analytic Hierarchy Process*. RWS Publications

[50] Kaufmann, A., & Gupta, M. M. (1991). *Introduction*

to Fuzzy Arithmetic: Theory and Applications. Van Nostrand Reinhold.

[51] Shannon, C. E. (1948). A Mathematics Theory of Communication. *The Bell System Technical Journal*, *27*(3-4), 373-423.

[52] Kulak O., & Kahraman C. (2005). Multi-attribute Comparison of Advanced Manufacturing Systems using Fuzzy vs. Crisp Axiomatic Design Approach. *International Journal of Production Economics, 95* (3), 415–424.

Biographies

MAHMOUD ABDELHAMID is a Post-Doctoral Scholar at the University of California Advanced Solar Technologies Institute (U.C. Solar) based at the University of California, Merced. He earned his Ph.D. degree from Clemson University (Automotive Engineering, 2014), his M.S. degree from Clemson University (Mechanical Engineering, 2011), and his B.S. degree from Hashemite University, Jordan (Electrical and Computer Engineering, 2004). His research has been published as a one-book manuscript, as well as in more than sixteen journal publications and conference proceedings. His research interests are in the area of sustainable transportation, solar energy, lifecycle assessment, and knowledge-based sustainable manufacturing. Dr. Abdelhamid may be reached at mabdelhamid@ucmerced.edu

ALA QATTAWI is an Assistant Professor at the University of California, Merced. She earned her B.S. degree from Jordan University of Science and Technology, Jordan (Industrial engineering, 2007) and her Ph.D. degree from Clemson University (Automotive Engineering, 2012); she became the first female to earn that degree in the U.S. Her research interest is in innovative manufacturing processes and design, with a focus on Origami-based design and knowledge-based manufacturing. Dr. Qattawi may be reached at aqattawi@ucmerced.edu

RAJENDRA SINGH is the D. Houser Banks Professor in the Department of ECE and the Director of the Center for Silicon Nanoelectronics at Clemson University. He earned his Ph.D. degree from McMaster University, Hamilton, Ontario, Canada (Physics, 1979). His research interests are in the area of semiconductor and photovoltaic device materials and applications. He has published over 350 papers in various journals and conference proceedings. Dr. Singh received various awards, including the White House's "Solar Champions of Change" (April, 2014). Dr. Singh may be reached at srajend@clemson.edu

IMTIAZ HAQUE is Director of the U.S. DOE GATE Center of Excellence in Sustainable Vehicle Systems, Executive Director of the Carroll A. Campbell Graduate Engineering Center, and Founding Chair of the Department of Automotive Engineering at Clemson University. He earned both M.S. and Ph.D. degrees from Clemson University (Mechanical Engineering, 1977 and 1982, respectively). His research interests are in the design, modeling, and simulation of mechanical systems including vehicles and transmissions. Professor Haque has published over 100 refereed papers and has served as PI or co-PI on grants totaling over $100M. Dr. Haque may be reached at sih@clemson.edu

EVALUATION OF THE SILICON-ON-GLASS MICROFABRICATION PROCESS FOR MEMS ACCELEROMETERS

Thomas S. White, Central Michigan University; Kevin Petsch, Michigan State University; Tolga Kaya, Central Michigan University

Abstract

In this paper, the authors present a testing procedure and the results of a capacitive triaxial accelerometer intended for health and safety applications. In this study, static and quasi-static tests were performed in order to gain insight into the overall functionality of devices and the effectiveness of the Silicon on Glass (SOG) microfabrication process performed at the Lurie Nanofabrication Facility (LNF) at the University of Michigan, Ann Arbor. SOG was incorporated into the design in order to reduce parasitic capacitances because they can impede accuracy and sensitivity. Understanding how this form of wafer bonding impacts the design was crucial to understanding the capabilities of the accelerometers. Capacitance reading yields showed ranges within predicted limits and deviations caused by the fabrication process. The highest change in capacitance was obtained to be 94.1% during quasi-static tests, while the lowest change was 7.6%. Out of 1259 devices tested on a 4'' wafer, 34 of them passed, yielding a success rate of 2.7%. This simplified method of elimination consumed less time for the accelerometer tests and made the optimization process viable.

Introduction

The field of MEMS (Microelectromechanical Systems) technology research has been continuously expanded. Applications can be found in numerous technologies such as smart phones, laptop computers, inkjet printers, microphones, and micro-scale lasers [1-7]. Factors that make MEMS devices so attractive include their relative reliability, low cost, and ability to be mass-fabricated [8]. In particular, MEMS-based accelerometers appear to have many possible applications [9-16]. In civil engineering, capacitive accelerometers have shown promise for gauging strain placed upon bridges through integration into sensing and transmission systems [15]. Companies such as BP and Shell have found that capacitive accelerometers offer benefits of lower-power consumption, reduced signal noise, and wider device dispersion for exploring oil and gas deposits [9]. Medical institutions explore possible applications for these sensors in areas such as monitoring heart bypass patients and collecting data relating to gait and balance in the elderly [16], [17]. For individuals at a higher risk of falling, like the elderly and disabled, low-G (up to 4 G) motion sensors have the potential to increase personal safety through monitoring physical activity [16], [17]. Emergency response personal can be notified immediately when the motion sensors register a falling event and signal to quickly bring assistance.

Capacitive accelerometers measure capacitance changes between a mobile electrode (the proof-mass in this case) and the bottom electrode, as shown in Figures 1(a) and 1(b) [6], [10], [17]. Capacitive accelerometers often depend on actuators such as cantilever beams, spring structures, or folded flexures to support a central proof-mass and allow it move as depicted in Figure 1(a) [6], [10], [17]; the red areas are immobile and the grey are mobile. Capacitance values can be calculated using Equation (1):

$$C = \frac{\epsilon A}{d} \tag{1}$$

where, C represents the capacitance, A represents the area of the capacitance plates, ϵ denotes the permittivity of the dielectric material between the plates, and d symbolizes the distance between the capacitance plates. A change in capacitance corresponds to changes in displacement of the proof-mass [17-20]. The distance between the plates and the resulting capacitance values have an inverse relationship. Another accelerometer design incorporates a comb-drive consisting of interdigitated electrodes that form parallel-capacitance plates, as shown in Figure 1(c) [6], [11], [17]. The type of accelerometer incorporated into a sensing system is determined by the needs of system designers. The capacitive signals generated by such sensors are relayed through a digital converter and sent to a computer or a recording device so that data can be analyzed [21].

The accelerometer design discussed here is intended for health and safety monitoring. It incorporates both comb-drives and a mobile proof-mass/bottom electrode mechanism in the same device, as depicted in Figure 2(a). The comb-drive measures capacitance along the x and y planes, as illustrated in Figure 2(b) [11], [17]. Tilt and z-directional readings are accommodated by the proof-mass and bottom electrode. The flexible spring structures shown in Figure 2 (c) actuate the proof-mass and allow not only a 3-dimensional range of motion, but also high sensitivity [11]. This type of motion sensor could eventually integrate piezoelectric materials that could help make them energy efficient as well as more accurate [22], [23].

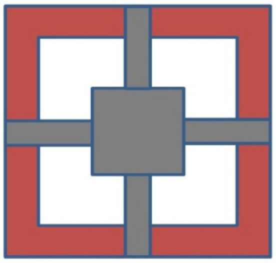

(a) Cantilever/Proof-mass Top

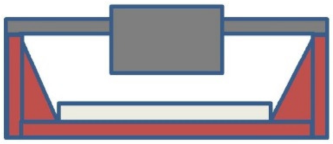

(b) Cantilever/Proof-mass Cutaway

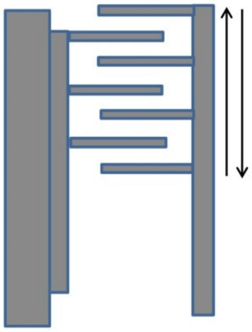

(c) Comb Drive

Figure 1. Examples of Accelerometers

The sensitivity of the device depends strongly on the proper fabrication and material selection procedures. It was decided that silicon and glass wafers together would perform best in this case. Silicon on Glass (SOG) anodic bonding was used to bond silicon and glass wafers together by applying an electric potential across both wafers [24], [25]. A major benefit of SOG is that the glass' non-conductive nature helps reduce parasitic capacitances which could reduce the accuracy and overall effectiveness of the sensors [17].

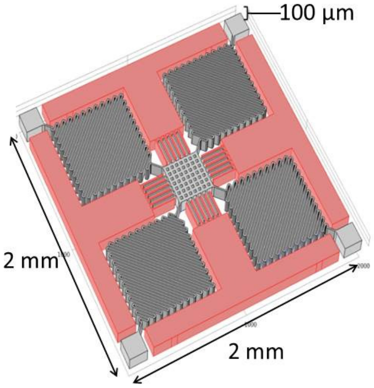

(a) Entire Accelerometer

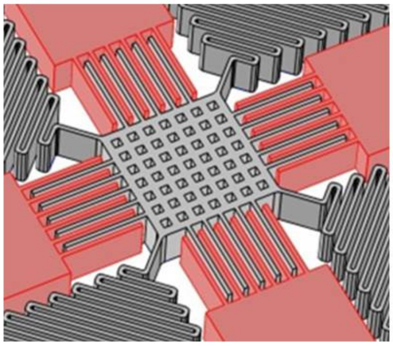

(b) Closeup of Proof-mass and Comb Drives

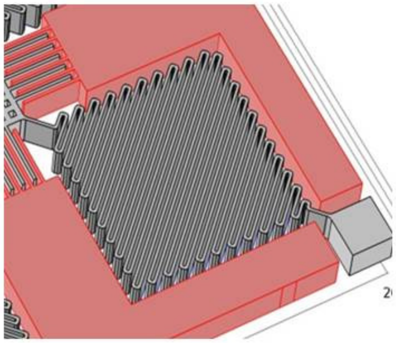

(c) Closeup of Serpentine Spring Actuator

Figure 2. A Comb Drive Triaxial Accelerometer

Testing can be static, quasi-static, and dynamic in nature. Static tests require no movement of any mobile structures. An example of a static test conducted in this current study involved checking the resistance along a stationary electrode to verify its function. Quasi-static examinations allowed the electrical and mechanical performance of a device to be checked in a single direction at a time. For example, in this study, the proof-mass was moved to the left (the negative x-direction, in this case) in order to measure the change in capacitance. Static and quasi-static evaluations were initially performed because they gave a direct and fast result of a device's functionality. Devices that passed these tests were good candidates for later dynamic testing. Dynamic tests allow the full range of an accelerometer's motion and sensitivity to be observed by a method like a shaker or Electron Speckle Pattern Interferometry [26-28], which are means of evaluating a sensor's performance in an environment that more closely simulates real-life conditions. But, before this can happen, the design and fabrication processes need to be evaluated and the reliability of the SOG process understand. Therefore, different designs were tested and the yields observed. Yield analysis and percent evaluations, based upon the gathered data, offered a clear picture of how the devices actually performed in terms of consistency and reliability.

Design and Fabrication

The development of the particular designs discussed here incorporated computer drafting and finite element analysis simulations via COMSOL Multiphysics®. Fabrication occurred at the University of Michigan's Lurie Nanofabrication Facility [17]. Fabrication of the devices included standard MEMS techniques such as photolithography, metal deposition, hydrofluoric acid etching of the glass substrate, anodic bonding of the glass and silicon wafers, and dry etching for shaping and releasing each of the devices' mobile structures [17]. The finished product of fabrication was a wafer containing nearly 1200 devices. The devices were organized into 5x5 geometric groups called dies. A die consisted of 25 devices of differing dimensions and directions of functionality, and is illustrated in Figure 3.

Figure 3(a) shows the fabricated wafer. A full die of 25 different designs which were fabricated and tested can be seen in Figure 3(b). Table 1 lists devices organized by type, sensitivity, and the spring actuator they employ. Accelerometers A-R function three-dimensionally. Devices U-W were designed for sensing motion along the x and z planes. Designs S, T, X, and Y served to take readings in the z direction only. The wafer contained approximately 45 complete dies.

Figure 4 was intended to serve as a guide, while different aspects of the testing process are explained. Specific regions of devices—static and mobile—are indicated by colored highlights. Only the proof-mass is mobile and traced with red. The static bottom electrode and anchor-fins are static and can be seen marked by the blue and green indicators, respectively. The following descriptions for both short and capacitance testing refer to Figure 4.

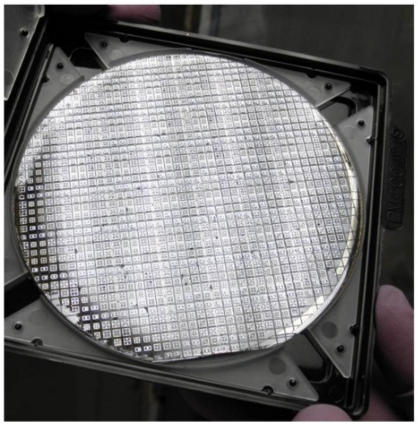

(a) Full Wafer of Accelerometers

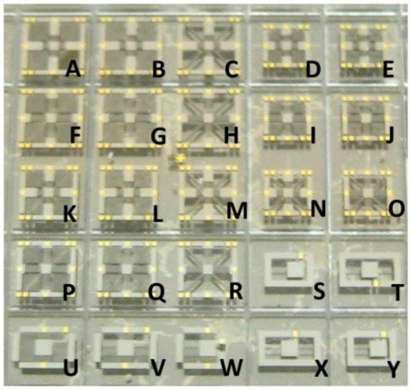

(b) A Die of 25 Accelerometers

Figure 3. Wafer and Closeup of Finished Accelerometers

Table. 1 Devices by Range and Spring Structure

Design Type	Sensing Range	Spring Type
A, D, F, I, K, P	3-D	Serpentine
B, E, G, J, L, Q	3-D	Spiral
C, H, M, N, O, R	3-D	Semi-serpentine
S, T, X, Y	1-D	Straight
U, V,W	2-D	Serpentine

The effectiveness of a device was examined through testing. Through proper evaluations, desired characteristics such as correct release of mobile structures, functional ability to take readings, and accuracy of those readings can be verified [1], [3], [6], [17]. Devices that passed all phases of testing were considered to be successful in terms of yield.

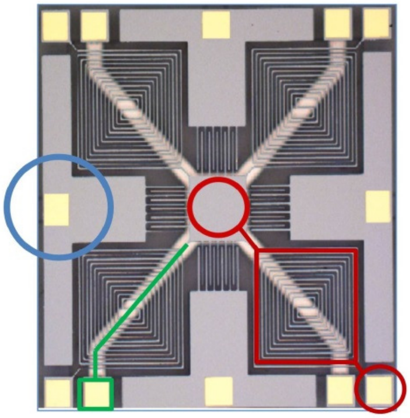

Figure 4. Various Regions Tested for Resistance

Testing Procedures

Testing was carried out in a soft-walled cleanroom via the Cascade Microtect M-150 probe station, as shown in Figure 5(a). The setup included a Dell® desktop computer, Keithley 179-A TRMS digital multimeter—Figure 5(b)—and a GLK Instruments 3000 capacitance meter—Figure 5 (c). GrabBee® video software was used for image capturing. The readings taken from the capacitance and digital multimeters were stored on Microsoft Excel© data sheets that corresponded to each stage of testing. Each meter was connected to the probe station (two probes for each meter) for performing electrical and mechanical testing of the devices. The data were then stored in a file on the Dropbox© website to facilitate communication between members of the research team.

Testing was done in a particular order. The basic reasoning was that if a device demonstrated a failure mode at a particular point of testing, then the tester could record the results and move on to another device. By process of elimination, successful devices could be eventually found in an efficient manner. Any negative capacitance reading, or reading higher than the theoretical value, indicated a device failure. Before static and quasi-static tests were performed, several quick inspections were done to determine if devices warranted the time required for full testing. First, a basic visual examination for any obvious damage, debris contaminants, or structural defects was performed. If the device appeared to be free of structural defects and debris contamination, the static capacitance between the proof-mass and the bottom electrode was briefly observed. The last test employed the probe tips to observe how well the proof-mass moved and returned to its original position. Any stiction indicated a failure. Devices that passed were allowed to proceed to regular evaluations.

(a) The Accelerometer Testing Station

(b) The Digital Multimeter

(c) The Capacitance Meter

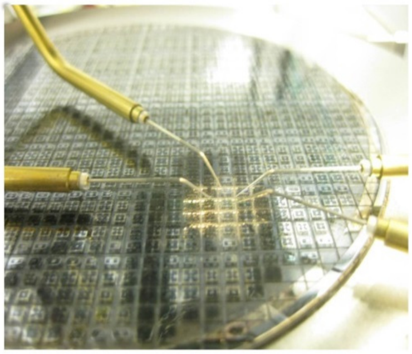

(d) Probe Tips Placed on a Wafer during a Short Test

Figure 5. The Testing Equipment and Wafer Example

Short Tests

Short testing was the first step in this process because it verified the release of mobile structures in the device. "Released" referred to the proper etching of particular structures so that they could move as intended. It also meant that testing revealed no shorts between regions that were not supposed to be in contact. It should be noted that shorts can also be caused by debris such as dust contaminating a device [9]. Resistance evaluations employed a digital multimeter to check for shorting between various device regions.

When performing short tests, the only regions that should give any readings for resistance are the top electrode and the bottom electrode (see Figure 4). Both portions of the device were designed to have four contact points each. Additionally, the top and bottom electrodes act as individual closed circuits. By evaluating the resistances between their respective contact pads, the functionality of each region was determined. All other regions had to show open circuits, because they were expected to be separate from one another, otherwise the device failed testing. The expected readings for the proof-mass and the bottom electrode averaged 5 kΩ and 1 kΩ, respectively.

The first two regions inspected were the proof-mass and bottom electrode. The probe tips were placed at the four contact pads for each region denoted in Figure 4. The goal was to verify that at least three distinct paths were functional along each portion. To check this, one probe tip remained stationary at a contact pad while the other was moved between two other corresponding pads. This provided two readings that were averaged and documented. If both parts passed, then the remaining regions of the device would be examined. Resistance tests were then performed between the proof-mass and each anchor-fin section; between the bottom electrode and anchor-fins; between the anchor-fin regions themselves; and, finally, the proof-mass and bottom electrode. Successful devices could then move on to capacitance inspections.

The resistance readings gathered from the proof-mass and bottom electrodes are shown in Figure 6.the values for R_{max}, R_{min}, and R_{avg} were very close for both regions. R_{max} represented the highest resistance; R_{min} represented the lowest value; and, R_{avg} was the average reading. Figure 6(a) demonstrates that the proof-mass had a high number of readings between 3.5 kΩ and 4.5 kΩ—fairly close to its expected value. It also showed a trend of fewer occurrences of multiple readings within a similar range occurring as they increased in magnitude. Figure 6(b) shows the variations of the data gathered from the bottom electrode. The data suggest that the occurrence of multiple resistances within a similar range was slightly more consistent here. It was noted that all of the resistances for the bottom electrode measured higher than its expected value of 1 kΩ. In both cases, the data showed that the resistances for both regions were out of their projected ranges, due to fabrication process variations.

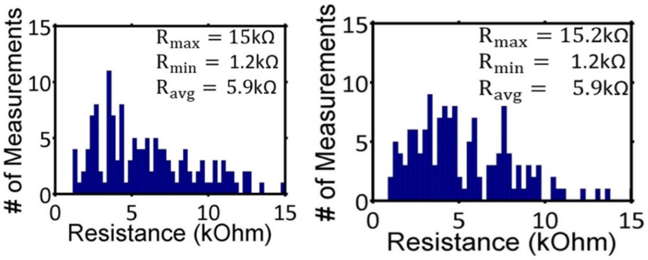

(a) Proof-mass Resistance **(b) Bottom Electrode Resistance**

Figure 6. Resistance Readings for the Proof-mass and Bottom Electrode Regions

Static testing

Static capacitance testing followed a similar flow as the resistance tests. Capacitances between the same regions were evaluated. Anything out of the acceptable range was considered a failure mode. Capacitance checks followed this order: proof-mass to anchor-fins; proof-mass to bottom electrode; and then the anchor-fin regions directly across from one another. Same as for the short tests, the readings were averaged and recorded. Figure 7 demonstrates the sequence of this phase of the evaluations.

Results varied between the different regions in which testing took place. C_{max}, C_{min}, and C_{avg} represented the highest, lowest, and average capacitance readings, respectively, for each graph in Figure 7. Figure 7(a) demonstrates the varied data gathered while testing the devices along the x- and y- planes. The most consistent grouping of capacitances remained close to 0.23 pF. It can also be seen that readings in Figure 7(a) were dispersed in a relatively even fashion--starting with the minimum value of 0.17 pF. The static performance between the top and bottom electrodes can be seen in Figure 7(b). It was the largest range between 0 pF and 7 pF. The lowest reading was 0.06 pF and the highest was 6.7 pF. Of all the locations on the device, readings here tended to rank the highest in range and frequency of approximate occurrence. This was due to the relatively large surface areas between the bottom electrode and proof-mass, while they functioned as capacitance plates.

The most consistently recurring readings were approximately 1 pF. The most similar sets of readings were between the anchor-fins themselves. Figures 7(c) and 7(d) show the readings for the horizontal and vertical readings, respectively. The peaks on both graphs illustrate similar behavior in both regions. This was no surprise as all four regions were of the same basic design, yet there was a small difference worth mentioning. Figure 7(d) has a higher average than Figure 7(c), yet during actual testing it was observed that the average capacitance was generally 0.01 pF higher for the static capacitance plates across from one another horizontally, than for those vertically across from one another.

Quasi-static Testing

A delicate touch was needed during quasi-static tests. At the micro-scale, structures in MEMS devices can be easily damaged with a careless movement. With a little practice, though, this method can be mastered without much difficulty. Figure 8 offers an illustration of anchor fins correctly being manipulated. It should be pointed out that the fins are brought together as closely as possible to make note of a reading, but not so close as to short them or damage the fins. Four probe tips—two stationary for measuring changes in capacitance and two to move the proof-mass—were required for this series of tests. Measurements were taken for the x and y directions—two sets of readings for each anchor -fin region (left, right, up, and down). The z-direction only provided one reading (up-down). Any readings out of range or any stiction indicated a device had failed testing.

The changes in capacitance can be seen in Figure 9. These charts show the percentage of capacitance change for each area of testing. Data for all three directions were plotted in order to show the percentages of capacitance change in relation to the approximate number of times they came up. Also included with ΔC_{max}, ΔC_{min}, and ΔC_{avg} were the largest variations that occurred during z-directional examinations. The quasi-static performance for the x- and y-directional examinations revealed similar performances but, overall, the performance for the y-plane seemed to be higher than the readings of the x axis—an average variation of 3.2% difference in performance.

The performance in the x-plane revealed a slightly more consistent tendency towards repeated instances of higher percentages than the y plane. The overall device performance in the z direction showed the most variation. This demonstrated high degrees of consistency in terms of percentage of change in capacitance ranging between recurrences of 3 to 5 times for readings between approximately 25% and 60%; this could be related to the various types of devices that were designed for the z-plane function.

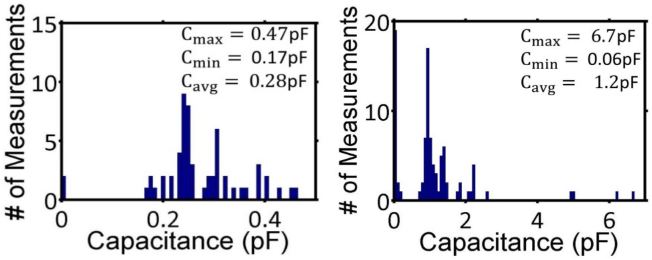

(a) Proof-mass to Anchor-fins Readings

(b) Proof-mass to Bottom Electrode Readings

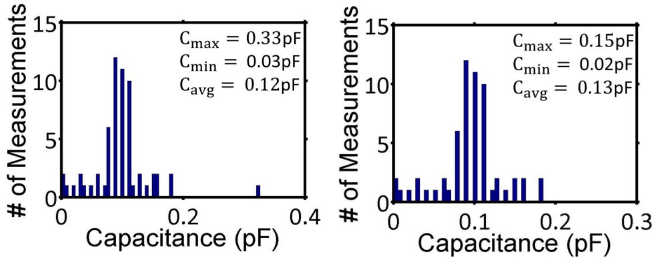

(c) Horizontal Anchor-fin Capacitances

(d) Vertical Anchor-fin Capacitances

Figure 7. Capacitance Readings for Various Device Regions

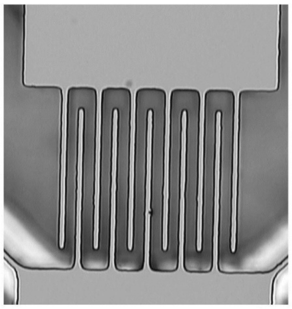

(a) Stationary Position

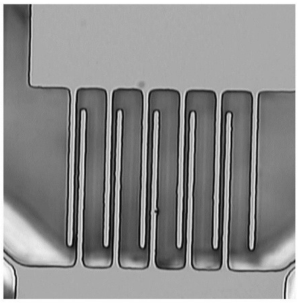

(b) After X-Directional Movement

Figure 8. Optical Microscopy Snapshots during the Quasi-static Capacitance Measurements

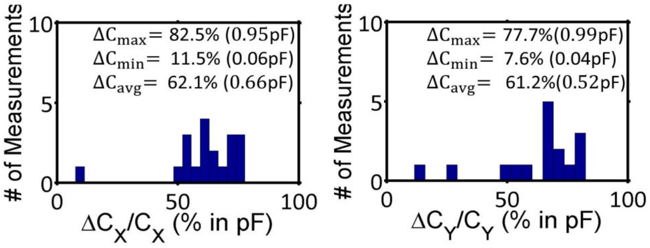

(a) X-Direction **(b) Y-Direction**

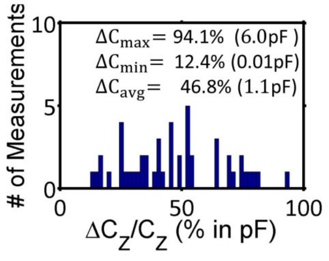

(c) Z-Direction

Figure 9. Capacitance Changes in Three Directions

Device Failures and Yield Analysis

The most common causes for device failure were related to stiction or incomplete etching. Figure 10 provides visual examples of some of these sources of malfunction. Both factors seemed to cause devices to fail the short, capacitance, or mobility tests. Examples of these types of structural failures included anchor-fins being fused together by or to the substrate, as shown in Figures 10(e) and 10(f). In some instances, the proof-mass was rendered completely immobile, due to this type of fusion, as indicated in Figure 10(e). A common stiction-related problem occurred when either the proof-mass wouldn't return to its original position or a higher capacitance reading would be shown after being flexed and returned to its static position. In some instances, capacitance would actually decrease when capacitance plates were brought together. Most commonly, this seemed to happen in z-directional devices.

Table 2 illustrates the percentages of accelerometers that passed each stage of testing with respect to the initial lot of devices. The top row represents the number of devices at each point in the evaluation. The bottom row contains the corresponding percentage of passing devices. The ratio of acceptable accelerometers from the visual examination to the final quasi-static stage was 65%/2.7%, or 24/1. The 2.7% refers to the 34 remaining devices out of the total 1259. Yield percentages for successful devices, as identified in Table 1, were as follows: 65.6% of the remaining sensors were of the straight, one-dimensional type; 13% of the actuator accelerometers were of the semi-serpentine type; 12.6% were of the serpentine variety; the remaining 8.8% of successful devices were of a spiral actuator design. None of the two-dimensional, spiral sensors passed testing. During the process of analyzing the various design types, it appeared as though the more complex actuator designs were more prone to stiction (due to van der Waals forces) and incomplete etching. The one-dimensional and semi-serpentine actuator models were the simplest designs, yet faired the best overall.

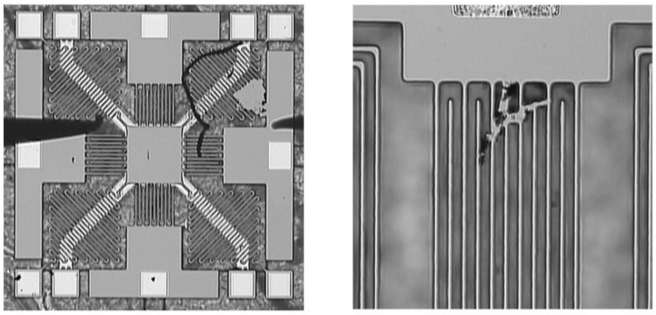

(a) Structural Damage/ Debris Contamination **(b) Incomplete Etching Causing a Short**

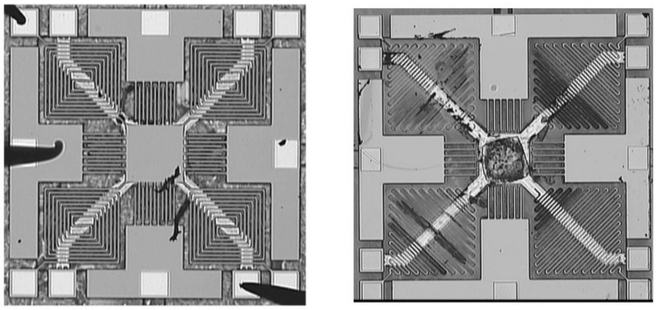

(c) Adhesion and Debris **(d) Destruction during Fabrication**

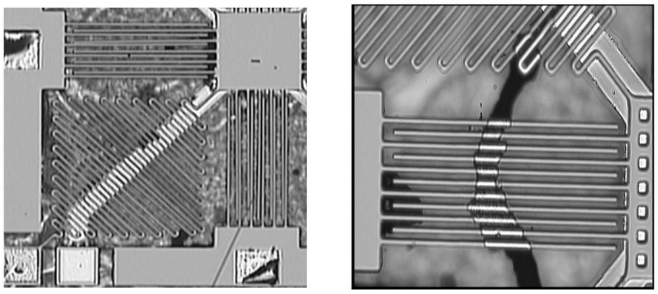

(e) Stiction **(f) Adhesions from Incomplete Removal of Photoresist**

Figure 10. Examples of Various Device Failures

Table 2. Devices and Percent Yields from Tests

	Fabricated	Visual Exam	Short Tests	Static Tests	Quasi-Static Tests
# Devices	1259	819	129	98	34
Yield (%)	N/A	65	10.2	7.8	2.7

Conclusion

A simple and low-cost testing process for evaluating capacitive accelerometers was described in this paper. The results helped to identify the most reliable designs for future fabrication and testing. This is particularly important when considering the time and costs related to subsequent wire-bonding and dynamic tests. In future fabrications, reliable models could even integrate a piezoelectric material to serve as both a built-in power supply and an on/off switch that responds to changes in motion. Combined with the comb-drive, the resulting device could offer the benefits of being very simple in function, highly sensitive, compact in size, and power efficient. This would be ideal for health and safety monitoring.

The differences in capacitance readings between the anchor-fin regions along the x and y planes revealed very small differences in capacitance readings, yet were still relatively consistent in overall performance. The x-directional capacitances offered a larger number of consistently recurring readings in several different percentages, while the y-directional performance yielded the highest percentage for a single reading range—approximately 60%. The readings for the z-plane were the most varied, due to the different designs tested that ranged from 1-D to 3-D areas of sensitivity; a larger surface area between the top and bottom electrodes were another likely reason for the higher degree of variation in readings between these regions. The 3-D devices that passed testing showed relatively reliable performance during these tests. Of these, the semi-serpentine actuators appeared to perform the best during the most recent phase of testing. With a reassessment of the fabrication and testing procedures, the yield should be significantly higher in future evaluations. The z-directional devices showed the highest degree of success in testing, in part due to their simpler function and less testing needed for them. Despite the yield results, the basic testing procedure itself is reliable and cost-effective for evaluating capacitive accelerometers up to the quasi-static level.

Acknowledgements

The authors would like to thank the Lurie Nanofabrication Facility staff at the University of Michigan, Ann Arbor. This research was supported by an Early Career Investigator grant (Grant # C61659) from Central Michigan University.

References

[1] Aswendt, P., Schmidt, C.-D., Zielke, D., & Schubert, S. (2002). HNDT Solution for MEMS Testing on Wafer Level. *ZDT.net, 4*(7). Retrieved from http://www.ndt.net/ article/v07n04/aswendt/aswendt.htm

[2] Bouchaud, J. (2011). Tablets and Smartphones Spur Record MEMS Revenue Growth in 2011. IHS iSuppli. Retrieved from http://www.isuppli.com/MEMS-and-Sensors/News/Pages/Tablets-and-Smartphones-Spur-Record-MEMS-Revenue-Growth-in-2011.aspx

[3] Chae, J., Kulah, H., & Najafi, K. (2005). A Monolithic Three-Axis Micro-g Micromachined Silicon Capacitive Accelerometer. *Journal of Microelectronics*, *2*(14), 235-242. doi: 10.1109/JMEMS.2004.839347

[4] Culhane, K. M., O'Connor, M., Lyons, D., & Lyons, G. M. (2005). Accelerometers in Rehabilitation Medicine for Older Adults. *Age and Ageing, 34*(6), 556-560.

[5] Demerjian, C. (2011). Memjet Speeds Up Printing with MEMS. Retrieved from http://semiaccurate.com/2011/02/25/memjet-speeds-up-printing-with-mems

[6] Farahani, H., Mills, J., & Cleghorn, W. (2009). Design, Fabrication and Analysis of Micromachined High Sensitivity and 0% Cross-Axis Sensitivity Capacitive Accelerometers. *Microsystem Technology*, *15*(12), 1815-1826.

[7] Fedder, G. K. (2003). MEMS Fabrication. *Proceedings of the 2003 International Test Conference,* (pp 691-698). Charlotte, NC.

[8] McNulty, J. (2008). A Perspective on the Reliability of MEMS-Based Components for Telecommunications. *SPIE Proceedings, Paper #6884.*

[9] HP. (2011). HP Seismic Sensor for Oil and Gas Exploration. Retrieved from http://www.hp.com/hpinfo/newsroom/press_kits/2011/sensingsolutions/HP_Seismic_Sensor_wp.pdf

[10] Whelan, M. J., Fuchs, M. P., Gangone, M. V., & Janoyan, K. D. (2007). Development of a Wireless Bridge Monitoring System for Condition Assessment Using Hybrid Techniques. *SPIE Proceedings.* Paper #6530. doi: 10.1117/12.715905

[11] Kaya, T., & Koser, H. (2005). A Study of Nonlinear

Deflection Dynamics of a Peizoelectric Accelerometer. *COMSOL Multiphysics User's Conference*. Boston, MA.

[12] Kaya, T., Shiari, B., Petsch, K., & Yates, D. (2011). Design of a MEMS Capacitive Comb-Drive Accelerometer. *COMSOL Multiphysics User's Conference*. Boston, MA.

[13] O'Sullivan, M., Blake, C., Cunningham, C., Boyle, G., & Finucane, C. (2009). Correlation of Accelerometry with Clinical Balance Tests in Older Fallers and Non-Fallers. *Age and Ageing*, *38*(3), 308-313.

[14] Man, K. F. (1999). MEMS Reliability for Space Applications by Elimination of Potential Failure Modes through Testing and Analysis. *SPIE, Micromachining and Microfabrication Meeting*. Santa Clara, CA.

[15] Xu, Z.-D., & Wu, Z. (2009). Sensitivity Analysis of Acceleration-Based Energy Damage Detection Strategy to Load Excitations and Sensor Placement. *Journal of Intelligent Material Systems and Structures*, *20*(4), 413-423. doi: doi: 10.1177/1045389X08095183

[16] Lowrie, C., Desmulliez, M., Hoff, L., Elle, O. J., & Fosse, E. (2009). Fabrication of a MEMS Accelerometer to Detect Heart Bypass Surgery Complications. *Sensor Review*, *29*(4), 319-325. doi: 10.1108/02602280910986557

[17] Petsch, K., & Kaya, T. (2012). Design, Fabrication, and Analysis of MEMS Three-Direction Capacitive Accelerometer. *Proceedings of the 2012 American Society for Engineering Education North-Central Section Conference*.

[18] Lemkin, M., & Boser, B. E. (1999). A Three-Axis Micromachined Accelerometer with a CMOS Position-Sense Interface and Digital Offset-Trim Electronics. *IEEE Journal of Solid-State Circuits*, *34* (4), 456-468.

[19] Luo, H., Fedder, G. K., & Carley, L. R. (2000). A 1 mG Lateral CMOS-MEMS Accelerometer. *Proceedings of the IEEE Thirteenth Annual International Conference on Micro Electro Mechanical Systems,* (pp. 502-507). Miyazaki, Japan.

[20] Maudie, T., Hardt, A., Nielsen, R., Stanerson, D., Bieschke, R., & Miller, M. (2003). MEMS Manufacturing Testing: An Accelerometer Case Study. *Proceedings of the 2003 International Test Conference*.

[21] Yurish, S. Y. (2005). Practical Circuits and Interface Techniques for MEMS Accelerometers with Quasi-Digital Output. *Sensors and Transducers Journal*, *58* (8), 352-359.

[22] Marinkovic, B., Kaya, T., & Koser, H. (2011). Characterization of Ferroelectric Material Properties of Multifunctional Lead Zirconate Titanate for Energy Harvesting Sensor Nodes. *Journal of Applied Physics*, *109*(1), 1-5. doi: 10.1063/1.3524271

[23] Liu, Y., Tian, G., Wang, Y., Lin, J., Zhang, Q., & Hofmann, H. F. (2008). Active Piezoelectric Energy Harvesting: General Principle and Experimental Demonstration. *Journal of Intelligent Material Systems and Structures*, *20*(5), 575-585. doi: 10.1177/1045389X08098195

[24] Lee, T., Lee, D. H. Y., Liaw, C. Y. N., Lao, A. I. K., & Hsing, I.-M. (2000). Detailed Characterization of Anodic Bonding Process between Glass and Thin-Film Coated Silicon Substrates. *Sensors and Actuators*, *86*, 103-107.

[25] Schmidt, M. A. (1998, August). Wafer-to-Wafer Bonding for Microstructure Formation. *Proceedings of the IEEE, 86*(8), 1575-1585. doi: 10.1109/5.704262

[26] Masson, J., St-Gelais, R., Poulin, A., & Peter, Y.-A. (2010). Tunable Fiber Laser Using a MEMS-Based in Plane Fabry-Pérot Filter. *IEEE Journal of Quantum Electronics*, *46*(9), 1313-1319. doi: 10.1109/JQE.2010.2050299

[27] Miller, S. L., Rodgers, M. S., LaVigne, G., Sniegowski. J. J., Clews, P., Tanner, D. M., et al. (1998). Failure Modes in Surface Micromachined Microelectromechanical Actuators. *Proceedings of the 36th Annual IEEE International Reliability Physics Symposium,* (pp. 17-25). Reno, NV. doi: 10.1109/RELPHY.1998.670437

[28] Werner, F.-M., & Preston, J. M. (2008). Solutions for Testing MEMS Devices at the Wafer Level. Retrieved from http://www2.electronicproducts.com/Solutions_for_testing_MEMS_devices_at_the_wafer_level-article-farcsuss_jul2008-html.aspx

Biographies

THOMAS WHITE is currently a mechanical engineering undergraduate and student researcher working for Kaya Lab (2010-present). He has presented his work at the 2013 ASEE Midwest Conference in Columbus, Ohio, and posters at the Capital and Student Research and Creative Education Endeavors events. Mr. White may be reached at white1ts@cmich.edu

KEVIN PETSCH is currently a graduate student at Michigan State University and works at GE. His research focuses on micro-electromechanical systems. He has a B.S. from Central Michigan University (Electrical Engineering 2012). Mr. Petsch may be reached at petsch1k@cmich.edu

TOLGA KAYA is an Assistant Professor of Electrical Engineering in the School of Engineering and Technology at Central Michigan University. He earned his B.S., M.S., and Ph.D. degrees from Istanbul Technical University (Electronics and Communications Engineering) in 1999, 2002, and 2007 (Electronics Engineering), respectively. His research interestes include micro-scale sensor development and bacterial cell manipulation. Dr. Kaya may be reached at kaya2t@cmich.edu

READING AND WRITING CIRCUIT DESIGN FOR PROGRAMMABLE METALLIZATION CELLS

Dhirender Singh, California State University, Long Beach; Fei Wang, California State University, Long Beach

Abstract

A transistor-level read/write circuit for non-volatile Random Access Memory based on a programmable metallization cell (PMC) was designed using CMOS technology. The innovative write circuitry provided appropriate positive and negative voltage biasing required by the PMC memory cell. The read circuit involved circuitry for sensing the current induced by a very low voltage applied across the PMC cell. The circuit also consisted of row and column access circuits to facilitate memory cell addressing. Simulation of the circuit was performed using PSPICE in order to verify the functionality of the circuit under a variety of inputs.

Introduction

Non-volatile memory is a category of memory devices that can retain information without requiring electric power to be applied. Usually, this kind of memory device is used for long-term persistent information storage purposes. Nowadays, the demand for massive information storage increases rapidly because the density and read/write speed of memory devices are key factors for technology advancement. Among all non-volatile memories, chalcogenide-based non-volatile memory is one of the most promising technologies, due to their fast read/write speed and high scalability. Moreover, since information storage is based on transitions between crystalline phases, or based on electrochemical reactions, chalcogenide-based devices display outstanding data retention characteristic, especially when compared to flash memories that rely on electric charge storage.

The design presented in this paper focuses on a programmable metallization cell (PMC), which is a relatively new chalcogenide-based non-volatile memory [1]. This type of memory device controls the formation/dissolution of metal conductive links in a solid state electrolyte through electrochemical methods [2], [3]. Therefore, the resistivity of the solid state electrolyte can be switched between high and low states for data recording purposes. Materials used as active recording layers for PMC are metal-doped chacogenides that include Ag-Se, Ag-S [4], Ag-Ge-Se [2], [3], Ag-Ge-S [5], Cu-S [6] etc. PMC has the advantages of short recording time, low recording power, as well as better scaling capability [2], [3].

Since the read/write operations of PMC devices are unique, corresponding read/write circuitry needs to be designed in order to take advantage of their fast switching speeds. One of the challenges in read/write circuit design is to provide the reverse biasing necessary to erase the data, while using a single-ended power supply. In this study, the authors developed a transistor-level read/write circuit for a PMC. The innovative write circuitry provided appropriate positive and negative voltage biasing required by the PMC memory cell. The read circuit involved circuitry for sensing the current induced by a very low voltage applied across the PMC cell. The circuit also consisted of row and column access circuits to facilitate memory cell addressing. Simulation of the circuit was performed using PSPICE in order to verify the functionality of the circuit under a variety of inputs.

Basic Operation of the PMC

A typical PMC cell has three major layers, as illustrated in Figure 1 [5]. The illustrated device uses a silver-based solid electrolyte, fabricated on a glass substrate, using thermal evaporation methods. Previous studies [5] showed that the device performance (e.g., on/off resistance and switching thresholds) greatly depend on the thickness of the chalcogenide electrolyte layer. Therefore, the design in this current study aimed to drive a PMC based on Ag-Ge-S with an active layer thickness of 60 nm.

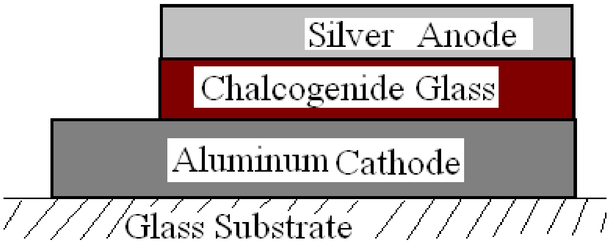

Figure 1. Cross-sectional View of a PMC Cell Structure Fabricated on a Silver-based PMC Glass Substrate [5]

Figure 2 shows the I-V characteristics of a PMC cell, based on Ag-Ge-S that was fabricated in a previous study by the authors [5]. This testing device had an active layer thickness of 60 nm. The current through the PMC cell was measured, while tuning voltage across the device. The voltage was increased from 0 V to 1 V, then decreased to -1 V, and finally brought back to 0 V. During this process, the resistance of the device showed a transition from a high to a low state at 0.8 V (SET voltage), and a transition from a low to a high state at around -0.5 V (RESET voltage). The high resistance (corresponding to a logical 0 or OFF) was three orders of magnitude larger than the measured low resistance (corresponding to a logical 1 or ON).

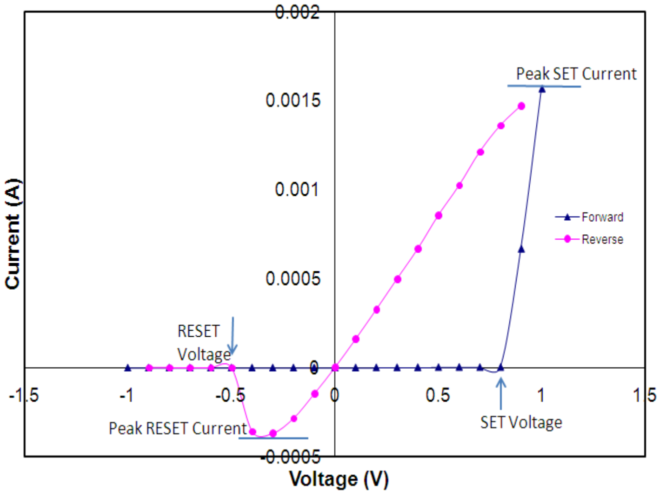

Figure 2. I-V Characteristics of a 100x100 μ m and 60 nm Thick PMC Testing Cell [5]

To SET the PMC cell to a logical 1, a positive voltage above the SET threshold was needed. This voltage pulse needed to be maintained for 30-50 ns, or until the electrochemical process in the active layer was completed, which usually took several ns. This fast-setting speed was one of the most significant advantages of the PMC devices.

To RESET the PMC cell to a logical 0, a negative voltage below the RESET threshold was needed. RESET took a shorter time than SET. Therefore, a 30-50 ns negative pulse was more than sufficient to RESET the device. In terms of circuit design, the voltage across the PMC device had to be able to change polarity, while using a single-sided power supply. This could be realized using a NMOS transistor plus a PMOS transistor. Only a very low voltage pulse, as low as 0.1 V, was needed for a read operation. This process was similar to a typical read process of memory cells. The device current was compared to a reference value. If the device current was higher than the reference, a logical 1 was identified; if the device current was lower than the reference, a logical 0 was identified.

Design and Simulations

A block diagram of the read/write circuit for the PMC memory cell is presented in Figure 3.

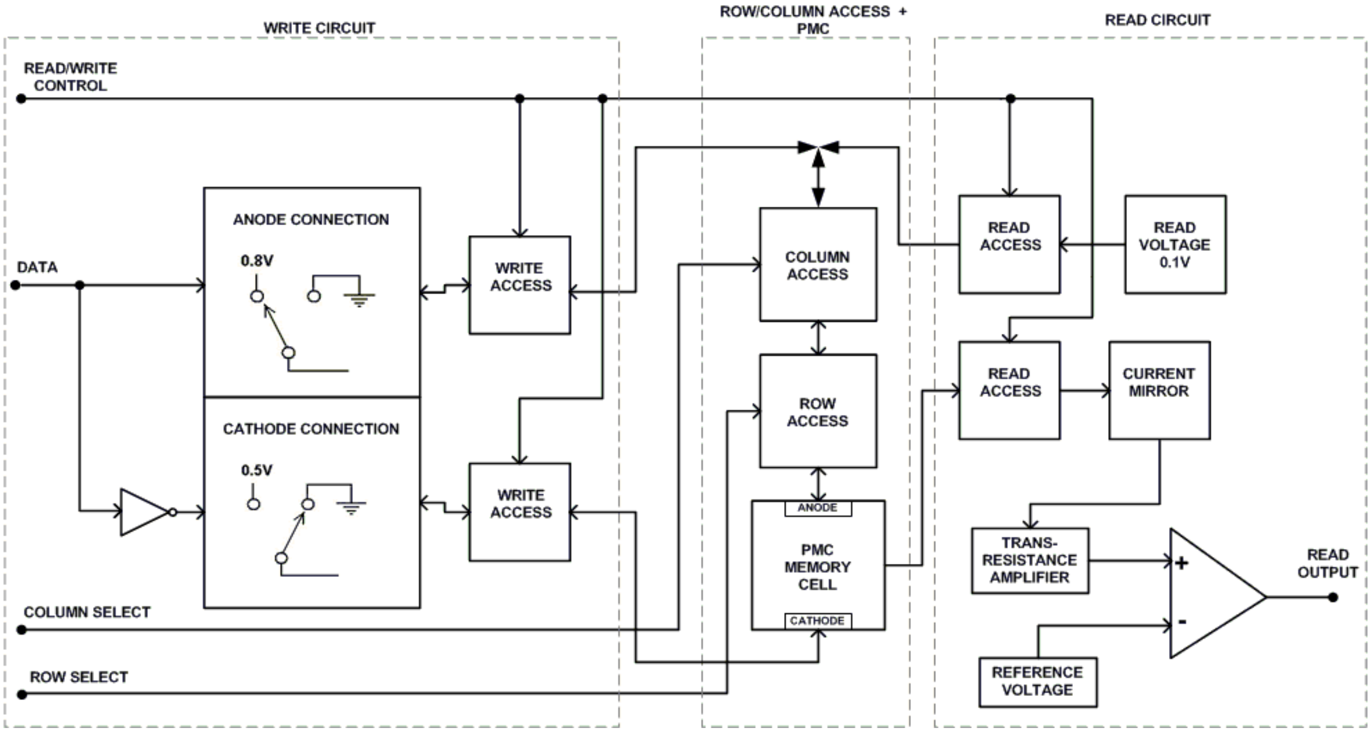

Figure 3. Block Diagram of the Read/Write Circuit Design

The design method and the corresponding circuitry for recording data on a PMC cell (see Figure 4) is presented here. Typically, a logical 1 is recorded on the PMC cell by applying a positive voltage of 0.8V or above from the anode to the cathode; whereas, a logical 0 is recorded by applying a negative voltage of -0.5V or below from the cathode to the anode. The key design issue here was to be able to apply both positive and negative voltages across the PMC cell, while using a constant positive supply voltage (i.e., three volts in this case). To implement this function, a terminal switching mechanism was constructed using two pairs of complimentary MOS transistors. Depending on the input data, the transistor pairs would toggle the anode and cathode terminals of the PMC between voltage sources and ground. The transistor pair consisting of M_8 (PMOS) and M_{11} (NMOS) was active when the input data was a logical 1, while the pair consisting of M_{10} (PMOS) and M_9 (NMOS) was active when the data was a logical 0.

When the input data was a logical 1, transistor M_8 connected the anode to a voltage reference of 0.8 V, and M_{11} connected the cathode to ground; thus, a positive current flow occurred from the anode to the cathode. As explained earlier, the positive bias of 0.8 V set the PMC cell to a logical 1 (i.e., low-resistance state). During this operation, the other pair of transistors (M_{10} and M_9) was turned off. A similar operation was conducted in the reverse direction when the input data was a logical 0 through transistor pair M_{10} and M_9. Transistor M_{10} connected the cathode to a voltage source of 0.5 V, and transistor M_9 connected the anode to ground. This resulted in a negative current flow from the cathode to the anode. The negative voltage bias of -0.5 V set the PMC cell to a logical 0 (i.e., high-resistance state).

Additionally, CMOS switches were employed for row, column, and read/write control. The write circuit involved a current flow in two directions; therefore, a specially constructed bi-directional switch was used to control row and column access. Moreover, these switches contained an additional pair of PMOS and NMOS transistors, unlike the typical CMOS switches, for extra protection from leakage currents, which might have altered the original PMC resistance state. These switches allowed access to the PMC cell only when the inputs on both row and column lines were active high. Transistors M_{16}, M_{17}, M_{20}, and M_{21} formed the row access switch, whereas transistors M_{18}, M_{19}, M_{22}, and M_{23} formed the column access switch.

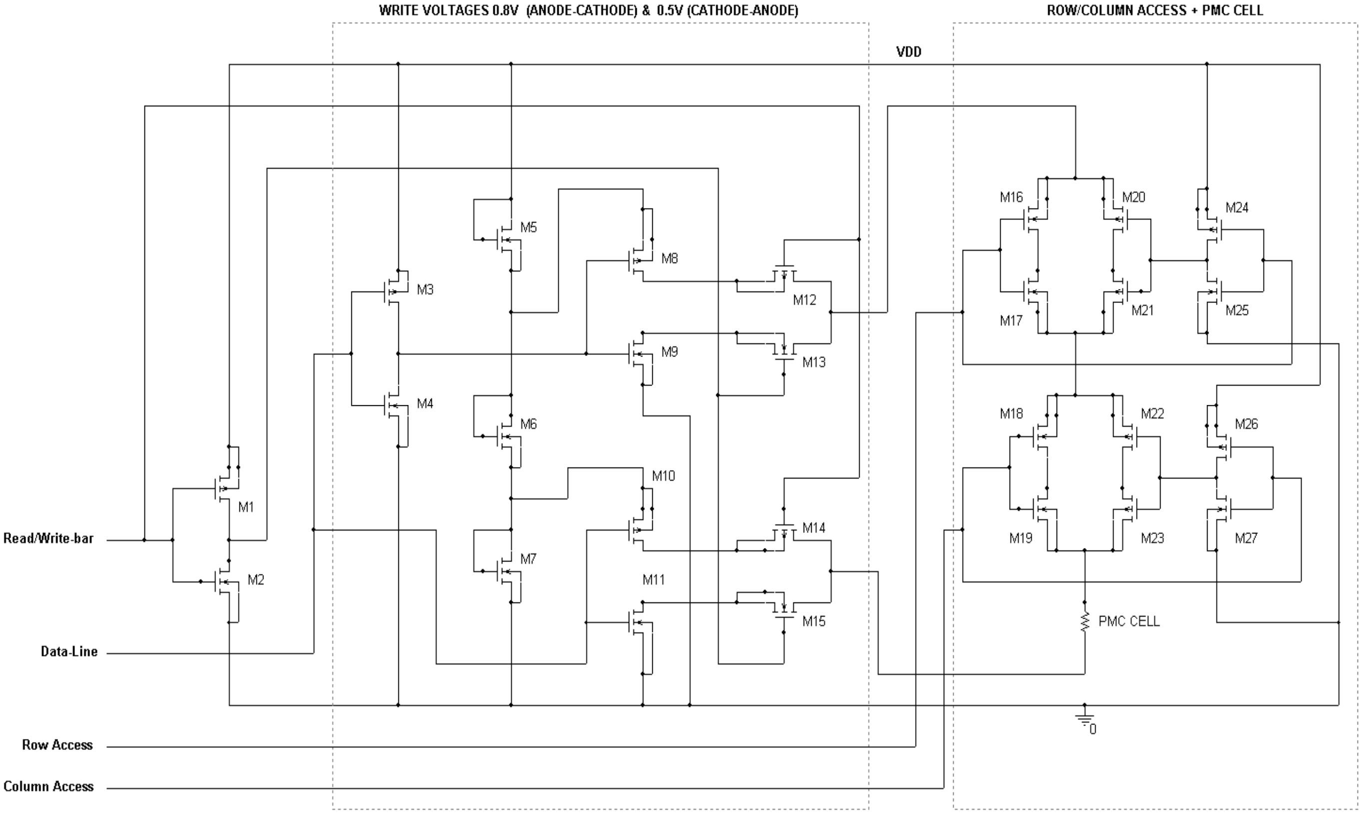

Figure 4. Write Circuitry for One PMC Cell

For controlling the write access, typical CMOS switches were used. These switches were controlled by the R/W_bar line. They allowed a current flow from the reference voltage sources through the PMC cell only when the R/W_bar line was active low. One of the switches was made up of transistors M_{12} and M_{13}, and the other of M_{14} and M_{15}. The read circuit for determining the resistive state of a PMC memory cell is shown in Figure 5. The circuit consisted of a current mirror, a trans-resistance amplifier, and a voltage comparator. Additionally, read access switches were also involved in the circuit.

A read voltage, V_{read}, of 0.1 V was applied across the PMC cell in order to read the data stored in the cell. This voltage caused a current flow of around 1 nA for a high-resistance state, R_{high}, representing a logical 0; and, 1 uA for a low-resistance state, R_{low}, representing a logical 1. This current passed through a current mirror and was subsequently converted to an amplified voltage using a trans-resistance amplifier. Finally, the voltage output of the amplifier was compared with a reference voltage, V_{ref}, using a differential amplifier. The resistor R_1 in the trans-resistance stage played an important role in terms of creating an appropriate voltage margin between the high and low states. It was selected based on the read voltage of 0.1V, the ratio of transistors in the current mirror, M_{20}:M_{21}, and the low state resistance of the PMC cell, given in Equation (1):

$$R_1 = \left(\frac{Vdd}{Vread}\right) \times \left(\frac{(W/L)1}{(W/L)2}\right) \times R_{low} \quad (1)$$

A logical 0 (high resistance) stored in the cell resulted in a voltage output lower than the reference voltage from the trans-resistance amplifier, while a logical 1 (low resistance) resulted in a voltage greater than the reference voltage. Thus, the differential amplifier output a high voltage for a logical 1, and low voltage for a logical 0 stored in the cell.

For controlling the read access, a typical CMOS switch consisting of transistors M_5 and M_6 was used. It allowed the current flow from the reference source into the PMC cell only when the R/W_bar input was active high. Additionally, an NMOS transistor, M_{19}, was also employed to block the write circuit's current from entering into the read circuit. This transistor allowed current flowing through the PMC cell into the Read circuit only when the R/W_bar input was active high. The simulations of the circuits were performed in order to verify the circuit behavior under the two different resistive states of the PMC cell.

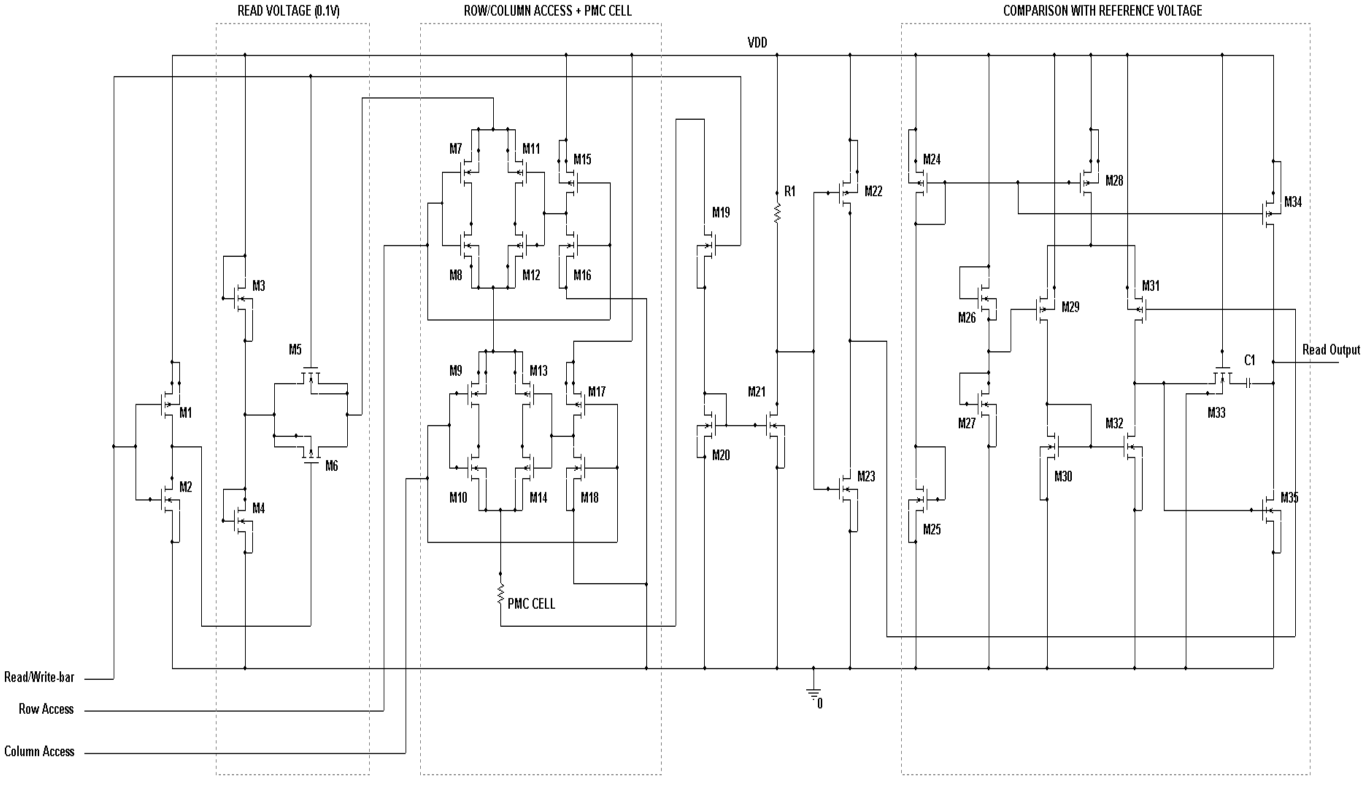

Figure 5. Read Circuitry for One PMC Cell

Figure 6 shows the simulation output of the read/write circuits for a PMC cell that was originally in a low-resistance state. This simulation was performed assuming a PMC resistance of 330 KΩ. The observed outputs were valid only when both row and column inputs were high; in rest of the cases, the outputs were all zero. When the R/W_bar line was low, the voltage on the PMC cell was observed to be 0.8 V and -0.5 V for input data of a logical 1 and a logical 0, respectively, while the read output remained 0 V (low). In the other case, when R/W_bar line was high, the PMC voltage was observed to be 0.1 V (read reference voltage) and the read output was 3 V (a logical 1).

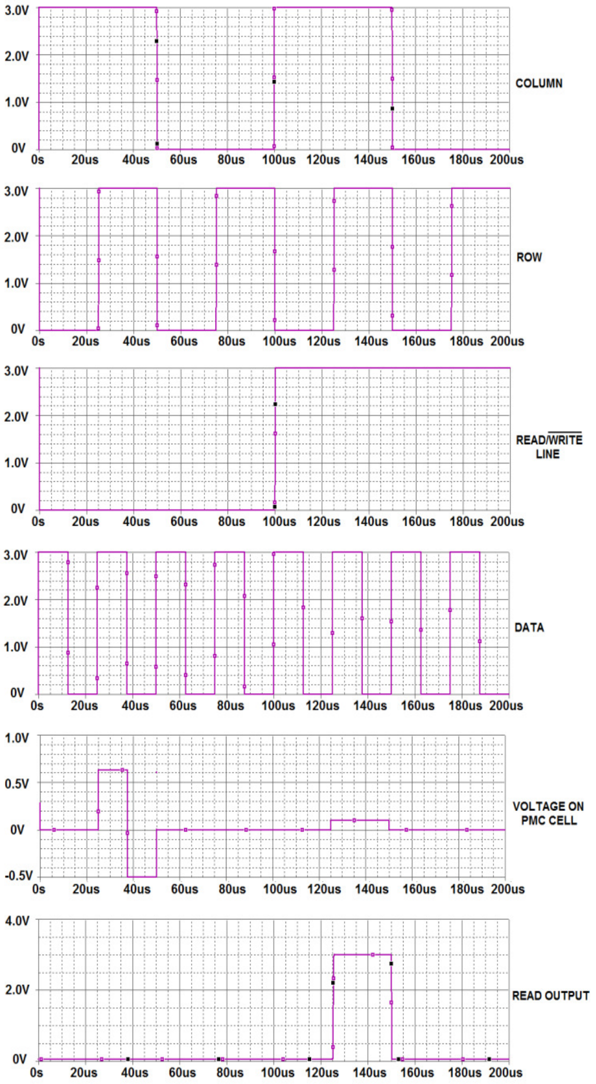

Figure 6. Simulation for an Initially ON (low-resistance) PMC

Figure 7 shows the simulation output of the read/write circuits for a PMC cell that was originally in a high-resistance state. This was simulated assuming a resistance of 330 MΩ. Similar to the previous simulation, the PMC voltages were observed to be 0.8 V and -0.5 V for logical inputs of 1 and 0, respectively, when the R/Wbar input was low, while a voltage of 0.1 V was observed on the PMC when R/Wbar input was high. But unlike the previous case, the read circuit output voltage was observed to be 0 V (low), irrespective of the R/W_bar status. This signified that a logical 0 (low) was stored in the cell. From these simulation results, it could be concluded that the circuit allowed access to the PMC cell only when both row and column inputs were high. It was also to be noted that the write circuit output was independent of the PMC's resistance state, which is what was wanted, while the read output voltage was purely based on the PMC's resistance state.

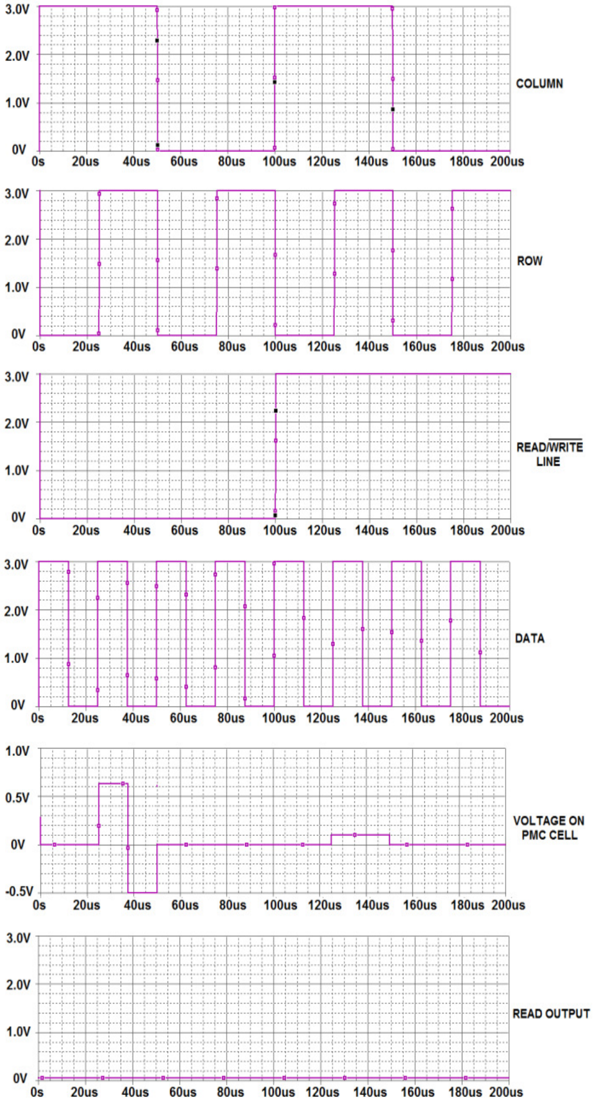

Figure 7. Simulation Results for an Initially OFF (high-resistance) PMC

Typically, a PMC cell requires a pulse of 30-50 ns for setting or resetting it. Additionally, the write circuit delay was determined to be 1.75 ns, as shown in Figure 8. Therefore, the clock frequency for the PMC write operation should be appropriately chosen to accommodate for the aforementioned time constraints and delay.

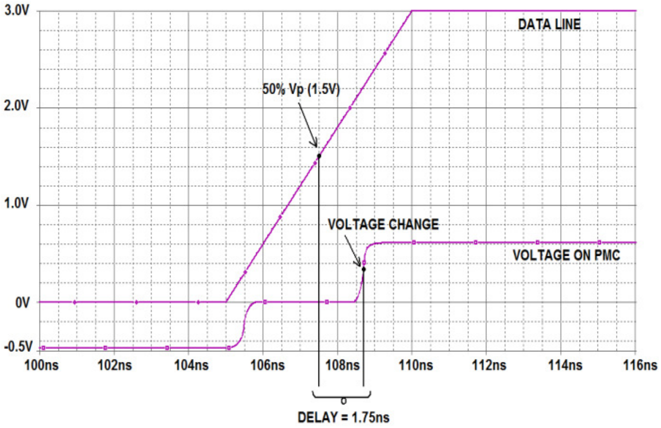

Figure 8. Simulated Propagation Delay

Conclusions

Read/write circuitry was designed specifically for a programmable metallization cell. The circuit was implemented using CMOS technology, and PSPICE simulation results showed the successful operation of this design.

References

[1] Wang, F., & Wu, X. (2009). Non-volatile Memory Devices Based on Chalcogenide Materials. *Proceedings of the 6th International Conference on Information Technology: New Generations,* (pp. 5-9). Las Vegas, NV.

[2] Kozicki, M. N., Yun, M., Yang, S. J., Aberouette, J. P., & Bird, J. P. (2000). Nanoscale Effects in Devices Based on Chalcogenide Solid Solutions. *Superlattices and Microstructures, 27*(5/6), 485-488.

[3] Kozicki, M. N., Gopalan, C., Balakrishnan, M., Park, M., & Mitkova, M. (2004). Nonvolatile Memory Masel on Solid Electrolytes. *Non-Volatile Memory Technology Symposium Proceedings,* (pp.15-17).

[4] Chaitanya, I. (2006). Metal-Semiconductor-metal Junctions with Silver Sulfide Barrier Layer [presentation]. *American Physical Society March Meeting*. Baltimore, MD.

[5] Wan, F., Dun, W. P., Jai, M., De Le, C., & Vicker, N. (2011). The Effects of Active Layer Thickness on Programmable Metallization Cell Based on Ag–Ge–S. *Solid-State Electronics, 61*(1), 33-37.

[6] Sakamot, T., Sunamur, H., Kawaur, H., Hasegaw, T., Nakayam, T., & Aon, M. (2003). Nanometer-scale Switches Using Copper Sulfide. *Applied Physics Letters, 82*, 3032.

Biographies

DHIRENDER SINGH works as an ASIC Engineer at Microchip Semiconductor in India. He earned his M.S. degree in Electrical Engineering from California State University in 2010. Mr. Singh may be reached at dsingh247@gmail.com

FEI WANG is an Associate Professor of Electrical Engineering at California State University, Long Beach. She earned her Ph.D. degree from the University of Cincinnati in 2005. Before she joined California State University, Long Beach, she worked as an Assistant Professor at California Polytechnic State University from 2005-2007. Dr. Wang may be reached at fei.wang@csulb.edu

DESIGN AND TEST OF AN IRONLESS AXIAL FLUX PERMANENT MAGNET MACHINE USING A HALBACH ARRAY

Todd D. Batzel, Penn State Altoona; Andrew M. Skraba, Penn State Altoona; Ray D. Massi, Penn State Altoona

Abstract

Conventional permanent magnet electric machines utilize ferromagnetic cores of high permeability. The high core permeability relative to the surrounding material helps to concentrate the magnetic flux in the core, and guide the flux across the air gap of the machine. An ironless machine design removes the ferromagnetic core, thus eliminating core losses due to hysteresis and eddy currents. As a result, the machine is capable of improved efficiency even at high speeds, where core losses are problematic in conventional designs. The ironless design also has zero cogging torque, reduced weight, and is simple to manufacture. The axial flux implementation of this machine was shown to have performance advantages over the radial flux machine, and also permits an adjustable air gap length.

However, the absence of an iron core generally results in lower air gap flux, which is a handicap in terms of torque production. For high torque, the air gap magnetic flux density should be as high as possible. Although this is difficult to achieve without an iron core, a Halbach array of permanent magnets can be used to focus the magnetic flux toward the air gap. The Halbach magnet array also produces a naturally sinusoidal air gap flux distribution, which helps to reduce torque ripple, when operated with synchronous drives. The Halbach array requires additional permanent magnetic material, however, which yields higher material cost.

In the paper, the authors present the design and test results of an ironless axial flux permanent magnet motor. The machine requirements and drive constraints (power, speed, diameter, and available bus voltage) were used to size the motor. The rotor design consisted of optimizing the air gap length and determining magnet dimensions. From the identified air gap length, the stator arrangement and coil design were then realized. The machine was constructed and tested, with predicted performance compared to observed experimental results.

Introduction

Traditional permanent magnet machines are constructed with an iron core in both the rotor and stator in order to reduce the machine's magnetic reluctance and obtain a strong air gap flux. The continued advancement of high energy density permanent magnet materials has enabled the development of ironless electric motors [1], [2], while maintaining a sufficient air gap magnetic flux. The elimination of iron has several advantages: increased efficiency, due to the absence of core losses [3], [4]; no cogging torque [5]; and, light weight [6]. Due to these advantages, the ironless machine is especially attractive in applications such as high-frequency energy storage flywheels [7], large [8] and small [9], [10] vehicle propulsion systems, aerospace auxiliaries [11], renewable energy systems [12], and general-purpose industrial servos [13]. The drawback to the ironless motor is a low air gap magnetic flux density and a high current ripple resulting from the use of traditional pulse width modulation (PWM) electric drives to low inductance machines such as those without iron cores [14].

Permanent magnet machine topologies are generally classified as radial flux or axial flux machines. In the common radial flux machine, the permanent magnets are arranged on the rotor (an inner cylinder) so that the torque is produced from magnetic flux that is perpendicular to the rotor shaft. In the axial flux machine [15], the magnets are arranged on a disk so that magnetic flux flowing parallel to the shaft produces the torque. Studies [16-18] have shown that the axial flux design will generally result in higher specific torque and smaller volume per unit torque, respectively, than the radial machine. Although there are many variants of the axial flux machine, the topology adopted for this study utilized two external rotor disks sandwiched around a single internal stator. This modular topology allowed several identical axial rotor stages to be stacked onto a single shaft in order to increase output torque as needed.

Without an iron core, a large effective air gap is unavoidable, and a higher volume of permanent magnet material is necessary to establish sufficient air gap flux. To address the low air gap magnetic flux that is typically present in an ironless machine, a Halbach array [19] was employed for this study. An arrangement of discrete permanent magnet segments with their angle of magnetization varying with respect to the stator winding magnetic axis forms a Halbach array. A Halbach array, where the permanent magnets are at 0, 90, 180, and 270 degrees from the winding is shown in

Figure 1. As shown, the magnetic field produced by the Halbach array is focused on one side of the magnetic array, and nearly zero on the other side, so that rotor backiron is unnecessary. This focusing of the field by the Halbach array was used to obtain high air gap flux (where flux is needed to produce torque) even in the absence of an iron core.

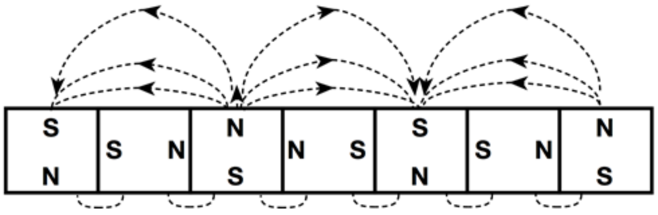

Figure 1. Halbach Magnetic Array

In this paper, the authors present the development and testing of an axial gap, dual-rotor single-stator motor/ generator. The mechanical design of the machine is also presented, and both the rotor and stator electromagnetic design aspects are discussed in detail. The test results will then be used to show that the resulting air-cooled ironless design compares favorably with commercially available iron-core machines in terms of specific torque and power, torque per unit volume, and efficiency.

Machine Sizing

The sizing analysis begins with the design parameters and desired machine ratings, which are summarized in Table 1. The machine was constructed mainly for laboratory experimentation and to compare the performance of an ironless machine to commercially available iron-core machines in terms of efficiency, noise, specific torque and power, and torque per unit volume. However, this machine was appropriate for a variety of applications, including small-vehicle propulsion, aerospace or electric vehicle auxiliaries, and small-scale wind turbines.

Table 1. Machine Design Parameters

Parameter	Value
DC Bus Voltage	60 V
Torque	5.94 N-m
Base Speed	1200 RPM
Rated Current	10 A (rms)
Rated Power	1 HP
Voltage Constant	$.092\ v_{phase,pk}/\omega_e$
Torque Constant	.276 N-m/A (per phase)
Poles	6
Connection	Star (Y connection)

A starting point for determining the axial machine dimensions that would allow the machine to conform to the specifications of Table 1, was the average air gap shear stress, τ. Air gap shear stress is a measure of the torque-producing force relative to the active surface area of the rotor. In general, the air gap shear stress is similar across different sizes of the same class of machines and is, therefore, widely used as an indicator of torque per unit volume. For an axial flux machine, the average air gap shear stress (τ) is defined by Equation (1):

$$\tau = \frac{T}{A_{rotor} r_{av}} \tag{1}$$

where, T is the torque applied to the machine shaft; A_{rotor} is the active surface area, where stator current is interacting with the magnetic flux; and, r_{av} is the average radius of the rotor magnets. The active surface area is given by Equation (2):

$$A_{rotor} = \pi\left(r_o^2 - r_i^2\right) \tag{2}$$

where, r_o and r_i are the magnet outer and inner radii, respectively, as shown in Figure 2. Since from Equation (3):

$$r_{av} = .5\left(r_o + r_i\right) \tag{3}$$

then, Equation (4) gives the ratio of inner to outer magnet radius:

$$\alpha = {}^{r_o}\!/_{r_i} \tag{4}$$

and, Equation (5) gives the torque:

$$T = \left(1-\alpha^2\right)\left(1+\alpha\right)\frac{\pi\tau}{2} r_o^3 \tag{5}$$

The relation between outer radius and air gap shear stress can be expressed by Equation (6):

$$r_o = \left(\frac{2T}{\left(1-\alpha^2\right)\left(1+\alpha\right)\pi\tau}\right)^{1/3} \tag{6}$$

Thus, the outer radius of the machine is dependent upon the rated torque (see Table 1), the air gap shear stress, and the ratio of the inner radius to the outer radius. Clearly, the ratio of the inner to outer radius of the machine is an important design parameter. Many studies have been performed to find the optimum ratio. In the study by Campbell [20], the ratio was shown to be 0.57, while Patterson et al. [21] determined the optimum ratio to be 0.63. Huang et al. [22] suggested that the optimum ratio depends on many other design parameters such as flux density, speed, and number of poles; but, they went on to say, the optimum ratio is generally in a limited range near the results cited in the other two studies. Based on these three studies, the inner to outer radius ratio, α, was selected to be 0.5. This value is in the narrow range cited in the studies and is also a value that would allow a commercially available arc magnet to be obtained without the expense associated with custom magnet dimensions.

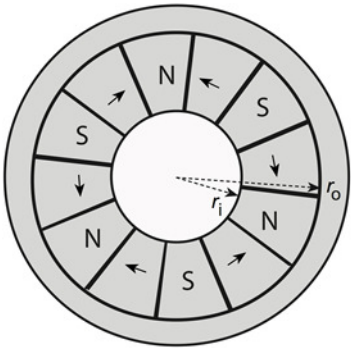

Figure 2. Axial Dimensions

In Equation (6), the average air gap shear stress must also be selected to determine the machine radius. Air gap shear stress is generally similar for different sizes of the same class of machines [23], [24]. Of the various classes of electric machines, the permanent magnet synchronous motor (PMSM) is capable of the highest air gap shear stress. In a study by Miller [24], high-performance industrial PMSM designs without special provisions for forced cooling were found to have an air gap shear stress rating in the range from 13.75 to 27.5 kPa. For the present design, the upper range of shear stress (27.5 kPa) was selected as a starting point for sizing the ironless machine. With this air gap shear stress, along with the rated machine torque, the outer diameter, r_o, was found to be 1.95 inches, by using Equation (6). This was rounded up to 2 inches because of off-the-shelf magnet availability in that size. Consequently, the inner radius, r_i, was one inch.

The fundamental relationship for torque production in an axial flux permanent-magnet (PM) machine is given by Equation (7), which links the force F, on a wire of length l, carrying a current i in a uniform magnetic field B, where the field and current are perpendicular to one another:

$$F = Bli \tag{7}$$

Consider now the linear current density, Z (in A/m), which is the total current per unit length around the air gap occupied by the stator coils. This is also often called the electrical loading of the machine. The force on the conductors can be related to the air gap shear stress and, therefore, to the electrical loading by Equation (8):

$$\tau = \frac{F}{A_{rotor}} = \frac{Bli}{lw} = \frac{Bi}{w} = BZ \tag{8}$$

where, w is the average linear length around the air gap, and B is the mean air gap flux density per pole (in units Teslas)—or equivalently the magnetic loading. Note that air gap shear stress is dependent upon the electrical and magnetic loading points. For the sinusoidal flux density distribution, the mean air gap flux density per pole is related to the peak flux density, B_m , by Equation (9):

$$B = \frac{2B_m}{\pi} \tag{9}$$

In order to achieve the desired air gap shear stress of 27.5 kPa, a mean magnetic flux density, B, near 0.5 Tesla, and Z near 55,000 A/m, was chosen.

Stator Design

From the sizing computations, an electrical loading (Z) of 55,000 A/m was chosen as a baseline. Now, using the electrical and magnetic loading, rated current, and dc bus voltage, the coil size and number of turns per phase of the stator may now be specified.

From the radial dimensions of the permanent magnets (r_o and r_i), the stator coil dimensions can be determined. For ease of manufacture, a non-overlapping winding was used, with one coil per phase for each pole pair. For the 6-pole machine, this translated to three coils per phase, and a total of nine coils for the 3-phase machine. Each coil in the same phase was connected in series, and the phases connected in a star (or "Y") configuration. The nine non-overlapping coils each occupied 40°, or 1/3 of a magnetic pole pair. The coil shape was trapezoidal, as shown in Figure 3, with an average area enclosed by the winding of $A_{coil} = 5\text{x}10^{-4}m^2$.

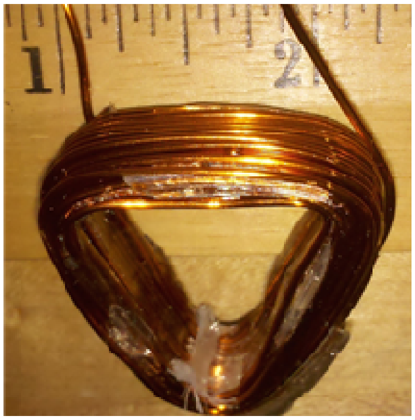

Figure 3. Stator Coil

From the DC bus operating voltage of 60 V, and the star connection, each phase was expected to develop a peak emf of $60/\sqrt{3}$ or 34.6 V at the base speed of 1200 RPM. To find the number of turns per phase, N_{ph}, to accomplish this, Faraday's law was used:

$$e_{ph} = N_{ph} A_{coil} \frac{dB(\theta)}{dt} \tag{10}$$

where, e_{ph} is the per-phase emf, and where the flux density varies sinusoidally around the air gap according to Equation (11):

$$B(\theta) = B_m \sin(\omega_e t) \tag{11}$$

The term ω_e represents the electrical frequency of the stator voltage, as determined by the shaft speed and the number of poles. At the base speed of 1200 RPM, ω_e is 377 rad/sec (or 60 Hz). From the two previous equations,

$$e_{ph} = N_{ph} A_{coil} \omega_e B_m \cos(\omega_e t) \tag{12}$$

Thus, the number of turns per phase required to produce a peak per phase emf is given by Equation (13):

$$N_{ph} = \frac{e_{ph}}{A_{coil} \omega_e B_m} \tag{13}$$

The number of turns per phase, N_{ph}, was determined to be 233. Thus, with three coils per phase, each coil would have 77 turns. For the actual coil construction, 18-gauge (round) class H magnet wire was chosen to handle the required 10 A_{rms}, yielding an acceptable conductor current density (J) of 8 A/mm^2. An 18-gauge conductor has a diameter of approximately 1.2 mm. Thus, to accommodate the 77 turns, the coil needs to have a height of approximately 15 mm or 0.59 inches. Half of a single coil is shown in Figure 3. Also, the total resistance per phase was computed to be 0.39 Ω.

Any torque, speed, or position controller for a PMSM requires rotor position feedback. To accommodate this need, three Hall-effect sensors were installed onto the stator between the phase A, B, and C coils to allow coarse rotor position detection sufficient to drive the ironless machine with trapezoidal, or six-step currents. A rotary encoder could be added to the shaft if higher resolution rotor position feedback is preferred. The electrical loading for the stator design at the outer radius, r_{av}, is the product of the total number of wires (two wires per turn) per coil, multiplied by number of coils per phase, the number of phases, and the rated current—divided by the length around the gap at that radius, as given by Equation (14):

$$Z = 2 m_1 N_{ph} \frac{i_{rms}}{2\pi r_{av}} \tag{14}$$

where, m_1 is the number of phases. Thus, Z=58,600 A/m, which essentially meets the target electrical loading of 55,000 A/m specified in the sizing section.

Rotor Design

As shown in Equation (8), the designated average air gap shear stress of 27.5 kPa can be realized by many combinations of electrical and magnetic loading. When selecting electrical and magnetic loading, it is important to consider that they compete with one another for space in a fixed-size machine. For example, if magnetic loading is increased by reducing the air gap length, this leaves less room for electrical conductors in the air gap and, therefore, a decrease in the electrical loading. An electrical loading of 55,000 A/m, and magnetic loading of approximately 0.5 Tesla was selected in this case to yield the targeted air gap shear stress. In the machine sizing section, the rotor magnets were selected to have inner and outer radii of one and two inches, respectively. For a 6-pole Halbach rotor disk with four magnets per pole pair, each magnet had to have an arc of 30°. The magnets to be used were NdFeB grade N52, with B_r =1.48 T. To implement the Halbach array, half of the magnets were magnetized in the axial direction, others in the circumferential direction, as shown in Figure 2.

The axial thickness of the permanent magnets could then be determined. Theoretical formulas for air gap flux density produced by Halbach magnet arrays have been developed by Winter et al. [25]. From those results, the air gap flux density versus gap thickness for various magnet thicknesses was computed; the results are shown in Figure 4. Noting that the desired mean average flux density per pole (B) of 0.5 T corresponded to a peak flux density, B_m, of 0.78 T, the results showed that the magnetic loading could be achieved with a 1-inch-thick magnet using an air gap of approximately 0.65 inches. Considering that the required coil thickness was 0.59 inches, this left very little room for clearance, coil support structure, and magnet retainers. Thus, a sacrifice in magnetic loading was made in order to accommodate readily available magnets with a thickness of one inch so that the prototype ironless machine could be built with adequate clearances and magnet retainers at a reasonable cost. A conservative air gap length of 1.2 inch was selected, which in theory will reduce the magnetic loading from the target of 0.5 T to about 0.39 T. It should be noted that after the machine was fully tested, the magnet retainers and stator support structures could be reduced in thickness (or eliminated), and the coils re-wound with rectangular wire to enable the stator to fit into the targeted air gap of 0.65 inches (or even less) so that the magnetic loading target value of 0.5 T could be realized.

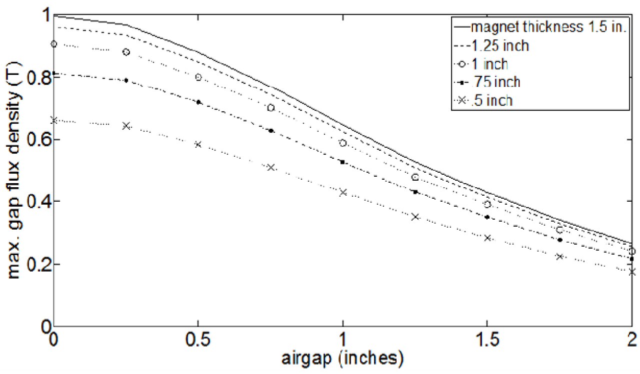

Figure 4. Air gap Flux Density versus Gap Length for Various Halbach Magnet Thicknesses

To verify the theoretical computation of the air gap flux density shown in Figure 4, the Halbach rotor disks with magnets of 1-inch thickness were positioned for various gap lengths, with the peak air gap flux density measured using a gauss meter. The experimentally measured peak flux density shown in Figure 5 for various gap lengths agree very well with the theoretical results for the 1-inch magnets shown in Figure 4. For example, in Figure 4, a 1-inch thick magnet with a gap of one inch yields a theoretical peak air gap flux density of 0.61 T. The experimentally measured peak for the same gap length, as shown in Figure 5, was 0.64 T.

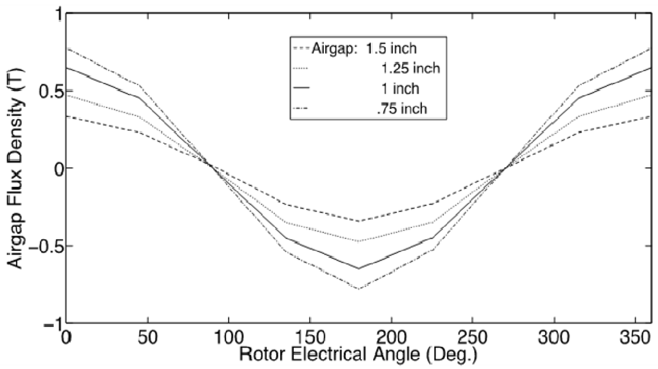

Figure 5. Measured Gap Flux versus Gap Length for a 1-inch Magnet

Machine Construction

The rotor PM disks were designed using Solidworks. The magnet disk was constructed with aluminum for light weight. Since the aluminum disk rotated with the magnets, it did not see a changing magnetic flux and, therefore, was not subject to significant eddy current losses. The Solidworks implementation of a single Halbach magnet disk, showing the magnet locations, is shown in Figure 6.

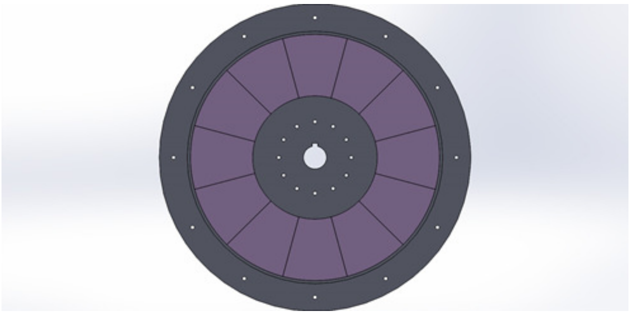

Figure 6. Solidworks Design of a Rotor Magnet Disk

In the ironless motor design, two magnet disks were sandwiched around the stator such that the Halbach array focused the magnetic field on the air gap between the disks. The full assembly—minus the stator—is shown in Figure 7. The stationary end bells shown in the figure were also constructed with aluminum, and held bearings to accommodate the rotating shaft. The magnet disks were fixed to the keyed shaft with a shaft collar and keystock. Note also that the air gap length (axial distance between the magnets) was easily adjustable. The stator (not shown) was held fixed to the end bells using screws and spacers of appropriate length. The actual Halbach rotor disk is shown in Figure 8.

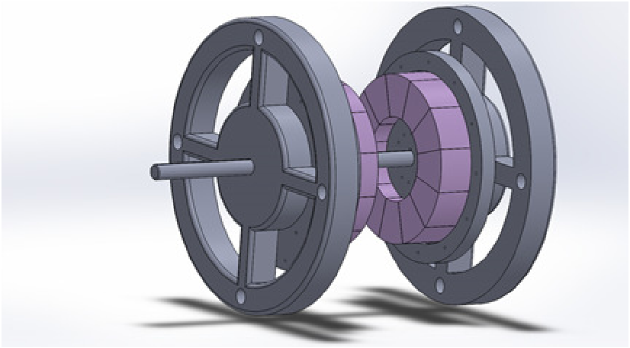

Figure 7. Dual-rotor Disks on Shaft with Endbell

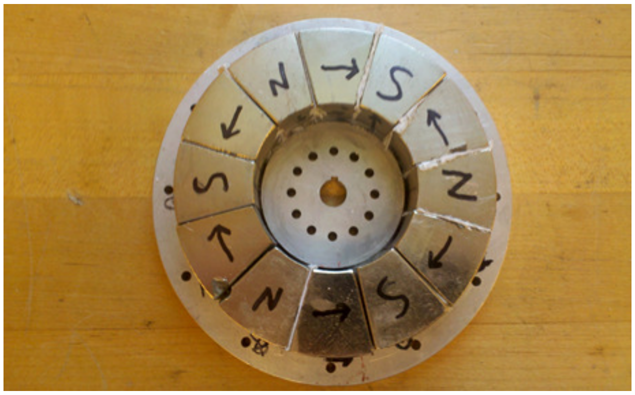

Figure 8. Rotor Disk with Halbach Array

The stator was constructed by mounting the coils onto a supporting acrylic sheet with a thickness of 3/32 inch. Each coil had a total of 77 turns. In practice, this was accomplished with two separate coils of 38 turns mounted to opposite sides of the stator support structure and connected in series. The constructed stator assembly is shown in Figure 9, and the fully constructed ironless axial flux machine in Figure 10.

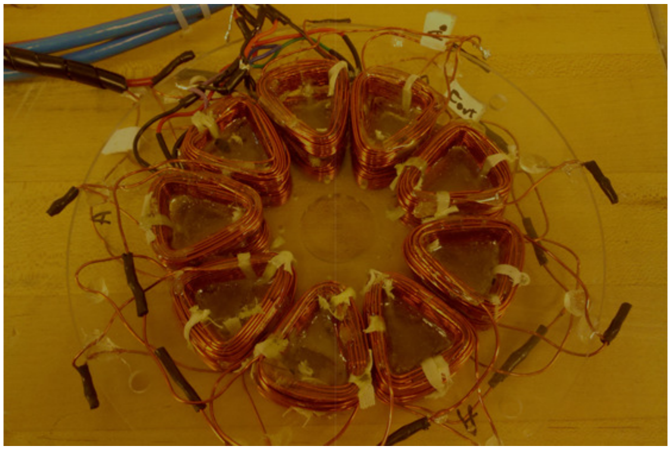

Figure 9. Stator Assembly

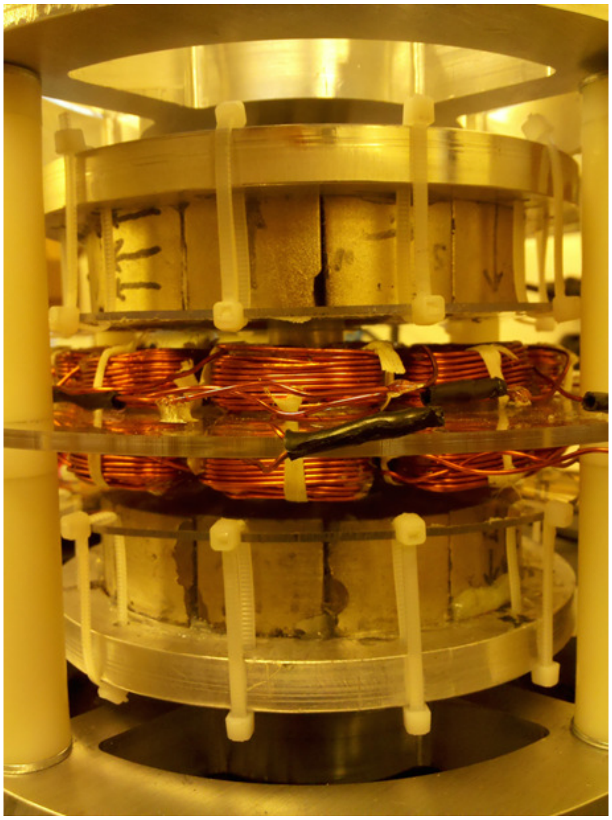

Figure 10. Constructed Ironless Axial Flux Motor

As indicated in Table 1, the voltage constant of the machine, k_e, is the computed ratio of the peak phase voltage relative to the electrical frequency. From the design parameters, the per-phase peak voltage at the rated speed was 34.6 V, since the maximum line-to-line voltage was limited by the DC bus voltage of 60 V. The electrical frequency at 1200 RPM was 377 rad/s, so the voltage constant, k_e, was .092 v-s. For the torque constant, k_t, the number of pole pairs (three for the machine of interest) had to be considered, so the torque constant, k_t, was 0.276 N-m/A per each phase. Assuming the drive enforces an optimum commutation angle using the rotor position feedback θ_e, the total machine torque was obtained from the instantaneous phase currents given in Equation (15):

$$T = k_t\left(i_a \sin\theta_e + i_b \sin\left(\theta_e - 120^\circ\right) + i_c \sin\left(\theta_e + 120^\circ\right)\right) \quad (15)$$

For sinusoidal current excitation, the torque will ideally be constant, with no ripple.

Machine Testing

For the machine test, the ironless machine was placed on a motor test dynamometer, as shown in Figure 11. The first test that was performed was to determine the voltage constant, k_e, which was computed earlier to be 0.092 v-s. To experimentally determine the voltage constant, the machine was driven as a generator with the induced phase voltages recorded, as shown in Figure 12. Note in the figure that the induced voltages are sinusoidal, with the 3-phase voltages balanced. The peak voltage in is seen to be 6.15 volts, and the electrical frequency is 20π rad/sec. The voltage constant, k_e, was 0.098 v-s, which agreed well with the value computed in the previous section of 0.092 v-s.

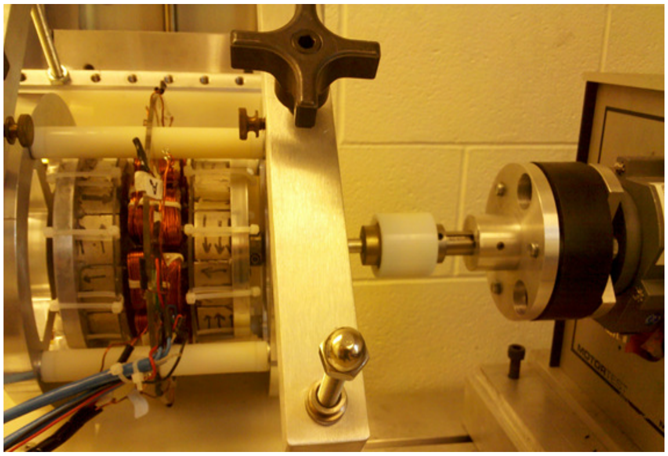

Figure 11. Ironless Motor Coupled to a Dynamometer on a Motor Test Stand

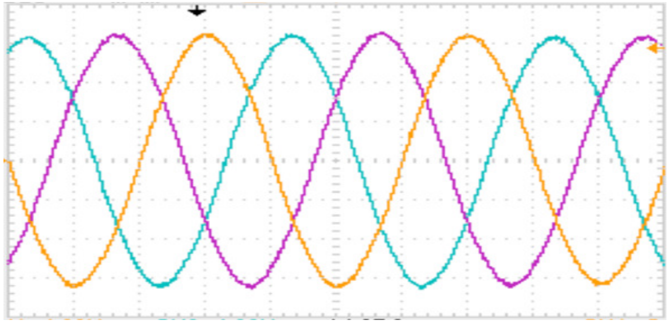

Figure 12. Back EMF Waveform (2 V/div, 25 ms/div)

The torque-versus-speed characteristic of the machine was obtained by placing the ironless machine on a dynamometer, while measuring shaft torque and RPM. For the tests, the stator current was limited to 10 A_{rms} per phase, due to thermal constraints. Likewise, the rotor speed was limited to 1200 RPM for several reasons: the DC bus voltage needed to be increased for higher speed, and the centrifugal force, F_c, on the magnets increased in proportion to speed squared, as given by Equation (16):

$$F_c = mr\omega^2 \qquad (16)$$

At 1200 RPM, approximately 13 lbs. of centrifugal force was acting on each magnet whose mass was 0.0975 kg. Until the adhesive used to bond the magnets to the disk was qualified for higher forces, rotational speed was limited to 1200 RPM. The obtained torque-versus-speed characteristic is shown in Figure 13. Note that the experimentally obtained torque is in good agreement with the expected value. For example, with the shaft angle at $\theta_m = 90°$ and the instantaneous phase currents of $i_a = 14.14$A, $i_b = -7.07$A, and $i_c = -7.07$A, the theoretical torque, from Equation (15), should be 5.85 N-m.

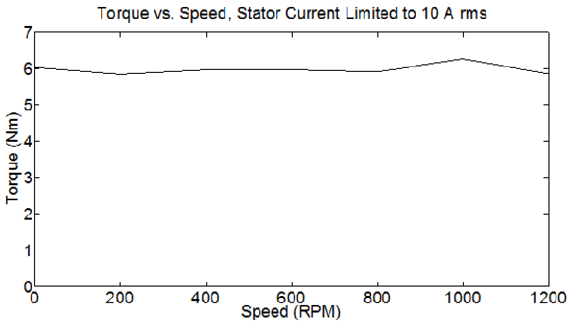

Figure 13. Torque versus Speed

Next, machine efficiency was experimentally determined for various operating points. In each case, the input (electrical) power was determined from measured phase voltages and currents. The output power was obtained from measured shaft torque and speed. For this experiment, a fan-type load was assumed, where load torque was proportional to the speed squared. The applied load torque versus speed curve used is shown in Figure 14. Efficiency versus speed results were above 90% over a wide range of speed, as shown in Figure 15.

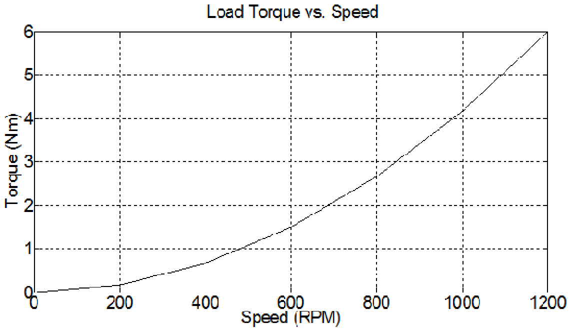

Figure 14. Load Torque versus Speed Characteristic used for Efficiency Tests

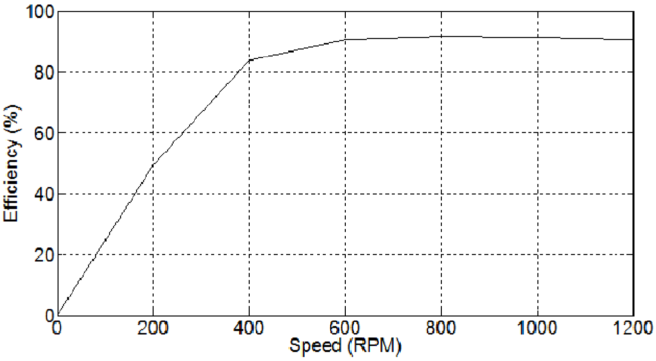

Figure 15. Ironless Machine Efficiency for Pump Load where Torque is Proportional to (Speed)^2

Efficiency tests reveal that the machine delivered one HP at 1200 RPM, as expected. Additional qualifications of the magnet adhesive may allow power rating increases by running the machine at higher speeds, without the core losses associated with iron-core machines. The total weight of the machine was 4.8 kg, which yielded a power-to-weight ratio of 156 W/kg. Comparisons to commercial machines of the same rating are difficult because the required data are only available from data sheets, and maximum versus short-time power ratings are not always clearly defined. Machines in the same power range with convection cooling must be used as comparisons because the specific power (W/kg) tends to increase with the machine power rating. For comparison, specifications from several vendors' iron-core PM machines in the range of one HP were examined. The specific power of those machines ranged from 64 W/kg up to 177 W/kg. Thus, the prototype ironless machine, even without serious consideration to weight reduction, compared well with those commercial iron-core machines.

The power density (power per unit volume) of the ironless design was also compared to the commercial iron-core machines. The ironless machine was found to have a power density of 505 kW/m^3. The commercial iron core machines that were examined had power densities ranging from a low of 375 kW/m^3 to 525 kW/m^3. Thus, the power density of the ironless machine compared well with those commercial machines.

Conclusions

The design of an ironless axial flux electric machine was presented. The design was carried out starting with basic design goals and constraints, and by using motor sizing estimates. For the rotor, a Halbach magnet array was used to concentrate flux in the air gap of the machine. This choice enabled reasonable magnetic loading, even in the absence of an iron core, while maintaining sufficient air gap length for aggressive electrical loading. The proposed machine design was then constructed and tested, with results showing excellent efficiency of well over 90% across a large operating range. The proposed design was also shown to be on par with many commercially designed machines of the same power rating in terms of power density and specific power rating. With additional attention to the magnet bonding to the rotor disc, the rated machine speed (and therefore power) can be increased to further improve power density without incurring additional inefficiencies that are unavoidable with iron-core designs. The results suggested that the ironless machine is easily manufactured, and is a viable alternative to iron-core designs—especially in applications where high speed, high efficiency, and low cogging torque are essential.

References

[1] Profumo, F., Eastham, F. J., Tenconi, A., & Gianolio, G. (2002). Plastic Electric Motors: A Viable Solution for Axial Flux Machines. *Proceedings of the 2002 IEEE International Symposium on Industrial Electronics*, (pp. 1-10).

[2] Lovatt, H. C., Ramsden, V. S., & Mecrow, B. C. (1997). Design of an In-Wheel Motor for a Solar-Powered Electric Vehicle. *Eighth International Conference on Electrical Machines and Drives*, (pp. 234-238).

[3] Kamper, M. J., Wang, R.-J., & Rossouw, F. G. (2008). Analysis and Performance of Axial Flux Permanent-Magnet with Air-Cored Non-Overlapping Concentrated Stator Windings. *IEEE Transactions on Industry Applications, 44*(5), 1495–1504.

[4] Gieras, J. F., & Gieras, I. A. (2002). Performance Analysis of a Coreless Permanent Magnet Brushless Motor. *Conference Record of the 37th IAS Annual Meeting, Industry Applications Conference*, (pp. 2477-2485).

[5] Praveen, R. P., Ravichandran, M. H., Achari, V. T. S., Raj, V. P. J., Madhu, G., & Bindu, G. R. (2010). Design and Analysis of Zero Cogging Brushless DC Motor for Spacecraft Applications. *International Conference on Electrical Engineering/Electronics Computer Telecommunications and Information Technology*, (pp. 254-258).

[6] Winter, O., Ucsnik, S., Rudolph, M., Kral, C., & Schmidt, E. (2012). Ironless In-Wheel Hub Motor Design by using Multi-Domain Finite Element Analyses. *International Symposium on Power Electronics, Electrical Drives, Automation and Motion*, (pp. 1474 -1478).

[7] Colotti, A., Garcia, O., Ronner, B., & Reichart, K. (1998). Design of an Ironless PMSM for Flywheel Storage Systems. *International Conference on Electric Machines*, (pp. 1128-1133).

[8] Ren, X., & Wang, Z. (2003). Multi-Stage PM Disc Motor for Ship Propulsion Application. *Sixth International Conference on Electrical Machines and Systems,* (pp. 52-55).

[9] Stamenkovic, I., Milivojevic, N., Krishnamurthy, M., Schofield, N., & Emadi, A. (2009). Ironless Machine Design and Novel Digital Control for Automotive Applications. *IEEE Vehicle Power and Propulsion Conference,* (pp. 475-480).

[10] Al Zaher, R., de Groot, S., Polinder, H., & Wieringa, P. (2010). Comparison of an Axial Flux and a Radial Flux Permanent Magnet Motor for Solar Race Cars. *International Conference on Electrical Machines*, (pp. 1-6).

[11] De, S., Rajne, M., Poosapati, M., Patel, C., & Gopakumar, K. (2012). Low-Inductance Axial Flux BLDC Motor Drive for More Electric Aircraft. *IET Power Electronics Journal*, *5*(1), 124-133.

[12] Bumby, J. R., & Marting, R. (2005). Axial-Flux Permanent-Magnet Air-cored Generator for Small-scale Wind Turbines. *IEEE Proceedings on Electric Power Applications, 152*(5), 1065-1075.

[13] Kessinger, R. L., & Robinson, S. (1997). SEMA-Based Permanent Magnet Motors for High-Torque, High-Performance. *Proceedings of the Naval Symposium on Electric Machines Conference*, (pp. 151-155).

[14] Batzel, T. D., & Adams, K. (2013). Variable Timing Control for ARCP Voltage Source Inverters Operating at Low DC Voltage. *International Journal of Modern Engineering*, *13*(2), 1-8.

[15] Price, G. F., Batzel, T. D., Muller, B. A., & Comanescu, M. U. (2009). Design and Testing of a Permanent Magnet Axial Flux Wind Power Generator. *International Journal of Modern Engineering*, *9*(2).

[16] Zhang, Z., Profumo, F., & Tenconi, A. (1996). Axial-Flux versus Radial-Flux Permanent-Magnet Motors. *Electromotion, 3*, 134-140.

[17] Sitapati, K., & Krishnan, K. (2001). Performance Comparisons of Radial and Axial Field, Permanent Magnet, Brushless Machines. *IEEE Transactions on Industry Applications, 37*(5), 1219-1226.

[18] Patterson, D. J., Brice, C. W., Dougal, R. A., & Kovuri, D. (2003). The “Goodness” of Small Contemporary Permanent Magnet Electric Machines. *IEEE International Electric Machines and Drives Conference*, (pp. 1195-2000).

[19] Ofori-Tenkorrang, J., & Lang, J. H. (1995). A Comparative Analysis of Torque Production in Halbach and Conventional Surface-Mounted Permanent Magnet Synchronous Motors. *Conference Record of the IEEE Industry Applications Conference*, *Thirtieth IAS Annual Meeting*, (pp. 657-663).

[20] Campbell, P. (1974). Principle of a Permanent Magnet Axial Field DC Machine. *Proceedings of the Institute of Electrical Engineering, 121*(12), 1489-1494.

[21] Patterson, D. J., Colton, J. L., Mularcik, B., Kennedy, B. J., Camilleri, S., & Rohoza, R. (2009). A Comparison of Radial and Axial Flux Structures in Electrical Machines. *IEEE International Electric Machines and Drives Conference*, (pp. 1029-1035).

[22] Huang, S., Luo, J., Leonardi, F., & Lipo, T. A. (1999). A Comparison of Power Density for Axial Flux Machines Based on General Purpose Sizing Equations. *IEEE Transactions on Energy Conversion, 14*(2), 185-192.

[23] West, J. G. (1993). DC, Induction, Reluctance and PM Motors for Electric Vehicles. *IEE Power Division Colloquium on Motors and Drives for Battery Powered Propulsion*, (pp. 1/1-111).

[24] Miller, T. J. E. (2006). *Speed’s Electric Motors: An Outline of Some of the Theory in the Speed Software for Electric Machine Design*. Lebanon, OH: Magna Physic Publishing.

[25] Winter, O., Kral, C., & Schmidt, E. (2012). Design Study of Magnet Shapes for Axial Halbach Arrays using 3D Finite Element Analyses. *IEEE International Conference on Electric Machines*, (pp. 2660-2665).

Biographies

TODD D. BATZEL received a B.S. in electrical engineering from Pennsylvania State University in 1984; an M.S. in electrical engineering from the University of Pittsburgh in 1989; and, a Ph.D. in electrical engineering in 2000 from Pennsylvania State University. He is currently an Associate Professor of electrical engineering at Penn State Altoona. His research interests include machine controls, electric drives, and artificial intelligence. Dr. Batzel may be reached at tdb120@psu.edu

ANDREW M. SKRABA is currently a fourth-year student in the electro-mechanical engineering technology program at Penn State Altoona.

RAY D. MASSI is currently a third-year student in the electro-mechanical engineering technology program at Penn State Altoona.

GASIFICATION OF TWO UNTAPPED RESOURCES: EL-LAJJUN OIL SHALE AND MUNICIPAL SOLID WASTE

Idowu Adeyemi, Masdar Institute, Abu Dhabi, UAE; Isam Janajreh, Masdar Institute, Abu Dhabi, UAE

Abstract

In this study, a numerical model for the gasification of El-Lajjun oil shale and municipal solid waste (MSW) inside an air-fed atmospheric gasifier was developed. The fuels were first characterized at the Waste-2-Energy Lab at the Masdar Institute with a thermo-gravimetric analyzer (TGA) for the proximate analysis, a Flash 2000 for the ultimate analysis, and a bomb calorimeter (Parr 6100) for the determination of the heating value. The model was based on the Langrangian -Eulerian approach, whereby the solid phase particles are tracked with the Langrangian approach and the surrounding gas phase is tracked by the Eulerian phase. The model takes into account the turbulent flow for the continuous phase (SST k-ω model), gas phase gasification (species transport model), devolatilization (Kobayashi two-competing-rate model), heterogeneous char reaction (multiple surface reaction model), particle dispersion by turbulent flow (stochastic discrete random walk model), radiation (P1), and particle distribution (Rosin-Rammler model).

The variations in the mole fraction of the product gas and temperature along the centerline of the gasifier were studied. While the mole fraction of carbon dioxide and water were reduced along the centerline with increasing residence time, the mole fraction of the carbon monoxide and hydrogen rose along the centerline of the gasifier for both cases. Based on this study, the oil shale was shown to have an ash content of 60.88%, which showed that it may require a low-cost separation process of the ash and moisture from the feedstock, or tapping into the sensible heat of the ash for it to be competitive for gasification.

Introduction

There are two major feed stocks that are not well utilized and sometimes cause problems in the world today. On the one hand, huge amounts of generated municipal solid wastes (MSW) are destined to be dumped into landfills worldwide. For example, over five million tons of solid waste were generated in Abu Dhabi in 2009 alone [1]. These solid wastes often end up in landfills, which cause countless problems. Landfills generate landfill gases (LFG), which have a global warming potential (GWP) of almost 21 times that of carbon dioxide. Apart from this, landfills occupy space which could be utilized for other purposes and harbor dangerous animals and disease-causing agents. On the other hand, there are large reserves of oil shale, which total about 790 billion cubic meters worldwide [2]. The Green River deposits in the western part of U.S., the Tertiary deposits in Australia, and the El-Lajjun deposits in Jordan are some parts of the world deposits that generate several million barrels of oil shale. These two feed stocks can be converted into synthetic gases of high economic value through their oxidation with a limited amount of oxidant through a pathway known as gasification.

Some studies have looked at the gasification effects on oil shale and MSW [3]. Jaber [3] studied the effects of bed temperature and fluidizing gas type on the gas composition, quantity, and calorific value of the syngas during the gasification of El-Lajjun oil shale samples in a continuous-feed fluidized bed reactor. In another study, Jaber et al. [4] investigated the influence of temperature on the gasification of oil shale in a continuous-feed fluidized bed reactor, using carbon dioxide as the fluidizing gas. Ingel et al. [5] studied the use of concentrated solar energy for gasifying oil shale with the Solar Central Receiver at the Weizmann Institute of Science. Xiao et al. [6] investigated the gasification characteristics of MSW in a fluidized bed gasifier at temperatures between 550-700°C. Thereafter, the melting characteristics of the fly ash generated was conducted within 1100-1460°C in a fixed-bed furnace. Wang et al. [7] studied the steam gasification of MSW with NiO on modified dolomite (NiO/MD) catalyst in order to obtain a hydrogen rich synthetic gas.

The objective of this current study was to investigate the entrained flow gasification behavior of El-Lajjun oil shale and MSW using ANSYS Fluent. The gasification numerical model was based on the drop-tube experimental facility at the Masdar Institute. The investigation started with the material characterization of the feed stocks in order to determine their suitability for gasification and provide essential data for the numerical model. The numerical model was based on the Lagrangian-Eulerian scheme. The model takes into account the turbulent flow for the continuous phase (Realizable k-ε model), gas-phase gasification (species transport model), devolatilization (Kobayashi two-competing-rate model), heterogeneous char reaction (multiple surface reaction model), particle dispersion by turbulent flow (Stochastic discrete random walk model), radiation (P1), and particle distribution (Rosin-Rammler model). The developed model will aid in determining specific characteristics of each feedstock under the same conditions.

Material Characterization

Proximate Analysis

The thermo-gravimetric or proximate analysis is an essential tool in the gasification process which helps to break down the feedstock into moisture, volatile, fixed carbon, and ash. The decomposition process was conducted with a DSC/TGA Q600 thermal analyzer. These data (see Figures 1 and 2, and Table 1) are required in order to model the gasification process.

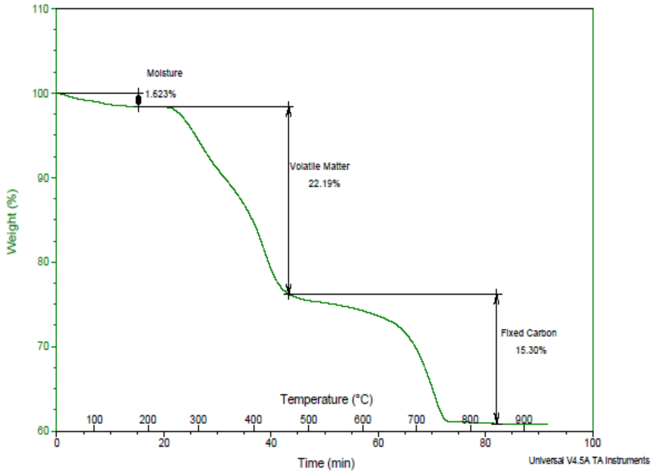

Figure 1. The Proximate Analysis of the El-Lajjun Oil Shale

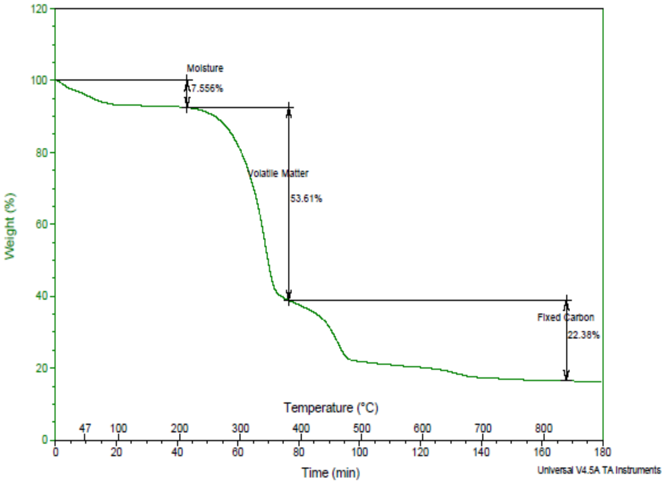

Figure 2. The Proximate Analysis of the MSW

Table 1. The Proximate Analysis of El-Lajjun Oil Shale and Municipal Solid Waste

Proximate Analysis	El-Lajjun Oil Shale (Wt. %)	Municipal Solid Waste (Wt. %)
Moisture	1.62	7.56
Volatile	22.19	53.61
Fixed Carbon	15.30	22.38
Ash	60.88	16.45

Ultimate Analysis

The ultimate analysis is based on the determination of the elemental composition of the fuel. The elemental composition of any carbonaceous material—in terms of the mass percentages of C, H, O, N, S components—can be determined using FLASH Elemental Analyzer. Determination of the elemental content composition is very important in gasification as it helps to determine the equivalence ratio of the fuel. The ultimate analysis data for the feed stocks are given in Table 2.

Table 2. The Ultimate Analysis of El-Lajjun Oil Shale and Municipal Solid Waste

Ultimate Analysis	El-Lajjun Oil Shale (Wt. %)	Municipal Solid Waste (Wt. %)
Carbon	19.17	45.32
Hydrogen	1.96	5.68
Nitrogen	0.39	1.14
Oxygen	14.41	31.13
Sulfur	3.19	0.28
Ash	60.88	16.45

Bomb Calorimetry

The bomb calorimeter helps to determine the heating value of the feed stocks to be gasified. The equipment used for this analysis was the Parr 6100 bomb calorimeter. The heating value obtained for the El-Lajjun oil shale and MSW were 7.82 MJ/kg and 17.57 MJ/kg, respectively.

Model Development

The assumption of instantaneous equilibrium and equal diffusivity may be too generic for numerical solid feedstock conversion under gasification conditions. Hence, the numerical investigation for this gasification study was based on global reaction kinetics in order to more accurately describe the multi-physics, multi-scale, multi-phase model. The gasification process, which is based on the Langrangian-Eulerian approach—used in this current study, due to the low-volume loading in EFGs—is modeled with the consideration of four events. The Langrangian-Eulerian approach tracks the particles as they move in space and takes the gas phase as the whole control volume. As the particles are injected into the gasifier, residual moisture content in the feedstock is evaporated during passive heating. The volatile content is then released in a process known as devolatilization or pyrolysis. The volatiles and other gaseous species then undergo homogeneous reactions, but the char is consumed through heterogeneous reactions. While the particles were monitored over space, the continuum approach was used for the gas phase. The multi-physics, multi-scale model was developed to describe the details of the different physical and chemical processes occurring in the Drop Tube Reactor (DTR) through key sub-models and their coupling. The mesh structure was developed with the GAMBIT meshing tool (see Figure 3).

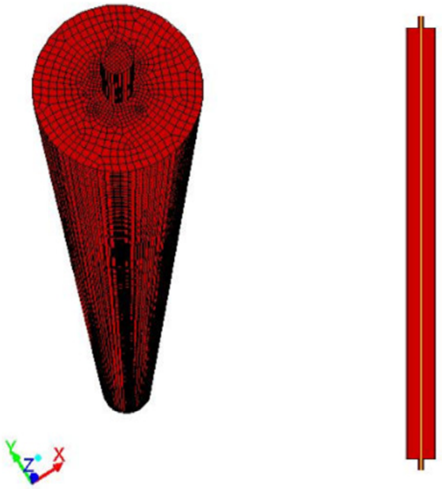

Figure 3. The 2D and 3D Mesh Structure

The numerical model is based on the drop-tube experimental facility at the Masdar Institute (see Figure 4). The specifications of the drop tube are listed in Table 3.

Governing System of Equations

Gas phase: The fluid phase was modeled with the Eulerian concept, where a control volume, the DTR, was being monitored. The conservation of mass, momentum, energy, and species were ensured and are, respectively, written as shown in Equations (1)-(3):

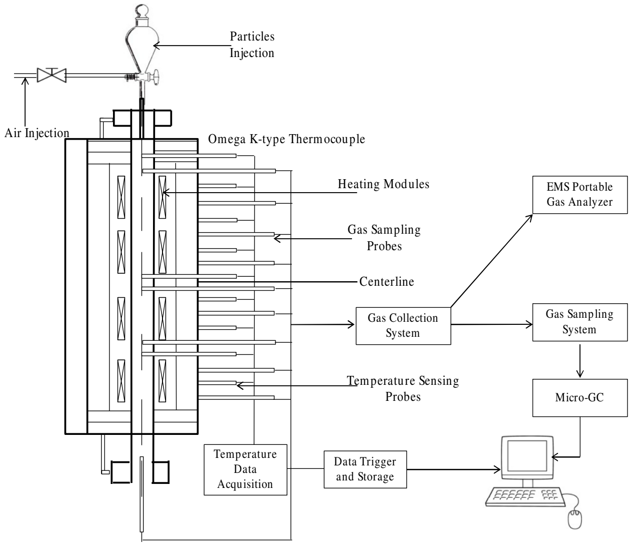

Figure 4. Schematic Representation of the Drop-tube Experimental Setup

Table 3. Drop-tube Specifications

Parameter	Value
Length Tube B	1540 mm
Outer Diameter Tube B	75 mm
Inner Diameter Tube B	66 mm
Heated Length	750 mm
Power Rating	4.6 kW
Material Tube B	APM
Maximum Temperature	1400 K

$$\frac{\partial}{\partial x_i}(\rho u_i) = S_{p,m} \tag{1}$$

$$\frac{\partial}{\partial x_j}(\rho u_i u_j) = -\frac{\partial p}{\partial x_i} + \frac{\partial}{\partial x_j}\left[\mu\left(\frac{\partial u_i}{\partial x_j} + \frac{\partial u_j}{\partial x_i} - \frac{2}{3}\delta_{ij}\frac{\partial u_l}{\partial x_l}\right)\right] + \frac{\partial}{\partial x_j}\left(-\rho\overline{u_i' u_j'}\right) + S_{p,mom} \tag{2}$$

$$\frac{\partial}{\partial x_i}(\rho u_i h) = \frac{\partial}{\partial x_i}\left[\lambda \frac{\partial T}{\partial x_i}\right] + S_{rad} + S_h + S_{p,h} \tag{3}$$

where, ρ is the medium density, u_i are the velocity components, and $S_{p,m}$ is the mass source term. P is the static pressure, μ is the molecular viscosity, δ_{ij} is kronecker delta tensor, and $S_{p,mom}$ is the momentum source term. Also, h is the enthalpy, λ is the medium thermal conductivity, S_{rad} is the radiative heat source, and $S_{p,h}$ is the energy heat source.

The multiple-species distribution was evaluated according to the species transport equation, which is given in Equation (4):

$$\frac{\partial}{\partial x_i}(\rho u_i Y_i) = \frac{\partial}{\partial x_i}(\rho D Y_i) + S_{Yi} + S_{p,Yi} \tag{4}$$

where, Y_i is the mass fraction of species i, and D is the diffusion coefficient, which is typically described according to Vick's law. S_{Yi} is the source term, due to the destruction and elimination of species, i, due to the reaction, while $S_{p,Yi}$ is the species source term, due to their interaction. As the flow was characterized as turbulent flow regime, the k-ω eddy viscosity model was used for the modeling of additional Reynolds stress according to Equation (4), as this is a commonly used model when treating an axisymmetrical flow. The Reynolds stress is modeled according to the eddy viscosity model, μ_t, and is described by Equations (5) and (6):

$$-\rho\overline{u_i{}'u_j{}'} = \mu_t\left(\frac{\partial u_i}{\partial x_j} + \frac{\partial u_j}{\partial x_i}\right) - \frac{2}{3}\delta_{ij}\left(\rho k + \mu_t\frac{\partial u_l}{\partial x_l}\right) \tag{5}$$

$$\mu_t = \alpha^*\frac{\rho k}{\omega} \tag{6}$$

where, μ_t, is the eddy viscosity, k is the turbulent kinetic energy, and ω is the specific dissipation scalar. The material transport for k and ω is given in Equations (7) and (8):

$$\frac{\partial}{\partial x_i}(\rho k u_i) = \frac{\partial}{\partial x_j}\left[\left(\mu + \frac{\mu_t}{\sigma_k}\right)\frac{\partial k}{\partial x_j}\right] + G_k - Y_k + S_k \tag{7}$$

$$\frac{\partial}{\partial x_i}(\rho\omega u_i) = \frac{\partial}{\partial x_j}\left[\left(\mu + \frac{\mu_t}{\sigma_\omega}\right)\frac{\partial \omega}{\partial x_j}\right] + G_\omega - Y_\omega + D_\omega + S_\omega \tag{8}$$

where, G, Y, and S are the production, the dissipation, and the source terms of each K and ω corresponding to their subscripts k and ω, respectively.

The closure problem for the Reynolds stresses in the momentum equation was solved according to Equation (5), and the gas phase turbulence was modeled with the k-ω shear stress transport model, as represented in Equations (6)-(8). The kinetics for the homogeneous reactions and their chemical equations are described in Table 4.

Particle Phase: In this model, and for entrained flow gasifiers in general, the discrete Lagrangian frame of reference was used to track each spherical particle of diameter distribution given by the Rosin-Rammler model. This approach is valid since its fundamental loading assumption is that the volume fraction of the solid phase must be less than 10% [10]. The conservation of mass, momentum, and energy of the particles are given in Equations (9)-(15), respectively.

$$\frac{dm_p}{dt} = \frac{dm_{C-O_2}}{dt} + \frac{dm_{C-CO_2}}{dt} + \frac{dm_{C-H_2O}}{dt} + \frac{dm_{pyrolysis}}{dt} + \frac{dm_{vapor}}{dt} \tag{9}$$

where, m_p is the particle mass and m_x is the x mass portion of oxygen (x≡o_2), carbon dioxide (x≡Co_2), moisture (x≡H_2O), volatile (x≡volatile), and light aromatics (x≡vapor). The momentum is written as:

$$\frac{du_p}{dt} = F_D(u - u_p) + \frac{g_i(\rho_p - \rho)}{\rho_p} + F_i \tag{10}$$

where, the drag force is related to the drag coefficient, which is written according to Equation (10):

$$F_D = \frac{18\mu}{\rho_p {d_p}^2}\frac{C_D Re_p}{24} \tag{11}$$

where, the subscript p signifies the solid particles, and ρ, d, and Re denote the particle's density, diameter, and the following Reynolds number. The C_D is the drag coefficient and is expressed by the functional form of Equation (12):

$$C_D = a_1 + \frac{a_2}{Re_p} + \frac{a_3}{{Re_p}^2} \tag{12}$$

Table 4. Kinetic Data for the Homogeneous Reactions [8], [9]

Reaction	Activation Energy (E_a)	Pre-Exponential Factor (A)	N
$CH_4 + \frac{1}{2}O_2 \rightarrow CO + 2H_2$	1.25×10^8	4.4×10^{11}	0
$H_2 + \frac{1}{2}O_2 \rightarrow H_2O$	1.67×10^8	6.8×10^{15}	-1
$CO + \frac{1}{2}O_2 \rightarrow CO_2$	1.67×10^8	2.24×10^{12}	0
$CH_4 + H_2O \rightarrow CO + 3H_2$	1.25×10^8	3×10^8	0
$CO + H_2O \rightarrow CO_2 + H_2$	8.37×10^7	2.75×10^9	0

Energy is determined using Equation (13):

$$Q_G = \frac{dm_{C-O_2}}{dt} H_{C-O_2} + \frac{dm_{C-CO_2}}{dt} H_{C-CO_2} + \frac{dm_{C-H_2O}}{dt} H_{C-H_2O} \quad (13)$$

where, H_i is the corresponding enthalpy of formation of each the species, i. Using the basic definition of the enthalpy ($h=C_p\,T$), Equation (11) can be re-written as:

$$m_p c_p \frac{dT_p}{dt} = h_p A_o\left(T - T_p\right) + \frac{\varepsilon_p A_o}{4}\left(G - 4\sigma T_p{}^4\right) + Q_G \quad (14)$$

where, Cp is the constant pressure specific heat, h is the convective heat transfer coefficient, E is the particle emissivity, A is the particle surface area, and σ is Stephan's constant. The convective heat coefficient is related to the conductive coefficient through a Nusselt number which is given in Equation (15):

$$Nu = \frac{h_p d_p}{k_g} = 2.0 + 0.6 Re_p Pr^{\frac{1}{3}} \quad (15)$$

where, k is the medium conductivity and Pr is the prandtle number. The char gasification process consists of three reactions: char-O_2, char-CO_2, and char-H_2O. The first reaction is exothermic and releases heat into the reactor. However, the last two reactions are endothermic and require a lot of heat for them to proceed, as noticed in their activation energy values in Table 5.

Results and Discussions

Model Validation

The validity of the results of every point on the contour depends mainly on the rigor of the constraint for the validation of the experimental data. The more the model results agree with the experimental values, the higher the fidelity in the model. Hence, the numerical model was validated with experimental data obtained from the drop-tube experimental setup at the Masdar Institute. The model results predict the experimental values reasonably well under both non-reactive and reactive conditions, as depicted in Figures 5 and 6. The experimental values were obtained with the drop -tube facility at the Masdar Institute.

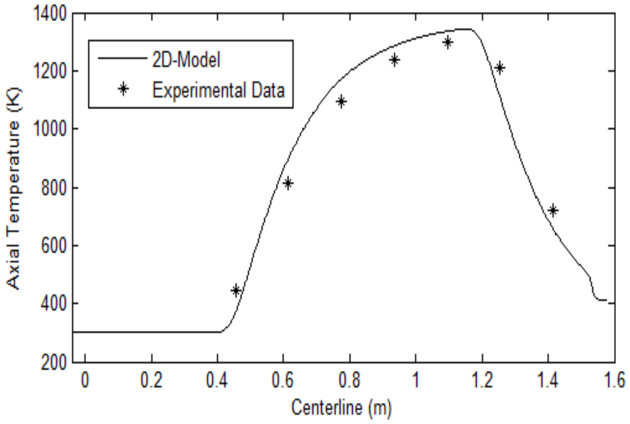

Figure 5. Axial Temperature Validation with Experimental Data for Non-reactive Flow

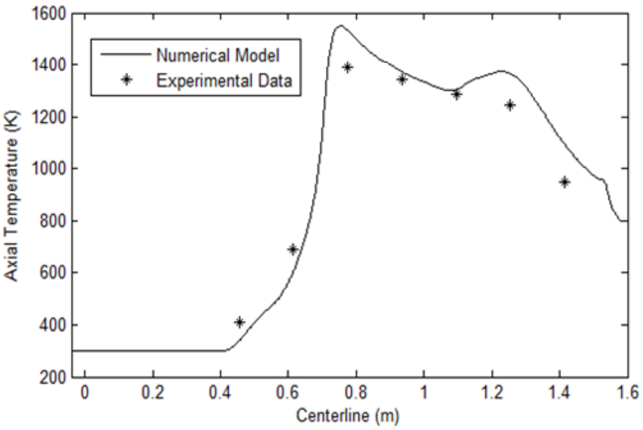

Figure 6. Axial Temperature Validation with Experimental Data for Reactive Flow

Table 5. Kinetic Data for the Heterogeneous Reactions [11]

Reaction	Activation Energy, E_a (J/mol)	Pre-Exponential Factor (A)	N
$C + \frac{1}{2}O_2 \rightarrow CO$	9.23 x 10^7	2.3	1
$C + CO_2 \rightarrow 2CO$	1.62 x 10^8	4.4	1
$C + H_2O \rightarrow CO + H_2$	1.47 x 10^8	1.33	1

Effect of Gasification of Oil Shale and MSW

One of the most important issues regarding the use of gasification is its fuel flexibility capability. Hence, this study was conducted in order to observe the behavior of entrained flow gasifiers to oil shale and MSW. The contour profile of the temperature (see Figure 7) showed that the temperature in the gasifier during the conversion of the MSW was generally higher than that of the oil shale. This was due to the higher volatile content in the MSW. Volatile matter is known to undergo exothermic reactions, which generates a lot of heat.

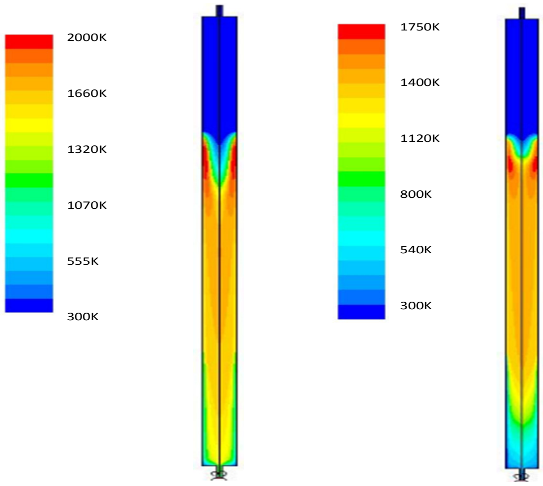

Figure 7. Contour Profile of the Temperature of MSW (left) and Oil Shale (right)

The mole fraction of the oxidant along the gasifier confirmed that the reactor was under gasification conditions (see Figure 8). The mole fraction of the oxidant along the gasifier showed that the oxygen content finished along the reactor for both feed stocks. However, the oxidant finished earlier for the oil shale. This can be accounted for by the lower oxygen content in the oil shale.

The mole fraction of the volatile (see Figure 9) showed that more volatile matter was released for the MSW than for the oil shale. This was evident from the fact that MSW (53.61%) contains more volatile than oil shale (22.19%).

Conclusions

El-Lajjun oil shale and MSW were analyzed for their material characteristics at the Waste-2-Energy Lab at the Masdar Institute. The results showed that El-Lajjun oil shale has high quantity ash (60.88%) and oxygen (14.41%), which in turn affected its gasification behavior. However, the MSW yielded a lower amount of ash (16.45%), while producing more volatile matter (53.61%) and oxygen (31.13%). A predictive model was developed for the gasification of El-Lajjun oil shale and MSW. The model was validated with MI drop-tube experimental data. This model allowed for the observation of specific gasification behaviors of each of the feed stocks. Based on this study, the oil shale was shown to have an ash content of 60.88%, which implies that it may require a low-cost separation process of the ash and moisture from the feedstock, or tapping into the sensible heat of the ash, for it to be competitive for gasification. Future studies should involve the utilization of a large eddy simulation to study the gasification of these two feed stocks. With a large eddy simulation, the turbulence can be more appropriately captured. In addition, the effect of ash minerals on the gasification of high-ash feed stocks should be studied.

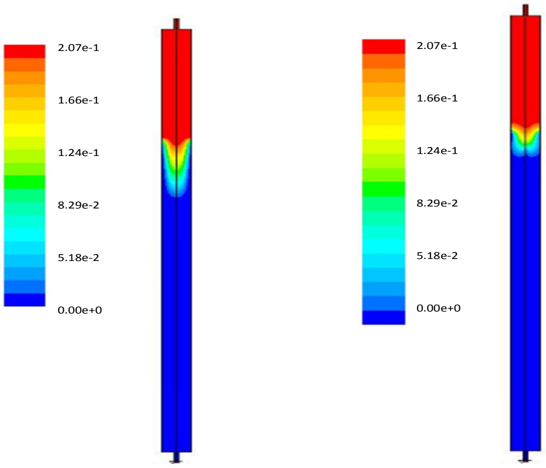

Figure 8. Contour Profile of the Oxygen Mole Fraction of MSW (left) and Oil Shale (right)

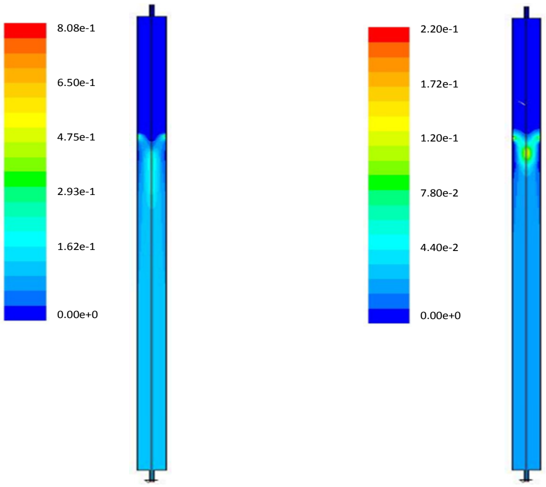

Figure 9. Contour Profile of the Volatile Mole Fraction of MSW (left) and Oil Shale (right)

Acknowledgements

The authors acknowledge the support and sponsorship of the Masdar Institute and the members of the Waste-2-Energy group.

References

[1] Statistics Center - Abu Dhabi. (2011). *Waste Statistics in the Emirate of Abu Dhabi 2009*. Retrieved December 12, 2013, from http://www.scad.ae/SCADDocuments/Waste%20Statistics%20in%20the%20Emirate%20of%20Abu%20Dhabi%202009.pdf

[2] International Energy Agency. (2012). *World Energy Outlook 2012*. Retrieved December 12, 2013, from http://www.iea.org/publications/freepublications/publication/world-energy-outlook-2012.html

[3] Jaber, J. O. (2012). Gasification Potential of Ellujjun Oil Shale. *Energy Conversion and Management*, *41* (15), 1615-1624.

[4] Jaber, J. O., Probert, S. D., Williams, P. T., & Tahat, M. (2000). Gasification Potential and Kinetics of Jordanian Oil Shales Using CO2 as the Reactant Gas. *Energy Sources*, *22*(6), 573-585.

[5] Ingel, G., Levy, M., & Gordon, J. (1991). Gasification of Oil Shales by Solar Energy. *Solar Energy Materials*, *24*(1-4), 478-489.

[6] Xiao, G., Jin, B.-S., Zhong, Z.-P., Chi, Y., Ni, M.-J., Cen, K.-F., et al. (2007). Experimental Study on MSW Gasification and Melting Technology. *Journal of Environmental Sciences*, *19*(11), 1398-1403.

[7] Wang, J., Cheng, G., You, Y., Xiao, B., Liu, S., He, P., et al. (2012). Hydrogen-Rich Gas Production by Steam Gasification of Municipal Solid Waste (MSW) using NiO Supported on Modified Dolomite. *International Journal of Hydrogen Energy*, *37* (8), 6503-6510.

[8] Jones, W. P., & Lindstedt, R. P. (1988). Global Reaction Schemes for Hydrocarbon Combustion. *Combustion and Flame*, *73*(3), 233-249.

[9] Westbrook, C. K., & Dryer, F. L. (1981). Simplified Reaction Mechanisms for the Oxidation of Hydrocarbon Fuels in Flames. *Combustion Science and Technology*, *27*(1-2), 31-43.

[10] Abani, N., & Ghoniem, A. F. (2013). Large Eddy Simulations of Coal Gasification in an Entrained Flow Gasifier. *Fuel*, *104*, 664–680.

[11] Kajitani, S., Hara, S., & Matsuda, H. (2002). Gasification Rate Analysis of Coal Chars with a Pressurized Drop Tube Furnace. *Fuel, 81*(5), 539-546.

Biographies

IDOWU ADEYEMI is currently a Ph.D. candidate at the Masdar Institute. He earned his M.S. in Mechanical Engineering, 2014, from the Masdar Institute. Idowu is part of the waste management group with Dr. Janajreh and is well-versed in both experimental and simulation analyses of feedstock gasification. Mr. Idowu may be reached at iadeyemi@masdar.ac.ae

ISAM JANAJREH is currently an Associate Mechanical Engineering Professor and the director of the waste-to-energy lab at the Masdar Institute. He is an internationally recognized expert in the area of waste-to-energy, particularly in the feedstock characterization thermochemical pathways, including gasification and pyrolysis. He has authored more than 80 publications on the subject and appeared in over 80 conferences. Dr. Janajreh may be reached at ijanajreh@masdar.ac.ae

PERFORMANCE OF AN OPTIMAL CONTROLLER OF VSC-HVDC SYSTEMS IN WEAK NETWORKS

F. Safdarian, Amirkabir University of Technology (Tehran Polytechnic); M.M. Ardehali, Amirkabir University of Technology (Tehran Polytechnic); G.B. Gharehpetian, Amirkabir University of Technology (Tehran Polytechnic)

Abstract

In this study, optimal control of a voltage source converter—high-voltage direct-current (VSC-HVDC) transmission system was modeled and its performance in weak networks was compared with strong systems. The comparison was made considering how the system would track the desired values of DC voltage and AC current, while switching or faults occur in order to determine system stability. A proportional-integral (PI) controller with decoupled control variables of a typical generator-load VSC-HVDC system was proposed for optimal control. Simulation results showed that a fault caused by switching in weaker networks, in which the short-circuit level was lower than stable networks, led to higher changes in DC voltage and AC current.

Introduction

Recent developments in power delivery are influenced by the progress of conventional power production, which mainly use primary energy resources that are limited and cause environmental problems. The technology of high-voltage direct current (HVDC) transmission can be a solution to this problem [1], [2]. Supporters of HVDC technology contend that it has the following environmental and economic benefits [3]:

- Transferring larger amounts of energy, especially in undersea transmission. DC systems, as opposed to long AC systems, are free of the cable capacitance that limits the possible transmission distance.
- Reducing active power losses, as HVDC has lower transmission losses than AC systems, even regarding converter losses.
- Connecting asynchronous systems, particularly systems with different nominal frequencies.
- Controlling all DC and AC parameters with acceptable accuracy and speed. Moreover, constant power can be transferred and fluctuations would be damped contrary to the AC network.
- Decreasing short-circuit currents. HVDC systems, unlike AC systems, do not contribute to short-circuit currents.

The configuration of an HVDC network is determined according to the mode of converter and location of conversion stations. The main configurations are [3]:

- Point-to-point HVDC transmission: uses overhead lines or submarine cables to connect to converter stations. The ground is used as a return path.
- Back-to-back HVDC stations: the two converters are located in the same station and are used to connect two asynchronous AC systems.
- Multi-terminal HVDC system: more than two converter stations are included.

Therefore, HVDC systems have drawn a lot of attention because of their advantages over HVAC transmission, including environmental, technical, and economical merits. Weak networks have lower short-circuit levels and a relatively high electrical impedance, but a lower inductance-to-impedance ratio in comparison with strong systems. HVDC converters connected to weak AC networks suffer from stability problems, due to adverse DC-AC system interactions. VSC-HVDC systems feature independent active and reactive power regulation and black-start capability and can provide connection between weak AC networks, in contrast to conventional thyristor-based HVDC transmissions. Although one of the original purposes for the use of VSC-HVDC systems was the possibility to connect to very weak AC systems, some difficulties have been experienced [4-7].

Some transmission systems use a line commutated converter (LCC) based on current source converter (CSC) through thyristor technology. The problem with this method is that thyristor turn off is not controlled with the gate signal [8]. Owing to the development of power electronics, voltage source converters (VSC) have become more practical. VSC-HVDC was invented by Ooi and Wang in 1990 [9] and uses self-commutating switches, which are gate-turn-off thyristors (GTOs) and insulated-gate bipolar transistors (IGBTs) that can be either turned on or off. Power electronics developments have given rise to HVDC Light, based on pulse width modulation (PWM) to produce voltage, independent of AC. Siemens has offered a VSC-HVDC variant, commercialized as HVDC Plus, which uses a multi-level approach. The first commercial VSC-based HVDC transmission was commissioned in 1999 on Gotland Island with an underground cable of 50 km. The topologies of power converters VSC in order to increase the transferred power are classified into three types: a two-level converter, a three-level converter, and a modular multilevel converter. The evolution of power electronics has led to progress on control techniques to improve VSC-HVDC system stability. The design of controllers for VSC-HVDC systems is mainly based on mathematical models.

However, the system will be influenced by external uncertainties such as the stochastic fluctuation of the faults in the AC system and the DC link. Hence, it is necessary to improve VSC-HVDC transient stability and to reduce the influences of uncertainties. In this way, many linear and nonlinear control strategies of VSC-HVDC systems have been developed, including a proportional-integral (PI) [10], [11] control Scheme [8], [12]. Conventional PI controllers, based on inner and outer control loops, are being widely studied. Modeling and optimal control of generator-load (GL) VSC-HVDC transmission systems, in order to enhance system stability, was designed by Ayari et al. [13] which aimed to compare transient stability of weak networks with strong systems. An optimal PI controller was simulated using MATLAB/Simulink and the desired values of DC voltage and AC current were tracked, while switching or faults occurred. The simulation took into account time constants and fault correction.

Modeling VSC-HVDC Systems

The typical system consists of a converter substation for the HVDC transmission system on the DC side and the AC network with impedance R1+jL1. Capacitor C1 on the DC side boosts the DC voltage in order to feed load R+jL. Figure 1 illustrates the structure of the system studied. As can be seen, it consists of an AC network and the DC side is connected through a converter in a rectifier mode. Applying Kirchhoff's theorem for the voltages on the AC side gives Equation (1) that depicts the voltage drop in each phase.

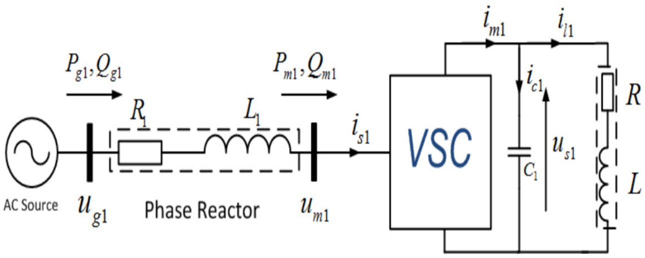

Figure 1. Basic Structure of a GL VSC-HVDC

$$L_1\frac{di_{s1}}{dt}+R_1 i_{s1}=u_{g1}-u_{m1} \tag{1}$$

The balanced three-phase system is defined in *d-q* reference by Equations (2)-(6):

$$\overrightarrow{u_{g1}}=u_{g1d}+ju_{g1q} \tag{2}$$

$$\overrightarrow{u_{m1}}=u_{m1d}+ju_{m1q} \tag{3}$$

$$\overrightarrow{i_{s1}}=I_{s1d}+jI_{s1q} \tag{4}$$

Moreover,

$$\overrightarrow{u_{m1}}=m_{1d}\frac{u_{s1}}{2}+jm_{1q}\frac{u_{s1}}{2} \tag{5}$$

So:

$$m_{1d}=2\frac{u_{m1d}}{u_{s1}}\ ,\ m_{1q}=2\frac{u_{m1q}}{u_{s1}} \tag{6}$$

where, m_{1d} and m_{1q} are the dimensionless *d-q* components that depict the relation between the *d-q* voltage on the AC side of the VSC-HVDC transmission system and the DC bus voltage, u_{s1}. The power exchange in the *d-q* reference voltage is given in Equation (7):

$$P_m=\frac{3}{2}(u_{m1d}i_{s1d}+u_{m1q}i_{s1q}) \tag{7}$$

Thus, by applying the power equality constraint on both sides of the rectifier, Equation (8) is achieved:

$$P_{mAC}=P_{mDC}\Rightarrow u_{s1}i_{m1}=\frac{3}{2}(u_{m1d}i_{s1d}+u_{m1q}i_{s1q}) \tag{8}$$

Considering Equations (1), (6) and (8), the continuous-time mathematical model of the VSC-HVDC system, which specifies the different relations among the circuit components, is indicated by the following state-space equations:

$$\frac{di_{s1d}}{dt}=-\frac{R_1}{L_1}i_{s1d}+\omega_1 i_{s1q}-\frac{1}{2L_1}m_{1d}u_{s1}+\frac{1}{L_1}u_{g1d} \tag{9}$$

$$\frac{di_{s1q}}{dt}=-\omega_1 i_{s1d}-\frac{R_1}{L_1}i_{s1q}-\frac{1}{2L_1}m_{1q}u_{s1}+\frac{1}{L_1}u_{g1q} \tag{10}$$

$$\frac{du_{s1}}{dt}=\frac{3}{4C_1}m_{1d}i_{s1d}+\frac{3}{4C_1}m_{1q}i_{s1q}-\frac{1}{C_1}i_{L1} \tag{11}$$

$$\frac{di_{L1}}{dt}=\frac{1}{L}u_{s1}-\frac{R}{L}i_{L1} \tag{12}$$

The active and reactive powers, applied to the AC side at the beginning and the end of the AC line, are given by P_{g1}, Q_{g1}, P_{m1}, and Q_{m1}, in Equations (13)-(16), respectively:

$$P_{g1} = \frac{3}{2}(u_{g1d} i_{s1d} + u_{g1q} i_{s1q}) \tag{13}$$

$$Q_{g1} = \frac{3}{2}(u_{g1q} i_{s1d} - u_{g1d} i_{s1q}) \tag{14}$$

$$P_{m1} = \frac{3}{2}(u_{m1d} i_{s1d} + u_{m1q} i_{s1q}) \tag{15}$$

$$Q_{m1} = \frac{3}{2}(u_{m1q} i_{s1d} - u_{m1d} i_{s1q}) \tag{16}$$

Optimal Control for VSC-HVDC

Control Problem Formulation

After modeling the steady state, it is necessary to maintain unity power factors on the AC side of the VSC-HVDC and govern the DC voltage. Hence, the control system, based on the inner current control loop, controls the AC current; the outer controllers supply the DC voltage to the desired values. For this purpose, optimal PI controllers were proposed in order to control the voltage on the VSC's AC side and the DC current. The optimal PI controller is given by the transfer function in Equation (17):

$$PI_i(s) = \frac{v}{e} = k_{pi} + \frac{k_{ii}}{s} \tag{17}$$

where, v and e refer to the output of the controller and the error between the reference and the under-control state variable, respectively. From Equation (17), the dynamics of the error can be written in the state-space Equation (18).

$$\overset{\bullet}{x}_e = A_e x_e + B_e v_i \quad \text{where,} \quad x_e = \begin{bmatrix} e_i \\ z_i \end{bmatrix} \tag{18}$$

The optimal parameters were obtained by minimizing a quadratic criteria J, from Equation (19):

$$J = \frac{1}{2}\int_0^{+\infty} (x_e^T Q x_e + v_i^T R v_i) dt \tag{19}$$

Equation (18), considering the criterion given by Equation (19), generates Equation (20):

$$v_i = -K_i x_e \tag{20}$$

where,

$$K_i = R^{-1} B_e^T S_i \tag{21}$$

where, S is a symmetric non-negative matrix that is the solution of the Riccati equation given in Equation (22):

$$S_i A_e + A_e^T S_i - S_i B_e R^{-1} B_e^T S_i + Q = 0 \tag{22}$$

By using LQR from MATLAB, the optimal gains of the PI controller are achieved as Equation (23):

$$K_i = [k_{pi}\ k_{ii}] \tag{23}$$

Optimal PI Controller

A method of VSC-HVDC control via PI controllers was studied. Based on this model, two control loops were obtained that had two controllers, PI_1 and PI_2. The inner loop regulates the AC currents i_{s1d} and i_{s1q}, and the outer loop controls the voltage u_{s1} on the DC side.

Inner Current Control Loop

From Equations (9)-(12), the variations of the AC current can be expressed by Equations (24)-(25):

$$\frac{di_{s1d}}{dt} = -\frac{R_1}{L_1} i_{s1d} + \frac{1}{L_1} u_{1d} \tag{24}$$

$$\frac{di_{s1q}}{dt} = -\frac{R_1}{L_1} i_{s1q} + \frac{1}{L_1} u_{1q} \tag{25}$$

where,

$$u_{1d} = \omega_1 L_1 i_{s1q} - \frac{1}{2} m_{1d} u_{s1} + u_{g1d} \tag{26}$$

$$u_{1q} = -\omega_1 L_1 i_{s1d} - \frac{1}{2} m_{1q} u_{s1} + u_{g1q} \tag{27}$$

Substituting i_{s1d} and i_{s1q}, by (I_{s1dref}-e_{1d}) and (I_{s1qref}- e_{1q}) in Equations (24) and (25), respectively, the variations of the errors e_{1d} and e_{1q} and their integrals, named z_{1d} and z_{1q}, are expressed by Equations (28)-(31), respectively:

$$\frac{de_{1d}}{dt} = -\frac{R_1}{L_1} e_{1d} + \frac{1}{L_1} v_{1d} \tag{28}$$

$$\frac{dz_{1d}}{dt} = e_{1d} \tag{29}$$

$$\frac{de_{1q}}{dt} = -\frac{R_1}{L_1}e_{1q} + \frac{1}{L_1}v_{1q} \quad (30)$$

$$\frac{dz_{1q}}{dt} = e_{1q} \quad (31)$$

where, the outputs of the *PI₁* controllers are given by Equations (32) and (33):

$$v_{1d} = R_1 I_{s1dref} - u_{1d} \quad (32)$$

$$v_{1q} = R_1 I_{s1qref} - u_{1q} \quad (33)$$

So, the control signals are achieved from Equations (34) and (35):

$$m_{1d} = \frac{2}{u_{s1}}(-u_{1d} + \omega_1 L_1 i_{s1q} + u_{g1d}) \quad (34)$$

$$m_{1q} = \frac{2}{u_{s1}}(-u_{1q} - \omega_1 L_1 i_{s1d} + u_{g1q}) \quad (35)$$

According to the proposed optimal approach and the decoupling control method, the current i_{s1d} control loop is illustrated in Figure 2.

The gains of the inner current control loops are obtained from the proposed optimal control approach, which guarantees fast operation of the inner loop in the desired settling time.

Outer Current Control Loop

From Equations (9)-(12), the variation of the DC voltage can be specified as Equation (36):

$$\frac{du_{s1}}{dt} = \frac{1}{C_1}i_{C1} \quad (36)$$

where, the output of the optimal *PI₂* controller is achieved from Equation (37):

$$i_{C1} = \frac{3}{4}m_{1d}i_{s1d} + \frac{3}{4}m_{1q}i_{s1q} - i_{L1} \quad (37)$$

Substituting u_{s1} with (U_{s1ref}- e_{1c}) into Equation (36), the variations of error e_{1c} and its integral z_{1c} would be as Equations (38) and (39), respectively:

$$\frac{de_{1c}}{dt} = -\frac{1}{C_1}i_{c1} \quad (38)$$

$$\frac{dz_{1c}}{dt} = e_{1c} \quad (39)$$

According to the state-space equations of Equations (38) and (39), the minimization of the quadratic criterion *J* results in the stability of the GL VSC-HVDC system. Hence, Equation (40) is obtained from Equation (37).

$$I_{s1dref} = \frac{4}{3m_{1d}}(-i_{c1} - 0.75m_{1q}i_{s1q} + i_{L1}) \quad (40)$$

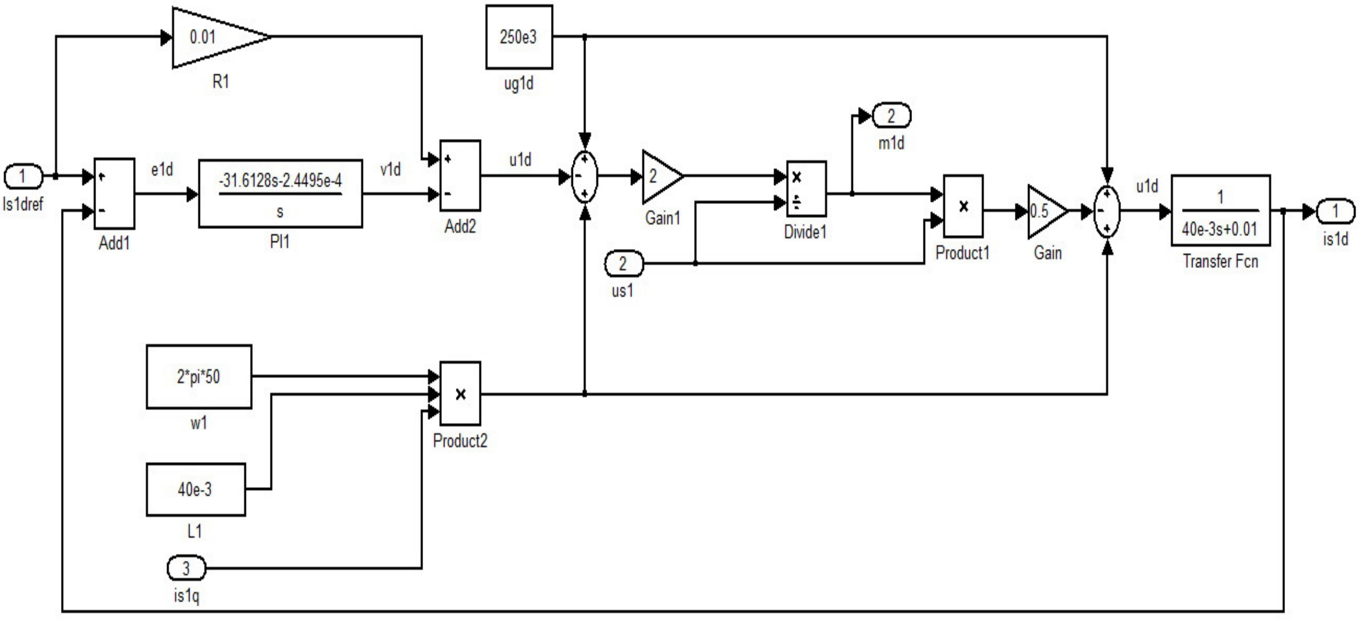

Figure 2. Outer Control Loop for AC Current, i_{s1d}

Consider that it can be divided by m_{1d} because this control variable would never become zero. Furthermore, the reactive power would be controlled through the current i_{s1q} using Equation (41) [13]:

$$I_{s1qref} = \frac{\frac{3}{2} u_{m1q} i_{s1d} - Q_{m1ref}}{\frac{3}{2} u_{m1d}} \tag{41}$$

The outer control loop is depicted in Figure 3. The gains of the PI_2 controller are also determined by the optimal approach, which guarantees a slower dynamic of the outer loop in the desired settling time. The outer loop controls the reactive power and the DC voltage.

Simulation

To verify the validity of the proposed control strategies and to survey the problems with the weak networks rather than typical strong systems, simulation studies of the VSC-HVDC system were undertaken via MATLAB/Simulink in the operating conditions.

System Parameters

The parameters of the VSC-HVDC transmission system and the optimal gains of PI controllers in strong and weak networks, through the LQR method, are given in Tables 1-3, respectively.

Table 1. Parameters of the Simulation System

Frequency of AC network (Hz)	50
AC line resister R1 (Ω)	0.01
AC line reactor L1 (mH)	40
Shunt capacitors C1 (μF)	20
Load resistance R (Ω)	450
Load inductance L (mH)	11.5
Input voltage ug1d (kV)	250
Input voltage ug1q (V)	0
Rated DC Voltage us1 (kV)	300

Table 2. Gain of Optimal PI Controller in a Strong System

k_{pi}	Values	k_{ii}	Values
k_{p1}	-31.6128	k_{i1}	-2.4495×10^{-4}
k_{p2}	7.2548×10^{-4}	k_{i2}	7.2548×10^{-12}

Table 3. Gain of Optimal PI Controller in a Weak Network

k_{pi}	Values	k_{ii}	Values
k_{p1}	-31.5928	k_{i1}	-2.4479×10^{-4}
k_{p2}	7.2548×10^{-4}	k_{i2}	7.2548×10^{-12}

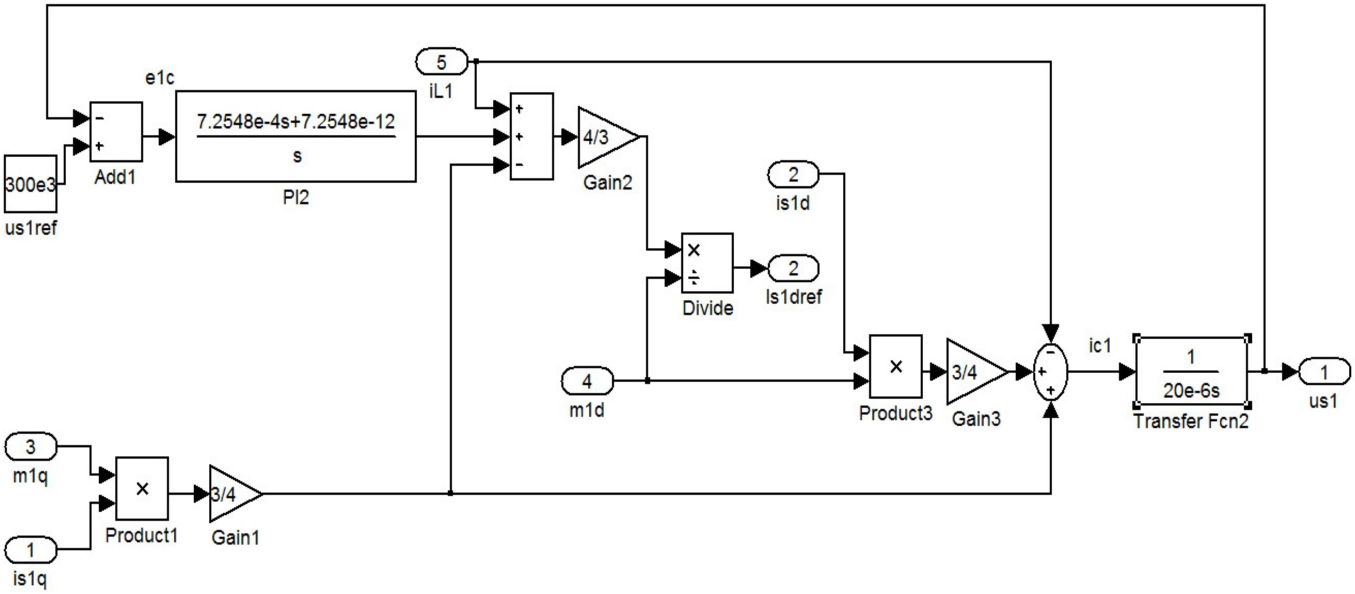

Figure 3. Outer Control Loop for DC Voltage, u_{s1}

Simulation Results

The behavior of the system outputs, while a change occurs in the load current, i_{l1}, due to switching in the weak and strong power systems, were studied. Using these optimal gains, DC voltage U_{s1} and Q_1 were controlled in order to track their reference values, 300 KV and 0, respectively. The behavior of current i_{s1d} in strong and weak networks during two switching conditions is shown in Figures 4 and 5; the behavior of DC voltage U_{s1} in the two different conditions is shown in Figures 6 and 7. As can be seen, in both conditions, the optimal PI controllers behave efficiently to decrease the fluctuations of DC voltage and AC current and improve the stability of the VSC-HVDC system. The time responses of the DC voltage and AC current reached a new stable steady-state value in response to load changes. However, in weak networks in which the short-circuit level is rather low, any kind of fault such as switching caused more changes in the DC voltage and AC current. I_{s1q} had a similar behavior in both conditions and was near zero, as was expected.

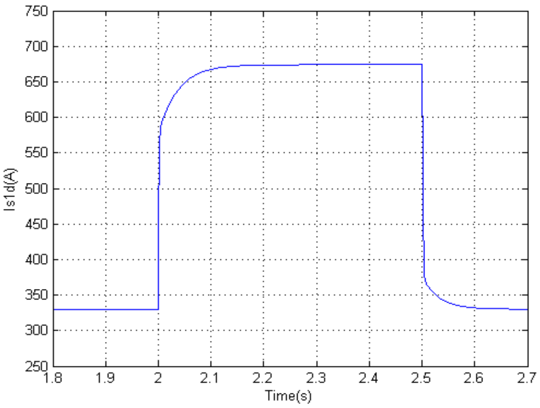

Figure 4. Current i_{s1d} Behavior in a Strong Power System

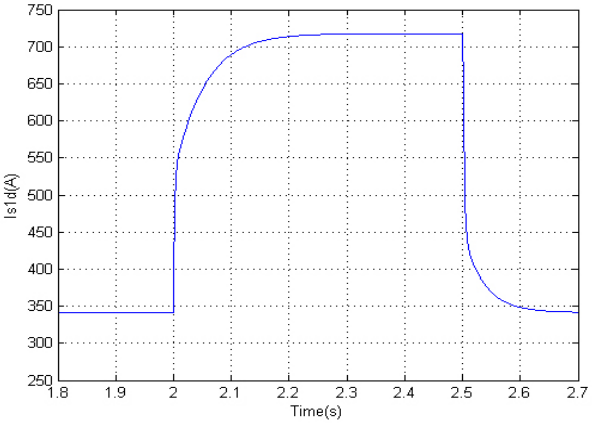

Figure 5. Current i_{s1d} Behavior in a Weak Power System

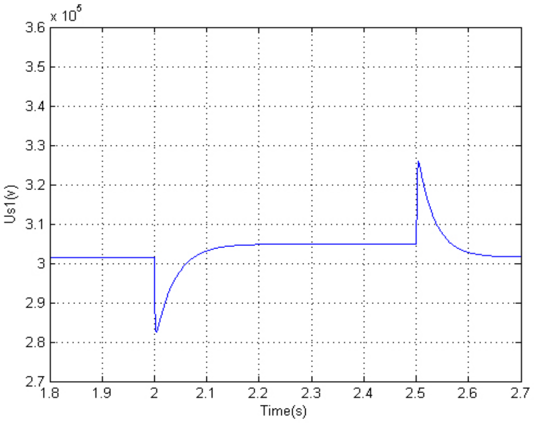

Figure 6. Voltage u_{s1} Behavior in a Strong Power System

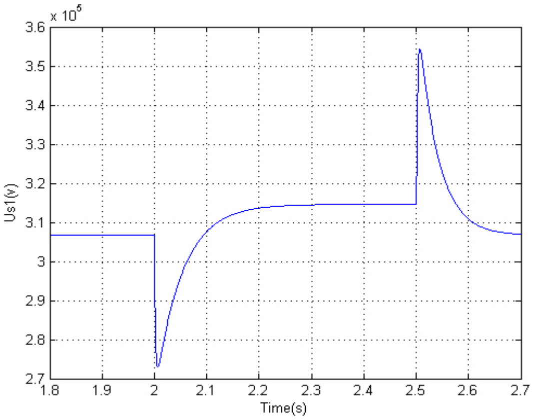

Figure 7. Voltage u_{s1} Behaviors in a Weak Network

Conclusion

It was necessary to design efficient control strategies to satisfy stability of VSC-HVDC transmission systems under external changes and different situations. After developing the mathematical model of the system, an optimal control method was designed and formulated to govern the DC link voltage and to control the reactive power on the AC side of the VSC-HVDC system. The PI controllers, which work through two faster inner loops to control the AC current and a slower outer loop to maintain the DC voltage and the reactive power, were designed to improve system performance. The gains of PI controllers were calculated using the optimal LQR method. To prove the efficiency of the proposed control strategy, with the goal of studying its performance in weak networks, the system was simulated via MATLAB/Simulink under operating conditions. It was determined from the results that faults in weak networks cause more changes and take more time to improve, as compared to the strong systems.

References

[1] Barberis Negra, N., Todorovic, J., & Ackermann, T. (2006). Loss Evaluation of HVAC and HVDC Transmission Solutions for Large Offshore Wind Farms. *Electric Power Systems Research, 76*(11), 916-927.

[2] de Algería, I. M., Martín, J. L., Kortabarria, I., Andreu, J., & Ereño, P. I. (2009). Transmission Alternatives for Offshore Electrical Power. *Renewable and Sustainable Energy Reviews, 13*(5), 1027-1038.

[3] Ramadan, H. S., Siguerdidjane, H., Petit, M., & Kaczmarek, R. (2012). Performance Enhancement and Robustness Assessment of VSC-HVDC Transmission Systems Controllers under Uncertainties. *International Journal of Electrical Power & Energy System, 35*(1), 34-46.

[4] Sharma, R., Rasmussen, T. W., Jensen, K. H., & Akamatov, V. (2010). Modular VSC Converter Based HVDC Power Transmission from Offshore Wind Power Plant: Compared to the Conventional HVAC System. *Electric Power and Energy Conference (EPEC),* (pp. 1-6). Halifax, NS.

[5] Eghlimi, M., & Shakouri, G. H. (2008). Economic Analysis of Iran-Turkey Power Network Interconnection: HVDC vs. HVAC. *IEEE 2nd International Power and Energy Conference*, (pp. 164-168). Johor Bahru.

[6] Beccuti, G., Papafotiou, G., & Harnefors, L. (2014). Multivariable Optimal Control of HVDC Transmission Links with Network Parameter Estimation for Weak Grids. *IEEE Transactions on Control Systems Technology, 22*(2), 676 - 689.

[7] O'Reilly, J., Wood, A. R., & Osauskas, C. M. (2003). Frequency Domain Based Control Design for an HVDC Converter Connected to a Weak AC Network. *IEEE Transactions on Power Delivery*, *18*(3), 1028-1033.

[8] Ruan, S.-Y., Li, G.-J., Peng, L., Sun, Y.-Z., & Lie, T. T. (2007). A Nonlinear Control for Enhancing HVDC Light Transmission System Stability. *International Journal of Electrical Power & Energy Systems*, *29*(7), 565-570.

[9] Yin, M., Li, G., Zhou, M., & Zhao, C. (2008). Simplified Input-Output Linearization Control for Wind Farm Interconnection Based on Multi-Terminal VSC -HVDC. *16th PSCC*, (pp. 1-7). Glasgow, Scotland.

[10] Blasko, V., & Kaura, V. (1997). A New Mathematical Model and Control of a Three-phase AC-DC Voltage Source Converter. *IEEE Transactions on Power Electronics*, *12*(1), 116-123.

[11] Bajracharya, C., Molinas, M., Suul, J. A., & Undeland, T. M. (2008). Understanding of Tuning Techniques of Converter Controllers for VSC-HVDC. *Nordic Workshop on Power and Industrial Electronics*, (pp. 1-8).

[12] Ruan, S.-Y., Li, G.-J., Jiao, X.-H., Sun, Y.-Z., & Lie, T. T. (2007). Adaptive Control Design for VSC-HVDC Systems Based on Backstepping Method. *Electric Power Systems Research, 77*(5-6), 559-565.

[13] Ayari, M., Moez Belhaouane, M., Braiek, N. B., & Guillaud, X. (2013). Optimal Control Design for VSC-HVDC Systems. *IEEE International Conference on Electrical Engineering and Software Applications (ICEESA),* (pp. 1-6). Hammamet.

Biographies

F. SAFDARIAN is currently a Master of Science graduate student and member of the Energy Systems Laboratory in the Power and Energy Management Division of the Department of Electrical Engineering at Amirkabir University of Technology (Tehran Polytechnic), Iran. Her research interests include power management, Smart Grid, HVDC systems, FACTS devices, DGs, renewable energy, and power electronics. Ms. Safdarian may reached at farnaz.safdarian@aut.ac.ir

M.M. ARDEHALI is an Associate Professor and the director of the Energy Systems Laboratory in the Department of Electrical Engineering at Amirkabir University of Technology (Tehran Polytechnic). He received his Ph.D. in energy conversion from the University of Iowa in 1995 and completed postdoctoral studies at Iowa State University in 1997. With numerous publications and patents, Dr. Ardehali is a registered professional engineer in several states in the U.S. and specializes in control and applications of artificial intelligence for energy systems including power generation facilities.

G. B. GHAREHPETIAN was an Assistant Professor at Amirkabir University of Technology (AUT), Tehran, Iran, from 1997 to 2003; an Associate Professor from 2004 to 2007; and is currently a full Professor. He was selected by the ministry of higher education as a distinguished professor of Iran; by IAEEE as a distinguished researcher of Iran; and, was awarded the National Prize in 2008 and 2010. He is the author of more than 700 journal and conference papers. His teaching and research interests include Smart Grid, DGs, monitoring of power transformers, FACTS devices, HVDC systems, and power system transients. Dr. Gharehpetian may be reached at grptian@aut.ac.ir

INSTRUCTIONS FOR AUTHORS: MANUSCRIPT REQUIREMENTS

The INTERNATIONAL JOURNAL OF MODERN ENGINEERING is an online/print publication, designed for Engineering, Engineering Technology, and Industrial Technology professionals. All submissions to this journal, submission of manuscripts, peer-reviews of submitted documents, requested editing changes, notification of acceptance or rejection, and final publication of accepted manuscripts will be handled electronically. The only exception is the submission of separate high-quality image files that are too large to send electronically.

All manuscript submissions must be prepared in Microsoft Word (.doc or .docx) and contain all figures, images and/or pictures embedded where you want them and appropriately captioned. Also, for all accepted manuscripts, each figure, image or picture that was imported into your Word document must be saved individually as a **300dpi or higher JPEG (.jpg)** file and submitted separately; your manuscript and figure numbers must be used in the title of the file (e.g., **M12-S-18 Figure 4**); that means one additional file for each image imported into your manuscript. These 300dpi images do NOT need to be embedded in your manuscript. For tables or graphs created directly in Word, you do not need to submit them as separate files.

Included below is a summary of the formatting instructions. You should, however, review the sample Word document of our website for details on how to correctly format your manuscript. The editorial staff reserves the right to edit and reformat any submitted document in order to meet publication standards of the journal.

The references included in the References section of your manuscript must follow APA-formatting guidelines. In order to help you, the sample Word document also includes numerous examples of how to format a variety of scenarios. Keep in mind that an incorrectly formatted manuscript will be returned to you, a delay that may cause it (if accepted) to be moved to a subsequent issue of the journal.

1. **Word Document Page Setup**: Two columns with ¼" spacing between columns; Top of page = ¾"; Bottom of page = 1" (from the top of the footer to bottom of page); Left margin = ¾"; Right margin = ¾".

2. **Paper Title**: Centered at the top of the first page with a 22-point Times New Roman (Bold), Small-Caps font.

3. **Page Breaks**: Do not use page breaks.

4. **Body Fonts**: Use 10-point Times New Roman (TNR) for body text throughout (1/8" paragraph indention); 9-point TNR for author names/affiliations under the paper title; 16-point TNR for major section titles; 14-point TNR for minor section titles; 9-point TNR BOLD for caption titles for tables and figures; other font sizes as noted in the sample document.

5. **In-text Referencing**: List and number each reference when referring to them in the body of your document (e.g., [1]). The first entry must be [1] followed by [2], [3], etc., continuing in numerical order to the final entry in your References section. Again, see the sample Word document for specifics. Do not use the End-Page Reference utility in Microsoft Word. You must manually place references in the body of the text.

6. **Tables and Figures**: Center all tables and figures. Captions for tables must be above the table, while captions for figures are below; all captions are left-justified.

7. **Page Limit**: Manuscripts should not be more than 15 pages (single-spaced, 2-column format).

8. **Page Numbering**: Do not use page numbers.

9. **Publication Charges:** Manuscripts accepted for publication are subject to mandatory publication charges.

10. **Copyright Agreement:** Review the **copyright transfer agreement**.

11. **Submissions:** All manuscripts and associated files must be submitted electronically; the only exception would be if you wish to submit a CD with the individual files for your high-quality images, as noted above.

MANUSCRIPTS should be submitted to Dr. Philip D. Weinsier, manuscript editor, at philipw@bgsu.edu along with a copy to editor@ijme.us.

FILES containing your high-quality images should ONLY be submitted to philipw@bgsu.edu.

CUTTING EDGE JOURNAL OF RESEARCH AND INNOVATION IN ENGINEERING

www.ijeri.org

Print ISSN: 2152-4157
Online ISSN: 2152-4165

www.iajc.org

INTERNATIONAL JOURNAL OF
ENGINEERING RESEARCH AND INNOVATION

ABOUT IJERI:

- IJERI is the second official journal of the International Association of Journals and Conferences (IAJC).
- IJERI is a high-quality, independent journal steered by a distinguished board of directors and supported by an international review board representing many well-known universities, colleges, and corporations in the U.S. and abroad.
- IJERI has an impact factor of **1.58**, placing it among an elite group of most-cited engineering journals worldwide.

OTHER IAJC JOURNALS:

- The International Journal of Modern Engineering (IJME)
  For more information visit www.ijme.us
- The Technology Interface International Journal (TIIJ)
  For more information visit www.tiij.org

IJERI SUBMISSIONS:

- Manuscripts should be sent electronically to the manuscript editor, Dr. Philip Weinsier, at philipw@bgsu.edu.

  For submission guidelines visit www.ijeri.org/submissions

TO JOIN THE REVIEW BOARD:

- Contact the chair of the International Review Board, Dr. Philip Weinsier, at philipw@bgsu.edu.

  For more information visit www.ijeri.org/editorial

INDEXING ORGANIZATIONS:

- IJERI is currently indexed by 16 agencies. For a complete listing, please visit us at www.ijeri.org.

Contact us:

Mark Rajai, Ph.D.

Editor-in-Chief
California State University-Northridge
College of Engineering and Computer Science
Room: JD 4510
Northridge, CA 91330
Office: (818) 677-5003
Email: mrajai@csun.edu

www.tiij.org

www.ijme.us

THE LEADING JOURNAL OF ENGINEERING, APPLIED SCIENCE AND TECHNOLOGY

The latest impact factor (IF) calculation (Google Scholar method) for IJME of 3.0 moves it even higher in its march towards the top 10 engineering journals.

IJME IS THE OFFICAL AND FLAGSHIP JOURNAL OF THE
INTERNATIONAL ASSOCATION OF JOURNALS AND CONFERENCE (IAJC)
www.iajc.org

The International Journal of Modern Engineering (IJME) is a highly-selective, peer-reviewed journal covering topics that appeal to a broad readership of various branches of engineering and related technologies. IJME is steered by the IAJC distinguished board of directors and is supported by an international review board consisting of prominent individuals representing many well-known universities, colleges, and corporations in the United States and abroad.

IJME Contact Information

General questions or inquiries about sponsorship of the journal should be directed to:

Mark Rajai, Ph.D.
Editor-in-Chief
Office: (818) 677-5003
Email: editor@ijme.us
Department of Manufacturing Systems Engineering & Management
California State University-Northridge
18111 Nordhoff St.
Northridge, CA 91330